Universidade do Minho
Escola de Engenharia

Bruno Manuel Oliveira Ramoa

Characterisation and Prediction of Mechanical Properties of Injection Moulded Polypropylene

Dissertação de Mestrado

Mestrado em Engenharia de Polímeros

Trabalho efetuado sob a orientação de:

Professor Doutor: Júlio César Machado Viana

Professor Doutor: Ricardo João Ferreira Simões

Outubro de 2015

ACKNOWLEDGMENTS

The conclusion of this thesis would not be possible without the precious help and support of several individuals. To:

Prof. Júlio Viana and Prof. Ricardo Simões, my scientific supervisors, for their support, availability and scientific guidance, a much felt thank you.

Carlos Barbosa, for all his advises and expertise help.

My family and friends, a special word of gratitude for their patience and encouragement during the realization of this thesis.

ABSTRACT

The characterisation of an automotive grade polypropylene, using a Taguchi L8 orthogonal array, was carried out in order to evaluate and quantify the differences in morphological features such as: skin ratio (Sa), bulk and skin crystallinity ($\chi_{bulk}$and χ_{skin}), molecular orientation (Ωs) and β-phase content (k-value), and tensile properties: yield stress (σ_y), elastic modulus (E) and strain at break (ε_b) induced by different processing conditions. The morphological features were assessed by polarised light microscopy, differential scanning calorimetry and wide angle x-ray diffraction, respectively. The mechanical properties by quasi-static (20 mm/min) and high speed tensile (1 and 3 m/s) tests. Afterwards, Autodesk Moldflow Insight 2012 was used to calculate thermomechanical variables using a dual domain mesh model to later apply the thermomechanical indices methodology. It was used to describe the variation of both morphological and mechanical properties and to subsequently establish mathematical equations to describe straightforward relationships between the TMI and these properties. Such regression equations allow the prediction of mechanical properties as a function of the injection moulding conditions. Finally, an industrial-like case-study was carried out (using samples supplied by an industrial company) in order to identify the processing conditions that display the highest values of peak force and puncture energy measured in a falling weight impact test and subsequently establish the TMI methodology to predict the impact responses of the used material.

Analysis of Variance was used to quantify the effect of the processing conditions on all morphological and tensile properties. Globally it was found a strong influence of the injection velocity (v_i) and injection temperature (T_i) on the morphological parameters. A decrease of T_i seems to increase the majority of the morphological features, whereas a contrary effect was observed for v_i. Sa increased for low values of v_i and all other morphological properties increased with the increase of the injection velocity. Regarding the mechanical properties, the mould temperature (T_w) and holding pressure (P_h) were the most significant processing conditions. A low value of T_w resulted in the increase of the majority of tensile properties. On the other hand, an opposing effect was observed for the holding pressure. σ_y and E presented a low variation within each microstructure which can be due to the coupled effect of opposing effects on these properties (Ωs and k- value) promoted by the same processing variables and the fact that the bulk crystallinity showed virtually no variation.

In the case-study, a lack of variation on the impact properties was also observed which in due turn compromised the use of the full extent of the TMI. This methodology is still under development but shows

a great potential to predict both morphological and mechanical responses as a function of the existent thermomechanical environment.

RESUMO

A caracterização de um polipropileno de grau automóvel, utilizando uma matriz ortogonal Taguchi L8, foi realizada a fim de avaliar e quantificar diferenças produzidas por diferentes condições de processamento em propriedades morfológicas, tais como: rácio casca- núcleo (Sa), cristalinidade média (χ_{bulk}) e da casca (χ_{skin}), orientação molecular (Ωs) e população de esferulites na fase β (k- value), e em propriedades mecânicas medidas à tração: tensão de cedência (σ_y), módulo de elasticidade (E) e deformação à rutura (ε_b).

As características morfológicas foram avaliadas, respetivamente, através de microscopia de luz polarizada, calorimetria diferencial de varrimento e difração de raio-X. As propriedades mecânicas por ensaios de tração realizados a velocidades quase-estáticas (20 mm/min) e a alta velocidade (1 e 3 m/s). Posteriormente, o *software* Autodesk Moldflow Insight 2012 foi utilizado para calcular variáveis termomecânicas utilizando um modelo com malha *dual domain* de forma a aplicar a metodologia dos índices termomecânicos (TMI). Esta foi utilizada para descrever a variação nos parâmetros morfológicos e mecânicos e subsequentemente estabelecer relações matemáticas diretas entre os TMI e as propriedades avaliadas. Por fim, um caso de estudo foi realizado (utilizando amostras fornecidas por uma empresa) de forma a identificar as condições de processamento que apresentam maiores valores de força de pico e energia à rutura medidas num ensaio de queda de dardo e, posteriormente, aplicar a metodologia dos TMI para prever as respostas de impacto deste material.

Análise de variância foi utilizada para quantificar a influência das condições de processamento nas propriedades morfológicas e mecânicas medidas à tração. Verificou-se que a temperatura (T_i) e velocidade de injeção (v_i) são as variáveis operatórias que mais influenciam as propriedades morfológicas. Uma diminuição de T_i levou ao aumento da generalidade dos parâmetros avaliados ao passo que v_i apresentou um efeito contraditório. Sa aumentou para baixos valores de v_i e os restantes parâmetros morfológicos para um aumento da velocidade de injeção. Em relação às propriedades mecânicas, a temperatura do molde (T_w) e a pressão de manutenção (P_h) foram as variáveis mais importantes. Uma redução de T_w conduziu a um aumento da generalidade das propriedades à tração, por outro lado um efeito contraditório foi observado por parte de P_h.

A tensão de cedência e módulo de elasticidade dentro das diferentes microestruturas apresentaram uma baixa variação. Tal pode ser devido a um efeito sinergético provocado por efeitos antagónicos (Ωs

e k-value) que são promovidos pelas mesmas variáveis operatórias e ao facto de a cristalinidade média se apresentar praticamente constante nas diferentes microestruturas.

No caso de estudo, uma falta de variação nas propriedades ao impacto também foi observado comprometendo a utilização dos TMI. Esta metodologia ainda se encontra em desenvolvimento mas mostra grande potencial para prever propriedades mecânicas e morfológicas em função do ambiente termomecânico existente no processo de injeção.

INDEX

INDEX OF FIGURES

INDEX OF TABLES

ABBREVIATIONS

IM	Injection moulding
CAE	Computer aided engineering
CAD	Computed aided design
DOE	Design of Experiments
AMI	Autodesk Moldflow Insight
PP	Polypropylene
hPP	Polypropylene homopolymer
cPP	Polypropylene copolymer
iPP	Isotactic polypropylene
PLM	Polarised light microscopy
SAXS	Small angle X-ray scattering
WAXS	Wide angle X-ray scattering
NA	Nucleating agent
CI	Cooling index
TSI	Thermo-stress index
TMI	Thermomechanical index
TMV	Thermomechanical variables
FLF	Frozen layer fraction
MWA	Moulding window analysis
SCORIM	Shear Controlled Orientation Injection Moulding

NOMENCLATURE

$\dot{\varepsilon}$	Strain-rate
τ_w	Shear stress at wall
T_b	Bulk temperature
T_C	Crystallization temperature
T_w	Mould temperature
T_i	Injection temperature
T_{int}	Temperature at the mould-polymer interface
v_i	Injection velocity
H	Thickness of the part
γ	Bulk shear-rate
R	Sample-to-detector distance
T_g	Glass transition temperature
T_m	Melt temperature
Sa	Skin Ratio
Ωs	Skin Orientation
k- value	β- phase content
χ_{bulk}	Bulk degree of crystallinity
χ_{skin}	Skin crystallinity index
t_i	Injection time
P_h	Holding Pressure
t_{Ph}	Holding time
R^2	Regression coefficient
σ_y	Yield Stress
ε_b	Strain at Break
Y_C	Cooling index at the end of the filling stage
τ_Y	Thermo-stress index at the end of the filling stage

1. INTRODUCTION

Plastic materials have a wide range of properties and their application has been introduced in several sectors from packing to aerospace, substituting in some cases, ceramics and metals. The worldwide production of these materials has been raising throughout the last decades. In 2013, Europe consumed approximately 46.3 Million tons of these materials and the automotive industry 8.5%, from which polypropylene (PP) was the most consumed polymer [1]. Polypropylene is a widely used semi-crystalline polymer that has been extensively investigated for academic and industrial purposes. This polyolefin presents a wide range of mechanical properties which are dependent, among other aspects, upon the processing technique.

Injection moulding (IM) is one, is not the most, used processing technique in the automotive industry. It offers a great flexibility in the design of parts, high production rates and high dimensional accuracy.

It is known that a layered up structure, composed of a skin and a core region, is developed when injection moulding semi-crystalline polymers. Fujiyama [2] demonstrated that the properties of the skin layer in an injection moulded PP had quite a distinct behaviour from the core layer. Nowadays, the engineering procedure to study the mechanical behaviour of injection moulded semi-crystalline polymers has been based on the scale features of this skin-core laminate arrangement. Also, because of the strong stress and temperature gradients existent in the IM process several types of hierarchical superstructures, such as the skin ratio [3]–[6], molecular orientation [7]–[10], and polymorphic crystalline structures [5], [10]–[14] are developed when processing polypropylene. Furthermore, the relationship between operating variables vs microstructural development, operating variables vs mechanical responses and morphology vs mechanical properties is not strictly straightforward [2], [15]–[22].

In an industrial context, more specifically in the automotive industry, cars are designed to be crashworthy so their components have to subjected to mechanical tests to ensure the safety of passengers and to more accurately design parts in order to save raw-material and the overall cost. One of the most extensively used mechanical tests used to obtain basic mechanical properties (e.g., elastic modulus, yield stress and strain at break) is the tensile test. Extensive knowledge is available about the mechanical behaviour of PP at quasi-static conditions (strain-rate $<10^{-2}$ s^{-1}) whilst due to the complicated experimental procedure and data interpretation not enough reliable material data has so far been determined at high strain-rates [23]–[28].

Despite all the anisotropic behaviour displayed by semi-crystalline polymers some models exist to predict the mechanical behaviour or a certain response of these materials [10], [24], [26], [29]–[31]. However, the majority of the models require the use of extensive microstructural analysis techniques which is not a cost-effective approach and therefore not applicable within the automotive industry. Thus, establishing straightforward relationships between processing conditions and the mechanical behaviour at the product development stage, enabling the prediction of properties, seems to be a valuable tool [32].

This work is divided into four sections. Firstly, identifying the most important processing variables and assess their influence on the morphological development in a lateral gated disc geometry. Secondly, study the effect of these variables on the tensile properties measured at both quasi-static and high speed conditions. Thirdly, use the thermomechanical indices (TMI) methodology , previously proposed [10], [28], [31]–[35], to correlate the morphological and mechanical responses of an automotive grade polypropylene with the thermomechanical environment developed during the injection moulding process. Lastly, an industrial-like case study will be carried out in some supplied samples to evaluate the experiments that present the highest values of peak force and puncture energy obtained through a falling weight impact test and subsequently use TMI methodology to define predictive models for these parameters.

The document is organised as follows: The chapter bellow (1.1) describes the state of the art with a specific focus on the goals of this project. The ones up to chapter 7 theoretical concepts of the experimental techniques used in accordance to what was found in literature are addressed. Chapter 7 and 8 describe the experimental procedure and the discussion of the obtained results. Chapter 9 covers the case study and finally, chapter 10 the conclusions of this work.

1.1 State of the Art

1.1.1 Structure development during the Injection Moulding (IM) process

Regarding the skin ratio, authors such as Fujiyama and Azuma [3] studied the effect of the melt temperature on the skin layer of several isotactic polypropylenes, both copolymer (cPP) and homopolymer (hPP). As a conclusion of their work they observed through polarised light microscopy (PLM) that with the decrease of this operative variable the skin layer increased. Housmans et al. [4] used capillary rheometer to drive several melted isotactic polypropylenes into a simple rectangular mould using different piston velocities. Though PLM they were able to identify 4 different layers from the edge to the core of the

sample, a skin layer, a transitional layer, a shear layer and an isotropic core. The authors noticed that when lowering the injection velocity both the transition layer and shear layer increased. Shen et al .[5] evaluated the skin thickness developed in and injection moulded iPP rectangle along the flow direction. The results showed that the skin layer diminishes along the flow path and that with different moulding temperatures, at the same distance from the gate, the lower the melt temperature the thicker the layer. Viana [6] injection moulded cPP parts with different geometries and explored the processing conditions affecting the development of the skin layer in the IM process. He noticed that three processing variables had influence on this parameter. The melt temperature, mould temperature and the injection velocity (flow rate). The first had a strong effect on skin layer and the author justified this by indicating that the raising in the melt temperature resulted in a larger time to reach the crystallization temperature and relaxation time, both effects contributing for the skin thinning mechanisms. The mould temperature had a low contribution for the development of this parameter and showed an opposing effect. A decrease of this operative variable raised the cooling rate, which reduced the time to reach to the crystallization temperature resulting in a thicker skin. However it also decreased the crystallization temperature by increasing the time to reach this thermal transition, thus leading to thinner skin. Lastly, the injection flow rate. The author stated that an increase of this parameter raised the temperature and shearing level of the melt. The latter phenomena has two different effects: it increases the crystallization temperature therefore reducing the time to reach the crystallization temperature (thinner skin); and it decreases the material relaxation time (thinner skins).

As for the molecular orientation and crystallinity developed when processing PP, due to the complex combination of the imposed stress field and cooling rate which strongly affects the crystallization kinetics, the macromolecular chains in the melt are highly extended forming supermolecular structures with central bundles (shishes) in which radial lamellae grow epitaxially (kebabs) [36]. Varga and Karger [11] studied the shear-induced crystallization of isotactic polypropylene (iPP) homo-, block, and random copolymers. In their study, it was evidenced that melt-shearing caused by fibber pulling was associated with the development of α-row-nuclei which served as self-nuclei of the bulk crystallization process and could induce the growth of the β-modification resulting in a polymorphous composition. Tribout et al. [12] observed the effect of shear in the crystallization kinetics of an Impact polypropylene copolymer and concluded that the nucleation density was strongly enhanced by this parameter. Faravo et al.[7] evaluated the molecular orientation by WAXS in the skin layer of an injection moulded iPP, both nucleated and non-nucleated. As a conclusion of their work, they showed that the most influential processing parameters were the mould temperature and flow rate. They observed that as the mould temperature increased the

characteristic molecular orientation of PP decreased due to the decrease of the cooling rate and the increase of the relaxation time, and, as the injection flow rate increased, an increase of the distinctive molecular orientation of PP was observed due to the increase of the flow velocity. Mendonza et al. [8] studied the molecular orientation in injection moulded plates with 1 and 3 mm of thickness using a commercial PP homopolymer (hPP) and resorting to infrared dichroism and WAXS. The authors varied the mould temperature (from 20 to 40 °C) and injection time (1.6 to 0.7s). They noticed that, paradoxically, the increment in injection velocity had no large influence when tripling the thickness of the moulding. They concluded that the thickness of the part is the factor which governed the global level of crystalline orientation. Van Erp et al., [9] studied the effect of the injection velocity in thin walled rectangular plates. They concluded that a lower injection velocity resulted in a higher degree of orientation in the flow direction. Cermak et al. [13] evaluated the effect of the mould temperature and hold pressure in the variation of crystallinity in the skin layer by WAXS for both α and β iPP. They noticed an increase of χ_{skin} for a raise in the mould temperature and a decrease in hold pressure. Demiray et al. [37] obtained a rather uniform crystallinity profile through the sample thickness of iPP mouldings. They justified this by reporting limitations on the experimental procedure and by stating that secondary crystallization occurred during the sample storage. Also, the crystallinity profile was not affected by the injection velocity, mould temperature and hold pressure, possibly due to the high crystallization rates of the used PP. Viana et al. [10] studied the effect of processing conditions (v_i, T_i and T_w) on some morphological parameters, through the use of thermomechanical indices, namely the skin orientation and crystallinity index measured by WAXS. The authors noticed that the shear stress played an important role in Ωs. An increase in this parameter led to a higher value of orientation. Regarding χ_{skin}, they noticed that a higher shear and thermal level led to an increase of the degree of crystallinity in the skin layer.

Concerning the β-phase content, Shen et al.[5] studied the development of β-crystals along the flow direction of an injection moulded rectangular part as a function of the melt temperature. They observed that this parameter diminished with the distance from the gate. Cermák et al. [13] evaluated the effect of the mould temperature and hold pressure on the structure of isotactic polypropylene (iPP), both α-iPP and β-nucleated (β-iPP), namely the skin layer thickness, crystallinity and β-phase content. To assess the crystallinity and β-phase content they used WAXS and concluded that a raise in the mould temperature led a positive effect on the crystallinity and β-phase content in the specimens, particularly in the skin region. On the other hand, when rising the hold pressure a negative influence on the crystallinity and β-form content was manifested throughout the bulk of both α and β- iPP specimens. He also stated that the impact strength of β-iPP exceeds that of α-iPP and justified this by saying that the superior toughness

of β-iPP over α-iPP can be attributed to a combined effect of the following factors (sectors): the α to β phase transformation induced by mechanical load, the enhanced mechanical damping of β-iPP or the peculiar lamellar morphology of β-iPP. Zhang et al. [14] studied the structural evolution of a β-nucleated iPP in a tensile test by in-situ WAXS. They compression moulded plates and took tensile specimens to perform tests at various temperatures (30, 60, 90 and 120°C). They observed that a β-mesophase transition occurred for the lowest test temperature while for the remaining test temperatures a β-α transition took place.

1.1.2 Mechanical properties of IM parts

Fujiyama [2], demonstrated that the mechanical properties of the skin layer in an injection moulded PP have a quite distinct behaviour from the core layer. The first presented a more brittle behaviour and a latter a more ductile one.

Roman et al.[15] studied the effect of the mould temperature and hold pressure on the tensile properties of α and β-nucleated polypropylene. They observed a positive effect of higher values of mould temperatures on the elastic modulus and a negligible effect of the holding pressure. Also, none of the previous processing variables showed any significant effect on the yield stress. Regarding the strain at break, since β- spherulites have a more ductile behaviour, the nucleated conditions displayed a higher deformation value. Zhou and Mallick [38] assessed the effect of the melt temperature and hold pressure on the tensile properties of a talc filled polypropylene. They noticed that in the flow direction the yield stress increase with increasing hold pressure but were relatively insensitive to the melt temperature.

Barbosa et al. [32] evaluated the effect of the processing conditions on a talc filled PP in a falling weight impact test. They concluded that the most significant processing variables were the injection and mould temperature. A decrease of these variables led to an increase of the peak force, peak energy and puncture energy.

Kalay and Bevis [16] reported that in conventional injection moulding, a very high injection speed can result in the decrease of the modulus due to shear heating. However, for low values of this operating variable a decrease in the modulus can also be obtained due to low molecular orientation. As for the injected temperature, they referred that a low value of this variable could lead to a decrease in the modulus due to the occurrence of the β-phase. Regarding the holding pressure, they referred that higher stiffness values could be obtained due to the promotion of molecular orientation.

Viana et al.[17] studied the effect of the skin thickness on the tensile properties of a PP copolymer. They observed that yield stress and modulus increased with the increase of the skin layer while the strain at break decrease with this parameter.

Van der Wal et al. [18] studied the effect of crystallinity on the fracture of polypropylene. They reported that modulus and yield stress increased almost linearly with increasing crystallinity. Parenteau et al. [19] studied the effect of crystallinity on the elastic properties in injection moulded polypropylene. They reported that an increase in crystallinity and in the mean thickness of the crystalline lamellae resulted in a higher elastic modulus. Tordjeman et al. [20] assessed the effect of different crystalline structures (α and β) on the mechanical properties of PP. They added different amounts of β-nucleating agent to an iPP and then compression moulded plates in order to produce tensile specimens. They observed that the yield stress and modulus decreased with the increase of the β-phase content and that the strain at break increased with the β-content.

Viana [21] injection moulded cPP with different processing conditions and evaluated the yield stress at several test velocities (2, 10, 100, 500 mm/min and 3 m/s). He reported that the yield stress increases with the thickness and level of the crystalline phase orientation of the skin layer and the thickness of the core lamella. He also mentioned that, as the strain-rate increased the contribution of the morphological parameters such as the skin layer saturated and the effect of the core layer became more pronounced.

Way et al.[39] studied the effect the spherulite size (R_s) on the yield stress. They observed that as R_s increased, up to a spherulite radius of 100 μm, the yield stress also increased. R_s with higher values led to the decreased of this mechanical property.

Kalay and Bevis [22] evaluated the effect of molecular orientation on the mechanical properties of PP produced by conventional and shear-controlled orientation injection moulding. They remarked that the thickness of the moulding is critical in achieving high molecular orientation and that the pronounced orientation obtained from SCORIM increased the Young's modulus.

There are not many studies regarding high speed tensile tests of polymeric materials [24]–[28] mainly because no standard procedure exist. This makes the experimental procedure and data interpretation hard to evaluate. Only a recommendation procedure by the Society of Automotive Engineers (SAE) exists. Zrida et al [24] and Schoßig [26] studied the effect of the strain-rate in a tensile test on a polypropylene. They both found that the tensile strength increased with an increase of the strain-rate. Raisch and Moginger [25] used a new approach to calculate the elastic modulus and showed that the strain-rate dependency of the modulus could be used to get rid of the stress oscillations superimposed on the stress

signal. Xiao [27] evaluated the procedure proposed by the SAE guideline and concluded that the generated results could be ranked as good when using the criteria provided by the guideline.

1.1.3 Modelling the mechanical behaviour of IM parts

Up to this point it is obvious the final performance of a part is highly dependent upon the morphological development and strain-rate. To simulate the mechanical behaviour of polymer materials it is necessary to draw up a model which accounts for the response of the polymer to various mechanical loads, as well as their strain-rate dependency. Several models to predict mechanical properties in polymeric structures exist, and they can be classified into three categories: phenomenological [24], [26], [29], empirical [10] and micro-mechanical [30], [31]. In the case of the micro-mechanical, the crystalline structures are treated as reinforcements in the amorphous phase [30] or in the case of the laminate theory, the thickness of the sample is discretised into layers. Each layer assumed to be made of an homogeneous isotropic material having a constant level of crystallinity and spherulite size [31]. The phenomenological models like the Hyper-Visco-Hysteresis (HVH) model [24], [29] predicts the strain-rate behaviour based on a rheological model accounting the hyperelastic, viscous and hysteresis contributions of the material. The G'Sell-Jonas model [26] comprises the viscoelasticity, viscoplasticity, strain hardening and the influence of temperature. However, the majority of the above mentioned models does not correlate the processing conditions and subsequent morphological structure with the mechanical properties.

The thermomechanical indices (TMI) methodology was pioneered by J.Viana [33] and dates from the late 90's. It aims to correlate physical phenomena involved in the injection moulding process with the morphological and mechanical development in a part. The author derived two thermomechanical indices referent to the filling stage: the thermo-stress index (τ_Y) and the cooling index (Y_c). The first intends to indirectly quantify the orientation imposed during the mould filling, and the latter to indirectly quantify the crystallinity level in the core. In his doctoral thesis [33] he found that the same morphological parameter in different geometries, therefore leading to a different thermomechanical environment, had a different trend on the TMIs. To be more specific, he studied the effect of τ_Y and Y_c on the skin ratio for a dumbbell and disc specimen. In the dumbbell specimen the skin ratio increased with a raise in τ_Y whereas for the disc geometry the skin layer increase with the decrease of τ_Y. He further studied the relationship between the thermomechanical indices in dumbbell specimens with other morphological properties such as the skin orientation, β-phase content and skin and core crystallinity [10], [28], [31], [34], [35].

Cunha et al. [34] gave another contribution to this methodology by proposing a method to weight the TMIs with the skin ratio. They obtained a substantial improvement in the regression coefficients between the TMI and tensile properties (yield stress, elastic modulus and strain at break). Using this method Viana et al.[28] established relationships between the TMIs and tensile properties measured at low (2mm/min) and high speed (3m/s) tensile tests. For the quasi-static conditions they observed that all tensile properties increased with the increase of both weighted indices and that for the high speed tests the modulus and yield stress increased with the increment of both weighted indices and the strain at break decreased with the increment of the TMIs.

In more recent years, Barbosa et al. [32] tried to further develop this methodology in order to encompass the packing and cooling stages of the injection moulding cycle. They derived new indices and tried to predict the impact response, namely the peak force (F_P), peak energy (U_P) and energy at break (U_b), of an injection moulded talc-filled polypropylene through a falling weight impact test. They obtained good results, being the biggest deviations for predicted vs measured results of 7% for F_P and 23% for U_p and U_b. Despite the good results, and as final remark, they stated that the TMI methodology and the mechanical properties predictive tool was still under refinement.

1.2 Goals

The scope of this work is to characterise the morphological and mechanical properties evaluated through polarised light microscopy, differential scanning calorimetry, wide angle x-ray diffraction, quasi-static and high speed tensile tests of an automotive grade thermoplastic (Hostacom EP 3307) as a function of the processing conditions and to subsequently establish predictive models to correlate mechanical responses with the thermomechanical environment developed during the injection moulding process.

The specific goals are:

1. Identify and quantify the effect of processing conditions that mainly influence the skin ratio, molecular orientation, crystallinity, β-phase content and some mechanical properties (yield stress, modulus and strain at break) using a lateral gated disc geometry;
2. Characterise the thermomechanical environment of different processing conditions with an injection moulding simulation software, namely Autodesk Moldflow Insight 2012;
3. Correlate the obtained results from the morphological and mechanical characterisation with the thermomechanical indices methodology;

4. Evaluate the performance of some supplied lateral injected discs in a falling weight impact test and establish a model to predict the peak force and puncture energy (case study).

2. INJECTION MOULDING

2.1 Technology

There are several processes to mould plastic materials (e.g., extrusion, rotational moulding, thermoforming, blow moulding, calendaring), but only injection moulding allows for a great flexibility in the design of complex parts as well as great production rates and high dimensional accuracy.

The injection moulding process had a great technological expansion by the time of the Second World War, when the petrochemical industry enabled the sale of a set of thermoplastics at competitive prices. After the second half of the 1950's the process has been subjected to several technological improvements, becoming one of the most widely used technologies to this day [40], [41].

Injection moulding consists of a repetitive process in which melted (plasticized) plastic is forced (injected) into a mould where it is held under pressure until it is solidified and removed, replicating the geometry of the cavity. A feeding system conveys the melt from the machine cylinder to the mould cavity(ies). It may consist in a single or multiple cavities of similar or dissimilar shape. The process ends with the opening of the mould and subsequent extraction of the part(s).

A conventional injection moulding machine is typically composed of four units (Figure 1):

a) Power unit - responsible for providing energy to the various machine actuators;
b) Injection unit - promotes the transport, heating, plasticizing and homogenization of material from the bottom of the hopper to the injection nozzle. It also ensures injection and pressurization of the melt;
c) Clamp unit - allows the setting and movement of the mould. This is responsible for keeping the mould closed during the injection and pressurization phases. It also integrates the devices required for the extraction of parts;
d) Control unit - integrates the devices necessary to ensure the monitoring and control of various process variables. It is the operator interface and communication with peripherals or information management systems.

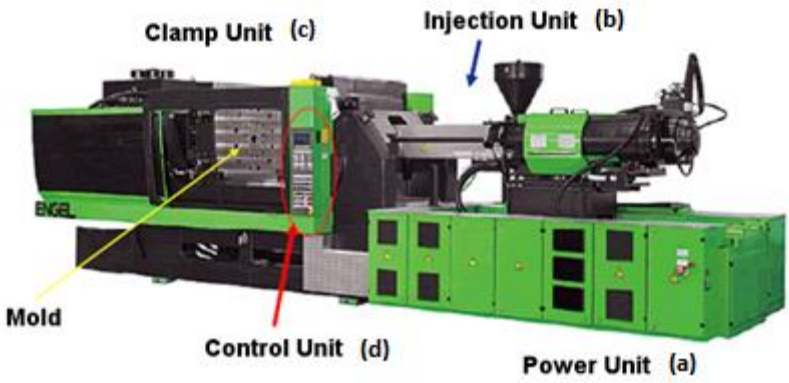

Figure 1: Conventional injection moulding machine

2.2 The Cycle

The injection cycle (Figure 2) can the defined as the set of operations that are carried out in the injection moulding machine during the production of consecutive parts. This process includes the following steps:

1. Mould closing – this is the operation that starts the cycle and should be as fast as possible, taking into account that the contact between the two parts of the mould should be smooth in order to prevent any damage to the surface;
2. Injection - at this stage, and after melting/softening, the polymeric material is forced to flow into the cavity;
3. Holding (Pressurization) - after the filling stage it is necessary to continue and pressurize the moulding in order to prevent reflux and contraction of the material;
4. Cooling - when the melt comes into contact with the mould, it loses heat in the form of conduction to the metal of the mould cavity. This phase is concluded when the temperature of the material decreases to the point of being able to remove the part from the cavity without distortion of the product.
5. Extraction of the part – The time needed to fulfil this operation is a function of the machine, namely the characteristics of the clamping unit and dislocation of the mould during the opening time;
6. Pause – The time between the extraction of the part and the beginning of a new cycle.

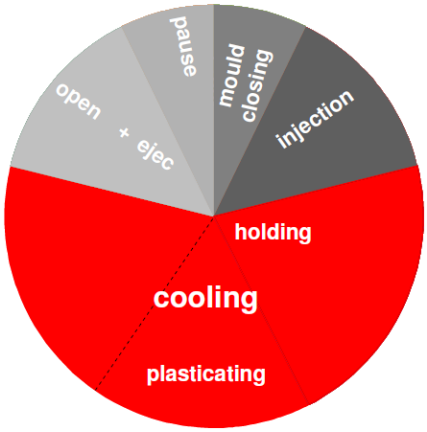

Figure 2: The injection moulding cycle [42]

The objective of the process, at an industrial level, is to minimize the time of each operation and ensure that the parts leave with the specified specifications. The optimization of this cycle basically ensures economic competition given that the initial investment for the acquisition and installation of the IM equipment, as well as the manufacturing of moulds, are quite high.

To reduce the time needed for the optimization of the IM process and to establish better processing conditions, computer aided engineering (CAE) and computer aided design (CAD) tools have been widely implemented. These techniques employ software to design and simulate the performance of a component in order to improve product designs or assist in the resolution of engineering problems. A software like Autodesk Moldflow Insight (AMI) is a good example of the CAE/CAD implementation. It has been used by several authors to improve the injection mould design and plastic part design, as well as the injection moulding process [43]–[46].

2.3 Thermomechanical Environment

In the injection moulding process, the thermal and mechanical phenomena are strongly coupled because of the dependence of the viscosity on the shear rate and temperature. The complex thermomechanical environment imposed to the melt results, mainly, from the combined effect of:

- the high shear rates associated to the flow rate;
- the moulding geometry;
- the material rheological properties;
- high cooling rates resulting from the relatively low temperatures of the mould walls;
- pressure level of the holding stage;
- the material physical properties (specific volume, thermal, etc.).

These thermomechanical conditions affect the morphological development of a polymeric part, thus determining its final mechanical properties (and others).

During the injection (filling) stage, the melt is driven through the feeding system into the mould cavity(ies). Due to the flow fountain effect and the high values of shearing, the macromolecules are stretched and frozen almost immediately forming a skin layer. The next portion of melted polymer flows rapidly in the central regions of the moulding, now thermally insulated by the previously formed solidified skin. The macromolecules relax over the available period of time or in the case of semi-crystalline polymers, until the crystallization temperature is reached. The relaxation phenomenon depends on the structure of the polymer, the cooling rate and pressure. During the next stage (holding), the melt velocity is drastically reduced, but a small amount is still introduced in the mould cavity to compensate for the volumetric shrinkage. This additional input of material will influence the shear stress distribution especially near the solid/melt interface due to the lower local temperatures and hence higher viscosity of the melt. Meanwhile, the core cools down under a relatively high pressure. The duration of this step is usually determined by the time need to reach the solidification of the gate. The solidified layers act as insulators during the cooling due to the low thermal diffusivity of the polymer allowing slower cooling of the core under a gradual reduction of the local pressure [28], [34].

3. THERMOMECHANICAL INDICES

The mechanical properties of polymers, especially semi-crystalline ones, are highly dependent upon the morphological development and cannot be related to one single factor. The establishment of quantitative relationships between processing, morphology and mechanical properties in injection moulding remains an open issue, which creates the need for developing engineering methodologies that, even with empirical and phenomenological approaches, can handle this reality. In 2013 [32], [47] a methodology was developed to predict local mechanical properties of injection moulded parts based on several thermomechanical variables (TMV) obtained from Autodesk Moldflow Insight in a filling, packing and cooling simulations and the TMI. A software was developed which consisted in importing relevant results from the computer flow simulations and, accordingly, predict the mechanical properties of a 2.5D finite-element model mesh (triangular elements on surface of the model). The application computes the mechanical properties (per element of a dual domain mesh) based on the TMI equations and a set of regression equations resulting from both simulations and experimental analysis. The user only imports the TMV into a root directory, grouping them into three distinct modules:

- Geometrical definition of the component;
- Set of processing conditions, including material-specific properties;
- TMV for all the time instants of the injection moulding process.

The thermomechanical variables are:

The bulk temperature (T_b), which is a weighted average temperature across the thickness of the moulding. The temperature of polymer melt changes not only with time and location but also with the thickness during the entire injection moulding cycle. It represents the energy that is transported through a particular location and is defined by equation 1.

$$\overline{T_b} = \bar{T} + \frac{\frac{1}{h}\int_0^h (T(z) - \bar{T})v(z)dz}{\int_0^h v(z)dz} \quad (1)$$

Where, $\overline{T_b}$ is the bulk temperature, $\bar{T}$ the average temperature, h the thickness of the part, v (z) the local velocity (through the thickness) and T (z) the temperature profile in the thickness direction.

The shear stress at wall (τ_w), which is the shear force at the frozen/molten interface, per unit area, and is proportional to the pressure gradient at each location. The shear stress is also an indirect indication

of the degree of molecular orientation since a higher shear stress would induce higher orientation, especially near the surface of the part.

The bulk shear rate ($\dot{\gamma}$). This parameter is derived from the shear stress at wall, the representative viscosity (η_{rep}) and thickness of the part, calculated from the fluidity (S), equation 2. It is a measure of how quickly the layers of plastic are sliding past each other. If this happens too fast, the polymer chains break and the material degrades. In contrast to the bulk temperature, the bulk shear rate is not an average or weighted average of the shear rate because it can vary widely across the part thickness.

$$S = \frac{H^3}{3\eta_{rep}};\ \dot{\gamma} = \frac{\tau_w}{\eta_{rep}} \tag{2}$$

Finally, the frozen layer fraction (FLF). It is not strictly a TMV but rather the result of the relationship between TMV. It presents a value varying between 0 and 1 and resents the fraction of the frozen layer thickness during the IM cycle. This parameter establishes a relationship between the temperature calculated in the finite element model at each given time with a transition temperature, which in case of semi-crystalline polymers is the crystallization temperature. The polymer is considered to be frozen when the temperature falls below the transition temperature.

Viana et al. [35] first introduced the derivation of two TMI. The cooling index(Y), CI, equation 3, which characterises the thermal level of the moulding and is defined as the ratio between the superheating degree and the cooling difference. It indirectly quantifies the crystallinity level of the core. Lastly, the thermal-stress index (τ_Y),TSI, equation 4, defined as the ratio between the level of molecular orientation imposed during the mould filling (indirectly assessed by the shear stress at the solid/liquid polymer interface, τ_w) and the level of molecular relaxation occurring during cooling (assumed proportional to the CI). Both TMI were derived for the end of the filling stage in 1997, and then, in 2000 to 2002 suffered some modifications [34], [35].

$$Y_c = \frac{T_b - T_c}{T_b - T_{int}} \tag{3}$$

$$\tau_Y = \frac{\tau_w}{e^Y} \tag{4}$$

Where T_c is the crystallization temperature; T_{int}, the temperature at the mould-polymer interface (equation 5), defined as an average temperature of the polymer (script$_{-m}$) and mould (script$_{-w}$) weighted by their thermal effusivities (b), equation 6.

$$T_{int} = \frac{b_w T_w + b_m T_b}{b_w + b_m} \tag{5}$$

$$b = \sqrt{\rho K C_p} \tag{6}$$

ρ is the density, K the thermal conductivity and C_p the heat capacity,

In more recent years, the TMIs have been subjected to improvements. Barbosa et al. [47], [48] proposed equations for the packing and cooling stages. In their report [47] the CI at the end of packing and cooling was calculated as a weighted average by the relative duration of each phase, equations 7 and 8.

$$Y_c^{fp} = \frac{Y_c^f t^f + |Y_c^p| t^p}{t^f + t^p} \tag{7}$$

$$Y_c^{fpc} = \frac{Y_c^f t^f + |Y_c^p| t^p + |Y_c^c| t^c}{t^f + t^p + t^c} \tag{8}$$

Y_c^f, Y_c^p Y_c^c, and t^f, t^p, and t^C are the filling, packing and cooling indices and durations, respectively. The packing time is defined at the element level and its value taken from the instant right before the pressure drops to 0. The cooling time was defined as the time needed for the FLF to be equal to 1.

The calculation of the cooling index exclusively for an individual phase can done resorting to equation 3 and substituting T_b, T_{int}, and T_c for their respective value at the end of each phase. T_c can be estimated by equation 9.

$$T_c = T_c^* + b_6 P \tag{9}$$

Where T_c^* is the crystallization temperature at ambient pressure (assumed constant), b_6 a constant and P the maximum pressure at the end of the filling, packing or cooling stages.

The calculation of shear stress at the end of the packing and cooling stages was done analogously to the CI, where a weighted average was calculated, equations 10 and 11.

$$\tau_w^{fp} = \frac{\tau_w^f \times FLF^f + \tau_w^p (FLF^p - FLF^f)}{FLF^p} \tag{10}$$

$$\tau_w^{fpc} = \tau_w^f \times FLF^f + \tau_w^p (FLF^p - FLF^f) \tag{11}$$

The calculation of the TSI at the end of each respective phase can be done by applying equation 4 and substituting the shear stress at wall and the CI by their respective values.

A computational flow chart of this methodology is illustrated in Figure 3.

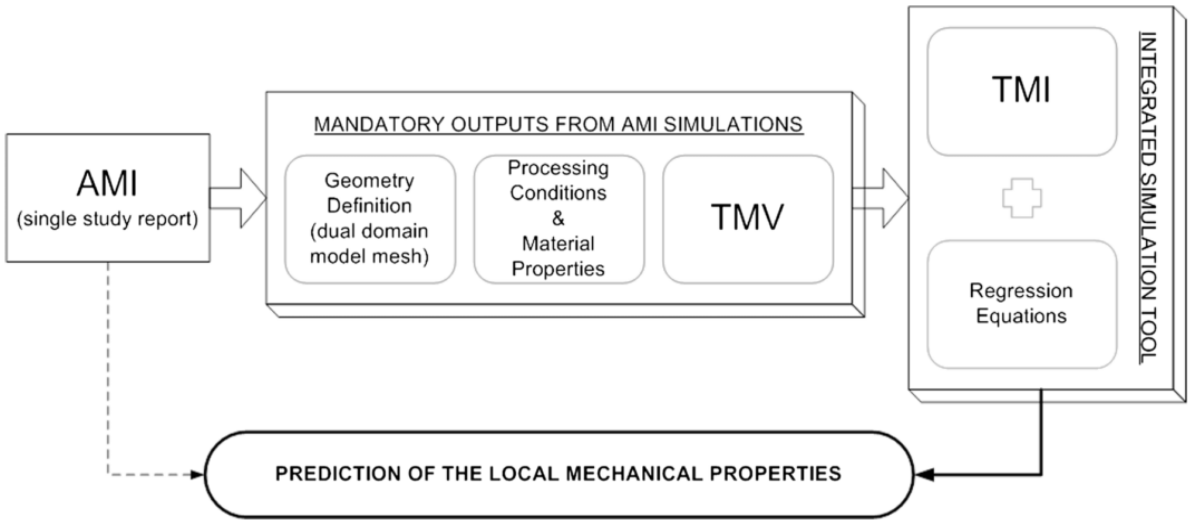

Figure 3: Flow chart for the prediction of mechanical properties through thermomechanical indices [32]

4. MATERIAL

Polypropylene (PP) was first produced by Guilio Natta, following the work of Karl Ziegler, by the polymerization of propylene monomers (Figure 4) in 1954 [49].

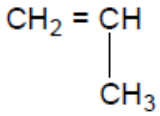

Figure 4: Polypropylene monomer

This semi-crystalline material can be divided into two different categories: homopolymer (hPP) and copolymer (cPP). The first consists of molecular chains with repeating units of polypropylene monomer. This monomer can be obtained from several different sources being the most common the steam cracking process using naphtha. The copolymer is obtain by mixing PP monomer at the first stages of polymerization with ethylene or with another comonomer such as butane [50]. An important subtype of cPP, which is used in several automotive applications, is the impact-resistant polypropylene copolymer (IPC). This polymer is prepared by a two-step polymerization: bulk polymerization of propylene and then a gas-phase copolymerization of ethylene and propylene [51]. Several authors identified 3 types of composition in IPC, ethylene-propylene random copolymer (EPR), ethylene- propylene block copolymers and propylene homopolymer [51].

Polypropylene has an asymmetric carbon and can be found in three types of spatial configuration. If the methyl groups (CH_3) are on the same side of the polymer chain, the resulting product is referred to as isotactic PP. If the methyl groups are placed in an alternating position along the polymer backbone the result is a syndiotactic PP, and, if they are displaced in a random way the result is the atactic form (Figure 5).

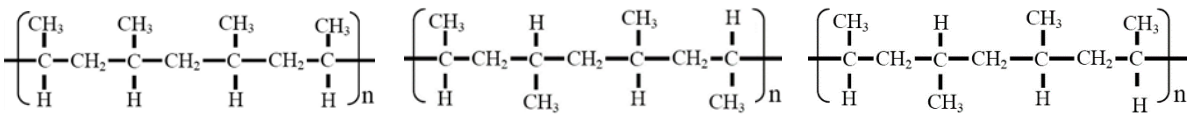

(a) (b) (c)

Figure 5: Polypropylene stereochemical configuration: a) Isotactic; b) Syndiotactic; c) Atactic

Polypropylene also exhibits polymorphism and may display up to four different crystal modifications: α, β, γ and a mesomorphic phase. Housmans et al. [4] cited that under standard conditions occurs the

formation of the α-phase with a monoclinic crystal structure characterised by the cross-hatching or lamellar branching, consisting of a daughter lamellae that grows on top of the initial (mother) lamellae. The β-phase with its trigonal unit cell is formed in the presence of a temperature gradient [52], strong imposed molecular orientation [11] or with the addition of nucleating agents [53]. The occurrence of the γ phase, with its orthorhombic unit cell, can be originated due to low stereo-regularity of the chains [54], low molecular weight [54], pronounced molecular orientation [55], and copolymerization (e.g., with ethylene) [56]. Finally the mesophase, containing a pseudo-hexagonal unit cell is formed under high cooling rates [4], [57].

5. DESIGN OF EXPERIMENTS AND ANALYSIS OF VARIANCE

In general the design of experiments (DOE) can be defined as a rigorous, systematic method to solve engineering problems in a process/system, applying principles and statistical techniques at the data collection stage to ensure the generation of valid, defensible, reproducible, and supportable conclusions. In addition, all of this is carried out in order to ensure minimal time and monetary expenses.

A process can be defined as the transformation of inputs into outputs. In the context of manufacturing, the inputs can be regarded as materials, processing conditions, procedures, etc. and the outputs (also referred to as the responses) can be the quality or a performance characteristics of a product, Figure 6. In a process, there are variables which the user can easily vary during an experiment who have a key role in the characterisation process. On the other hand, there can also be uncontrollable variables which are responsible for variability in the system. The knowledge of these and their influence is fundamental for the strategy of robust design [58].

When performing a DOE, intentional changes in the inputs will be made in order to observe changes in the outputs. There are several DOE techniques, like the Taguchi method [32], response surface methodology [59] and central face composite [28], among others, which several authors have used in order to define and study the optimization of different parameters in the injection moulding process.

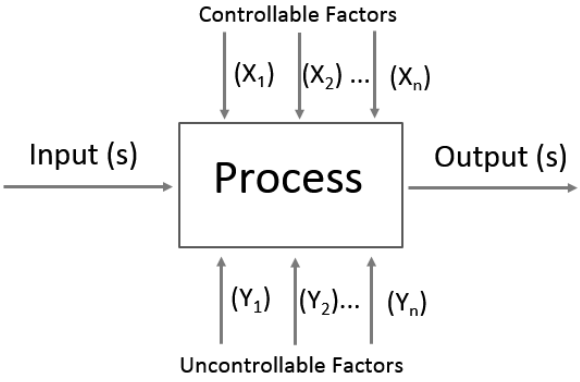

Figure 6: General model of a process/system

The use of statistical methods have a great importance in the conduct, analysis and interpretation of engineering data. The analysis of variance (ANOVA) is used to compare the variance within a data population (factors) and is usually implemented with DOE plans. This statistical procedure has been used by some authors [48], [60] to evaluate the trend and contribution of operative variables on a certain response. It is a statistical method based on the Fisher-Snedecor distribution that subdivides the total

variance within a specific set of data associated with specific sources of variation, in order to test a hypothesis (null hypothesis test) on the model's parameters. This null hypothesis tests checks if:

- The mean of each data population (factor) is the same for all conditions;
- The mean of each data population is different for all conditions.

If the test is true, for a certain degree of confidence (α), then the factor in question does not affect the response. If the hypothesis is rejected, at least one parameter is significant for the model and it influences the response. The mathematical derivations of this statistical analysis are not mentioned in this thesis, however, they can be accessed in [61].

6. CHARACTERISATION TECHNIQUES

6.1 Polarised Light Microscopy (PLM)

There are several techniques to observe the morphology of amorphous and semi-crystalline polymers. The knowledge of the interaction between electromagnetic waves and matter is of crucial importance for the selection of the adequate technique.

The image that is sought to reproduce the microstructure of a material must be in sufficient resolution, contrast and magnification to allow a comfortable observation. Polarised light microscopy (PLM) consists of a typical microscope combined with two polarised filters perpendicular to each other, one after the objective lens (analyser) and the other before the condenser lens (polarizer).

Light is an electromagnetic wave that propagates in all directions and when it contacts the polarizer, part of it is filtered and the resulting wave only propagates in one direction. If this polarised light goes through the sample without changes in the polarization plane it will be absorbed by the analyser and, as a result, the obtained image will be completely black. This phenomenon is called the extinction position and reflects the quality of the polarizers. Most efficient polarizers are made of transparent crystals, such as calcite, but light can also be polarised by using a sheet of aligned long-chain polyvinyl alcohol molecules impregnated with aligned microcrystals of polyiodide, like the one introduced by the Polaroid Company [62].

In the characterisation of polymeric materials the use of PLM can be seen in the:

- Detection and measurement of birefringence in films and moulded parts [63];
- Observation of the crystalline morphology of semi-crystalline polymers [5], [28], [64];
- Identification of additives [65] (e.g. fillers and reinforcements);
- Observation and measurement the optical fusion and crystallization point of semi-crystalline polymers (when the microscope is incorporated with a hot plate) [66].

In literature, semi-crystalline materials who are injection moulded develop a sandwich like structure. Near the mould a crystalline structure who is highly oriented, usually referred to as the skin layer is developed and, moving away from the mould wall, the material has more time to crystalize resulting in morphological structures with different shape and dimensions (core). The dimensions of these structures are dependent upon the thermomechanical history developed during the IM cycle and result in different mechanical properties, both along the thickness and the flow direction [64].

With the images taken from PLM one can calculate the skin ratio (Sa). This parameter intends to quantify the amount of oriented material developed during the IM process.

6.2 X-Ray Diffraction (XRD)

X-Rays are a high energy type of electromagnetic radiation, table 1. They were discovered by Wilhelm Conrad Röntgen in 1895 [67] and nowadays serve in a lot of applications, ranging from medical to security procedures (e.g., tomography and airport security).

In the case of polymeric materials the use of X-ray methods are an important characterisation tool that provides important solid-state structural information ,e.g., identification of phases, degree of crystallinity, crystallite size, molecular orientation, and identification of structural parameters (e.g., the unit cell parameters) in unknown crystalline materials.

Table 1: Electromagnetic Spectrum. Adapted from [68]

Wavelength	Frequency	Range	Wavelength (m)	Frequency (Hz)
Low	High	Gamma radiation	$< 10^{-11}$	$> 10^{19}$
↓	↑	X-Ray radiation	10^{-9}- 10^{-11}	10^{17}- 10^{19}
		Ultraviolet radiation	10^{-7}- 10^{-9}	10^{14}- 10^{17}
		Infrared radiation	10^{-5}- 10^{-7}	10^{12}- 10^{14}
		Microwave radiation	10^{-2}- 10^{-5}	10^{9}- 10^{12}
High	Low	Radio waves	$> 10^{-2}$	$< 10^{9}$

In principle, the x-ray equipment measures the flux of x-ray photons (scattered radiation) as a function of the diffraction angle (θ).

There are two main types of X-Ray scattering techniques, small angle x-ray scattering (SAXS) and wide angle x-ray scattering (WAXS). The main difference between the two is the sample-to-detector distance (R). In WAXS, short distances between sample and detector are used, usually ranging from 0.05-0.2 m and in SAXS, distances from 1-3 m [69]. There are variances (subareas) in this two techniques, e.g., middle angle x-ray scattering and ultra-small angle x-ray scattering) which result in a different type of scale resolution. Stribeck [69] displayed the subareas of x-ray scattering as a function of R, assuming the wavelength (λ) produced by Cu (0.15418 nm). The results are presented in Table 2.

Table 2: Subareas of scattering as a function of the sample-to-detector distance, [69]

Subarea	R (m)	Focus
WAXS	0.05 – 2	Arrangements of chain segments
MAXS	0.2 – 1	Liquid-crystalline structure
SAXS	1 – 3	Nanostructure 3-50 nm
USAXS	6-15	Nano and microstructure 15-2000nm

There are two types of setup schemes for the scattering experiments. In symmetrical-transmission mode the radiation from a source (1) is monocromatised and collimated by the incident beam optics (2). A beam passes through the sample (3) and is decomposed into a primary and diffracted components. The primary beam (unscattered) hits a beam stop (5) and the diffracted beams the detector (4). This setup allows the change of the sample-to-detector distance enabling the use of WAXS and SAXS but requires the use of 2D detectors, Table 2 and Figure 7. In a symmetrical- reflection x-ray setup the angle θ changes while recording the intensity of the scattered radiation being measured, typically, by a linear detector [70].

Some polymers, like polypropylene, have the capability of crystallization and polymorphism which in due turn contribute for the mechanical response of the material, thus rendering important the quantification of these morphological features.

Crystals are defined as a periodic atomic or molecular array with tridimensional shape. The unit cell is the simplest repeating unit in a crystal and their periodic arrangement is called a lattice. They are defined by three axes (abc) and the angles between them ($\alpha\beta\gamma$), Figure 8. In 1845, August Bravais demonstrated the existence of 14 types of lattices within 7 crystal systems. The lattices are classified as follows: simple, body centred, face centred and base centred. The crystal systems as: cubic, trigonal, monoclinic, orthorhombic, tetragonal, triclinic and hexagonal [71].

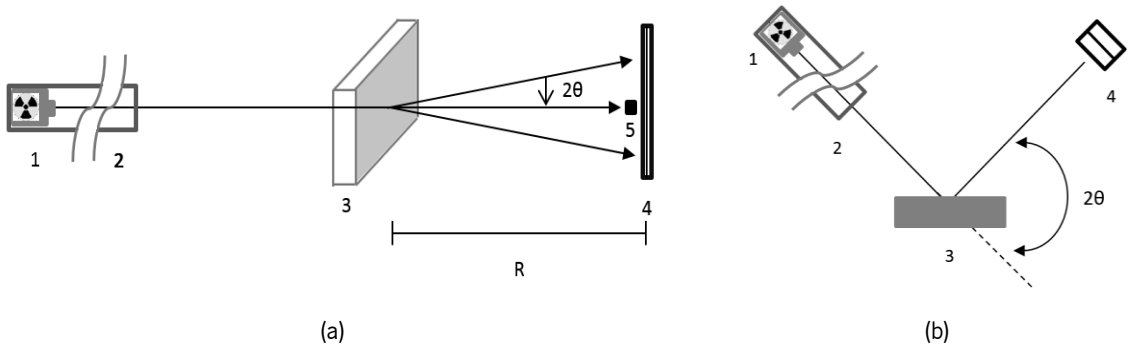

(a) (b)

Figure 7: X-ray setup a) Transmission setup; b) Reflection setup, 1-X-ray source; 2- Beam optics; 3- Sample; 4- Detector; 5- Beam stop; R- Sample-to-detector distance. Adapted from [70].

Table 3 presents a resume of the crystal systems and lattices along with the cell parameters of each system. In 1839, W.H Miller proposed a methodology to describe the facets or internal planes of a crystal structure in relation to the unit cell axes though a series of indices (h,k,l). They are characterised, among other things, by describing the angular position to the crystallographic axes but not their actual distances to the origin. Only the ratio of these indices are important, e.g., (330) (220) (110) represent the same set of planes. Also, when a plane is parallel to a coordinate system the miller index assumes the value 0 [72].

Table 3: Crystal systems and types of lattices. Adapted from [72]

Crystal System	Unit Cell Characteristics	Lattice Type			
		Simple	Base Centred	Body centred	Face centred
Cubic	$\alpha = \beta = \gamma = 90^\circ$ $a = b = c$	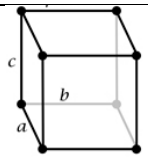		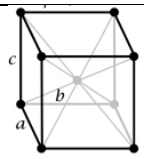	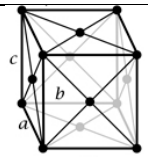
Tetragonal	$\alpha = \beta = \gamma = 90^\circ$ $a = b \neq c$	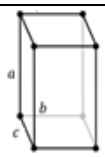		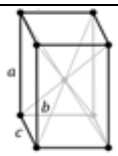	
Hexagonal	$\alpha = \beta = 90^\circ$ $\gamma = 120^\circ$ $a = b \neq c$				
Trigonal	$a = b = c$ $\alpha = \beta = \gamma \neq 90^\circ$	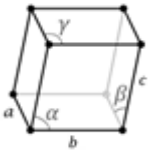			
Orthorhombic	$\alpha = \beta = \gamma = 90^\circ$ $a \neq b \neq c$	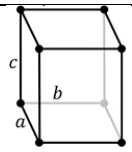	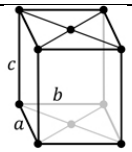	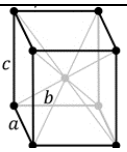	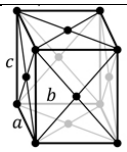
Monoclinic	$\alpha = \gamma = 90^\circ \neq \beta$ $a \neq b \neq c$	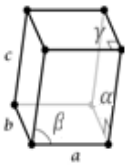	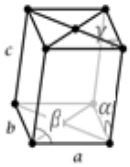		
Triclinic	$\alpha \neq \beta \neq \gamma \neq 90^\circ$ $a \neq b \neq c$	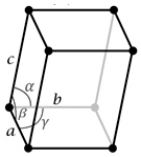			

The interaction between solid matter and x-rays is of fundamental importance for the analysis and interpretation of data. Their interaction results in two main effects: a) changes in the wavelength of the x-ray radiation, the so called Compton's or incoherent scattering, where energy transfer occurs between the photons and the electrons of the sample; b) without changes in the wavelength of the x-ray radiation (Rayleigh, coherent or elastic scattering) where no exchange of energy between the photons and the electrons of the sample exist. If the scattering waves are coherent (in phase) they interfere in a constructive way and diffracted waves are produced at an angle (2θ) from the incident radiation, if the material has domains, the distance between crystalline planes can be assessed through the Bragg's law, equation 12 and Figure 9.

$$n\lambda = 2d \sin\theta \tag{12}$$

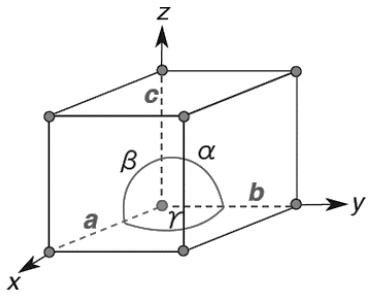

Figure 8: Example of a unit cell

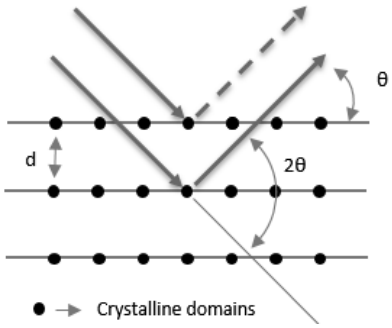

Figure 9: Bragg's law illustration

6.2.1 WAXS Indices

Several morphological parameters can be obtained from WAXS scans, among others are:

- The molecular orientation (Ωs);
- Degree of crystallinity of the skin layer (χ_{skin});
- β-phase content (k- value).

In an orientated semi-crystalline polymer the intensity of each reflection is dependent on the azimuthal angle. Typically, the distribution orientation functions are obtained through the construction of pole figures with the further determination of the Hermans orientation number along the machine, transverse and normal directions [8]. However for polypropylene, Zipper et al. [73] derived two orientation indices (A_{110} and A_{130}), equations 13 and 14, which reflect the α-crystallite orientation along the flow direction,

i.e., for A=1 for highly oriented α-crystallites, otherwise A < 1. This method was also performed by other authors [10], [74].

$$A_{110} = \frac{I_{110}}{I_{110} + I_{111} + I_{131+041}} \quad (13)$$

$$A_{130} = \frac{I_{130}}{I_{130} + I_{111} + I_{131+041}} \quad (14)$$

The skin crystallinity index (χ_{skin}) can be calculated by doing the ratio between the area of the crystalline peaks (A_{crist}) and the total area, given by the sum of A_{crist} and the area of the amorphous hallo (A_{am}), equation 15. This method has been used by several authors [10], [13] to evaluate the crystallinity of semi-crystalline polymers.

$$\chi_{skin} = \frac{A_{crist}}{A_{am} + A_{crist}} \quad (15)$$

The β-phase content (k-value), equation 16, is a concept introduced by Turner Jones et al. [75] and is a semi-quantitative manner to quantify the β-spherulitic population. It correlates the areas of the three strongest α-reflections (110), (040) and (130) with the strongest β reflection (300). For a 100% α-PP k =0; and for a 100% β-PP, k =1.

$$k - value = \frac{A_{300}^{\beta}}{A_{110}^{\alpha} + A_{040}^{\alpha} + A_{130}^{\alpha} + A_{300}^{\beta}} \quad (16)$$

The diffraction peaks angles, Miller index and crystal form for an iPP are summarised in Table 4.

Table 4: Diffraction angle, θ, and the corresponding Miller indices and crystal form. Adapted from [4]

Miller Index (hkl)	2θ	Crystal form
110	14.1	α
300	16.1	β
040	16.9	α
130	18.5	α
111	21.3	α
131/041	21.9	α
150/060	25.4	α
200	27.2	α

6.3 Differential Scanning Calorimetry (DSC)

Differential Scanning Calorimetry (DSC) is a thermoanalytical technique that dates from the early 1960's when Perkin-Elmer marketed their DSC-1, the first DSC [76].

Figure 10 illustrates the general scheme of a DSC apparatus. It is mainly constituted by:

- Two separated furnaces with their respective heaters and thermocouples;
- A computer for data acquisition and control of the electrical power output.

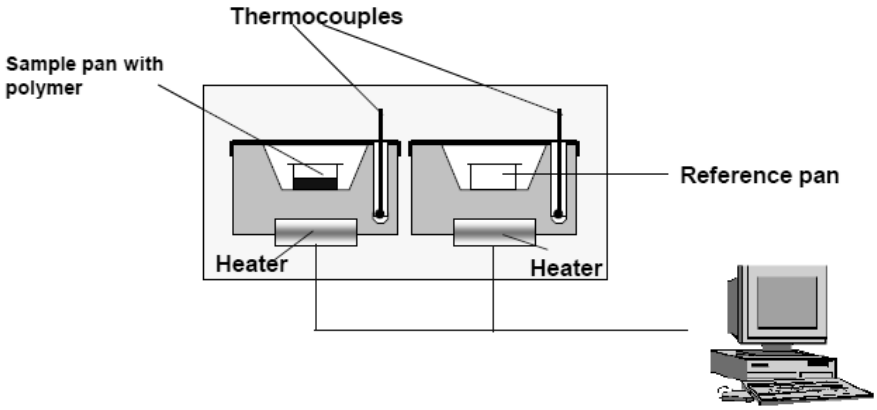

Figure 10: Scheme of a DSC apparatus

In this technique, the energy needed to establish a temperature difference $\Delta T = 0$ between the sample and a reference (empty pan), as a function of time or temperature, is registered. The measurement can be done during heating or cooling using a given heat rate within a pre-defined temperature range. The reference and sample are placed exactly at the same temperature conditions, and during the whole process an inert gas is circulating in the furnaces, typically nitrogen, who due to its high thermal conductivity is used to purge the atmosphere, allowing the stabilization of the temperature during the test and also preventing the oxidative degradation of the material.

The results obtained in a DSC test are presented in the form of a graphic relating the heat flow (W/g) with temperature (°C), from which it is possibly to obtain resulting regarding the:

- Glass transition temperature (T_g) – Defined as the temperature at which the conformational mobility of the liquid phase is no longer detected in the experimental time scale. In a DSC test (during heating) when passing through T_g, there is a change in the heat capacity without involving latent heat. This is defined as a second-order transition.
- Crystallization Temperature (T_c) – Temperature at which the macromolecules of semi-crystalline polymers gain enough energy to reorganize and form ordered arrays (semi-crystalline areas). The crystallization process is an exothermic process. The heater from the

sample side stops supplying heat, and an exothermic peak (depression/ dip) is observed in the DSC curve (Figure 11).

- Melt Temperature (T_m) – An increase in temperature can cause a semi-crystalline polymer to form crystalline areas, but continuing its increase another thermal transition is reached, the melting temperature. In this transition the crystalline areas are destroyed. The increased amount of energy is displayed in the form of an endothermic peak in the DSC curve (Figure 11).

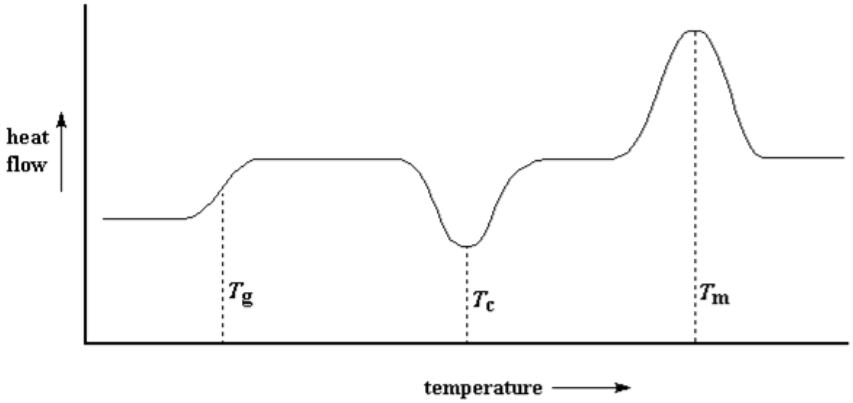

Figure 11: Example of a DSC curve of a typical semi-crystalline polymeric material

DSC is also used to assess the percent/ degree of crystallinity (χ_c) in a polymeric sample. When heating, χ_c is equal to the difference between the heat of fusion (ΔH_f) and crystallization (ΔH_c) divided by the equilibrium heat of fusion (ΔH_f°), equation 17.

$$\chi_c = \frac{\Delta H_f - \Delta H_c}{\Delta H_f^\circ} \tag{17}$$

6.4 Tensile tests

6.4.1 Quasi-Static

Tensile properties are widely used both to assess mechanical properties for the design of parts in engineering applications and as quality control. Several standard procedures exist for plastic materials, like the ISO 527 and ASTM D638, which contain the geometry of specimens, test velocities and the procedure for assessing the tensile properties in quasi-static conditions. In this type of tests, a specimen, typically with a dog-bone shape (Figure 12) is gripped at its two ends and extended along its major

longitudinal axis at constant speed until it fractures or the stress (load) or strain (elongation) reaches a predetermined value. Testing machines can be either electromechanical or servohydraulic, the main difference being the way by which the load is applied. The electromechanical systems employ a gear reduction system, screws that move the crosshead and a variable-speed electric motor. On the other hand, the servohydraulic systems are based on a single or dual-acting piston that move the crosshead up and down [77].

When a solid material is subjected to small stresses, the bonds between the atoms are stretched and, when removed, the bonds relax and the material returns to its original shape. This reversible deformation is called elastic deformation and is present in the initial portion of the stress- strain (σ - ε) curve by a linear region from which it is possible to assess the elastic or Young modulus (E), equation 20. When the applied stress becomes high enough, planes of atoms start to slide past each other and the deformation is not recovered when the stress is removed, the linear stress-strain behaviour will cease to exist and the strain will not disappear upon unloading. This is termed as plastic deformation and the stress point at this yielding phenomena is called yield stress.

In general all polymers, who are not cross-linked, show a decrease in the cross section of the gauge length in a localised region of the specimen. This phenomena is called necking. Once the specimen has necked as much as possible, the cross-section will be uniformly thin and with an increase in the strain, the stress will also rise and the specimen will break shortly after the necking ends [78].

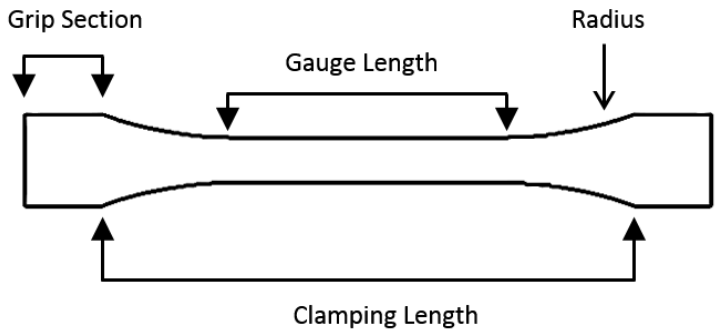

Figure 12: Typical dog-bone geometry used in a tensile test

The output of this test is a force vs elongation plot which for engineering purposes is transformed into an $\sigma - \varepsilon$ curve, Figure 13, to account for the cross-sectional area of the specimen. Equations 18 and 19 are used in construction of this curve. The ISO 527 defines the yield stress (σ_y) as the first stress at which an increase in strain occurs without an increase in the stress; the stress at break (σ_b) as the tensile stress

at which the test specimen ruptures; and the tensile strength (σ_M) as the maximum tensile stress sustained by the test specimen during a tensile test, which in the case of Figure 13 is also σ_b.

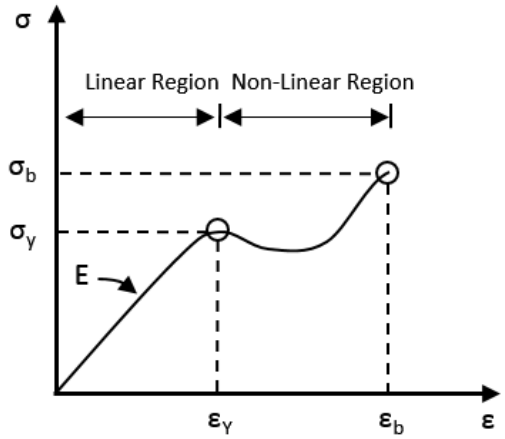

Figure 13: Example of a stress-strain curve

Figure 14 shows some different types of tensile curves dependent upon the nature of the material. When fracture occurs in a sudden way and for low values of deformation it is said that the material presents a brittle fracture (Figure 14, A). In this cases the yield stress and the tensile stress at break can coincide and the modulus is, generally, elevated. A ductile fracture is observed when the $\sigma - \varepsilon$ curve presents relatively high deformations with or without a well-defined yield point (Figure 14, B, C and D). Since polymers are viscoelastic materials their complex deformation behaviour is dependent upon several factors. The shape of the curve and the type of fracture can vary with different specimen preparation methods, test speed and environmental parameters such as temperature [24], [79].

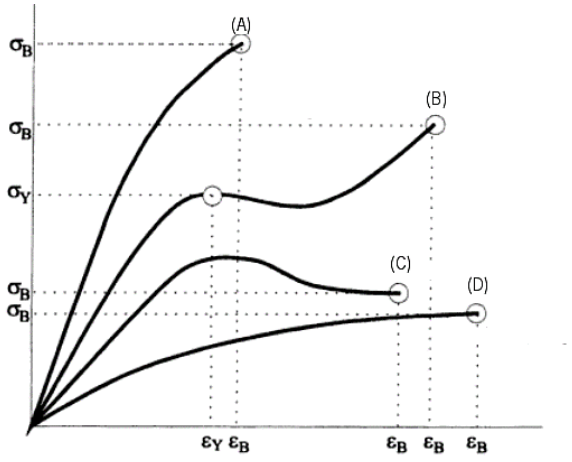

Figure 14: Types of fracture of unfilled polymers: A) Brittle; B) and C) Tough material with yield point; D) Tough material without a yield point. Adapted from [80]

$$\sigma_e = \frac{F}{A} \tag{18}$$

$$\varepsilon_e = \frac{\Delta L}{L_0} \tag{19}$$

$$E = \frac{\sigma}{\varepsilon} \tag{20}$$

Where F is the tensile force, A the cross-sectional area of the gauge section; L_0 the gage length and ΔL the displacement.

In the engineering approach the specimen geometry is assumed constant throughout the test. However, in reality, it changes, therefore changing the local values of σ and ε. ASTM D638 defines a type of curve (homogeneous) that takes into account the changes in the cross-sectional area of the specimen by assuming that the deformation is homogeneous (Hencky/ True strain) and the material incompressible, equations 21 and 22. Nevertheless, in the neck zone the deformation can be highly localised and so, particularly non-homogeneous. Typically the homogeneous curve as validity up to the end of the elastic/yield limit (before necking occurs) where the deformation is supposedly homogeneous.

To truly observe the behaviour of a material under tensile loadings the σ and ε must be defined relatively to the instantaneous local dimensions of the specimen (True stress- True strain). However, this curve at constant strain- rate is only available when specific experimental techniques are employed.

$$\varepsilon_{true} = \ln(1 + \varepsilon_e) \tag{21}$$

$$\sigma_{hom} = \sigma_e(1 + \varepsilon_e) \tag{22}$$

Data from one of the tested experiments was treated to plot the curves in Figure 15 in order to display the evolution of the different definitions of tensile curves. Two main differences can be emphasised:

- The low σ and high ε values of the engineering definition;
- A similar evolution of the homogeneous and true stress curve. However when the necking phenomena becomes accentuated a clear difference is observable.

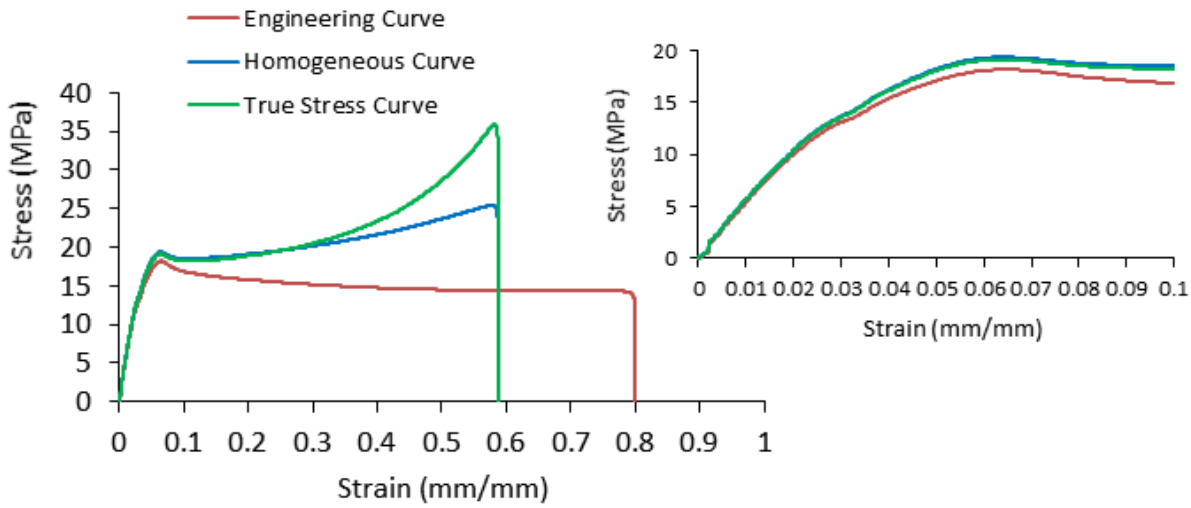

Figure 15: Difference in the tensile curves for experiment E2

6.4.2 High Speed

Common quasi-static tests are comprised in a strain-rate between 10^{-4} to 10^{-1} s^{-1} whereas high speed, or dynamic tensile tests start at a strain-rate above $10^{-1}s^{-1}$ when the inertia forces become important. The dynamic testing is further divided into two categories: i) intermediate rate testing, which covers the range 10^{-1} to 10^{2} s^{-1} and ii) high rate testing, which starts at 10^{2} s^{-1} when the elastic-plastic wave-propagation effect becomes important [81]. The characterisation of mechanical properties at high testing speeds has special importance for the acquisition of data to introduce in finite element analysis software, in particular, crash simulations. The common strain-rates recorded in vehicle crash simulations covers a range from 0.01 to 500 s^{-1} [27]. The properties of these materials can be studied experimentally using different techniques (Figure 16), such as high speed tensile tests [24]–[26], [79], [82] performed on servo-hydraulic tensile machines, impact tests (e.g., instrumented falling weight impact test, tensile impact) [83]–[85] and the split Hopkinson pressure bar method [86].

There aren't a lot of studies regarding high speed tensile tests on polymeric materials [24]–[27] mainly because no standard procedure exists, only a recommended practice guide emitted by the International Society of Automotive Engineers (SAE) [27], [23]. For the specimen configuration, some authors used the ISO 8256 [24], [25] while others opted for the ISO 572-2 [26] and the ASTM D638 [27]. All of these standards have some suggested configurations present in the SAE practice guide.

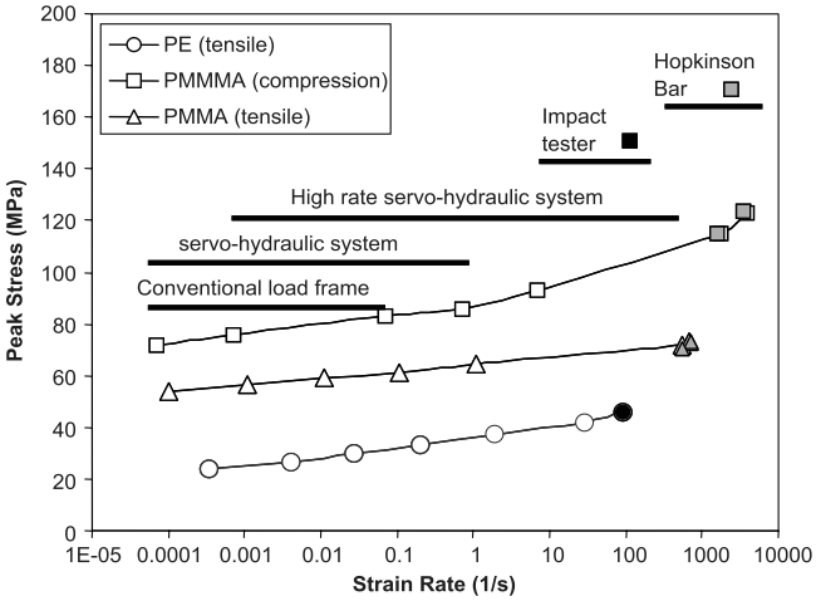

Figure 16: Typical strain rates covered by conventional load frame, servo-hydraulic system and Hopkinson bar system [27].

In high speed tests the stress signals are more and more superimposed by oscillations with increasing strain-rate due to the impact resulting from the coupling of the pre-accelerated piston to the sample [25]. The impulse during the load application, if it not properly damped, can cause the test system to oscillate resulting in a phenomenon called ringing [27]. This produces a high amplitude stress pulse and non-homogeneous deformation in the specimen. Stress waves of varying amplitudes are present in the gauge section during a high strain-rate test and a homogeneous stress state does not exist. The goal, in order to obtain valid data, is to introduce enough stress waves (at least. 10 to 15) in the gauge area to produce an approximate equilibrium, thus a "quasi- homogeneous" stress and strain field will exist and the nominal stress and strain states can be defined [23]. The SAE “standard” offers an equation (equation 23) to assess a low estimative of the number of stress waves (N) in the gage section up to the time of yield. However this calculation will not be made in this thesis.

$$N \approx \frac{\varepsilon_y L_g c_{fixt} c}{V\left(L_{fixt} c + L_g c_{fixt}\right)} \tag{23}$$

Where L_g the distance between grips, c is the elastic stress wave velocity of the specimen material, V the displacement velocity of the crosshead, L_{fixt} is the length of the fixture and, c_{fixt} the elastic stress wave velocity of the fixture material.

7. EXPERIMENTAL PROCEDURE

7.1 Material

The material used in the injection moulding process was a compounded polypropylene from Lyondell-Basell (Hostacom EP 3307). In the datasheet of the material it is mentioned that it has low density, UV stabilizers, good impact resistance combined with high fluidity and its primary use is for interior trim. The main properties from the datasheet are listed in Table 5.

Table 5: Properties from the data sheet of PP Hostacom EP3307

	Method	Value	Units
Physical Properties			
Density	ISO 1183	0.92	
Melt Flow Rate	ISO 1133	15	g/10min
Mechanical Properties			
Flexural Modulus	ISO 178	1100	MPa
Notched Izod Impact	ISO 180		
Notch A, 23°C, type 1		40	kJ/m^2
Notch A, -30°C, type 1		5	kJ/m^2

The material used to simulate the IM process was a Moplen EP3307 which is similar to the one used in the IM process with the exception of a choral black pigment presented by the Hostacom grade.

From Autodesk Moldflow Insight database several other properties were acquired. The flow curve, Figure 17, was obtained with the Cross-WLF model (equation 24). This model describes the dependency of the viscosity as a function of temperature (T), shear rate (γ) and pressure (P) following the ASTM D3835 standard.

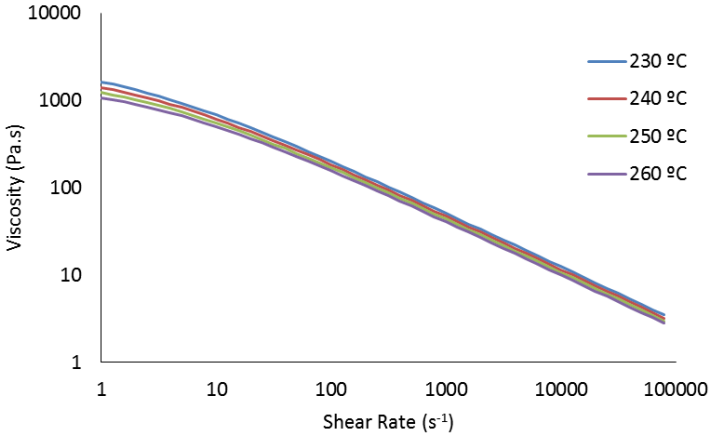

Figure 17: Flow curve from Moplen EP3307

$$\eta = \frac{\eta_0}{1 + \left(\frac{\eta_0 \gamma}{\tau^*}\right)^{1-n}} \tag{24}$$

Where:

η – is the melt viscosity (Pa s);

η_0– is the zero shear viscosity or the 'Newtonian limit' in which the viscosity approaches a constant at very low shear rate, equation 25;

γ – is the shear rate (s^{-1});

τ^* – is the critical stress level at the transition to shear thinning, determined by curve fitting (Pa);

n – is the power law index in the high shear rate regime, determined by curve fitting.

$$\eta_0 = D_1 e^{\left[-\frac{A_1(T-T^*)}{A_2+(T-T^*)}\right]} \tag{25}$$

Where:

T – is the temperature (°K);

T^* – is the glass transition temperature, determined by curve fitting, equation 27;

$$A_3 = A_2 - D_3 P \tag{26}$$

$$T^* = D_2 + D_3 P \tag{27}$$

P - is the pressure (Pa);

D_1, D_2, D_3, A_1, and A_2 are data-fitted coefficients.

The values from the coefficients of the cross-WLF model are listed in Table 6.

Table 6: Cross-WLF model coefficients

Cross- WLF model		
n	0.383	
τ^*	4194.08	Pa
D1	4.29308×10^{15}	Pa.s
D2	263.15	°K
D3	0	K/Pa
A1	34.023	
A2	51.6	°K

When processing semi-crystalline polymers a rise in temperature leads to several thermal transitions such as the glass transition temperature (T_g), crystallization temperature (T_C) and melt temperature (T_m).

The PVT diagrams describe the variation in the specific volume (inversely proportional to the density) as a function of pressure and temperature. In the injection moulding cycle the existence of pressure and temperature gradients induces a non-uniform crystallization, resulting in variations of density in the part, leading to the appearance of several defects such as warpage, shrinkage and sink marks. According to Berry et al.[87], the use of polymer PVT data can used to predict, among other things, the polymer-polymer miscibility and the optimization of processing parameters instead of establishing them by trial and error. AMI uses a modified 2-domain Tait PVT model to determinate the density of a material as function of pressure and temperature. This model is governed by equation 28.

$$V(T,P) = V_0(T)\left[1 - C\ ln\left(1 + \frac{P}{B(T)}\right) + V_0(T,P)\right] \quad (28)$$

Where:

V (T,P) – is the specific volume at a certain temperature and pressure;

V_0 (T) – is the specific volume at zero gauge pressure, following equation 29;

T – temperature (°K);

P– pressure (Pa);

C – is a constant ;

B (T) – accounts for the pressure sensitivity of the material and is defined in equation 30.

Above the transition temperature (T_t), which in case of semi-crystalline is the crystallization temperature, V_0 can be described by equation 29.

$$V_0(T) = b_{1m} + b_{2m}(T - b_5) \tag{29}$$

$$B(T) = b_{3m} e^{[-b_{4m}(T-b_5)]} \tag{30}$$

$$V_t(T,p) = 0 \tag{31}$$

Where b_{1m}, b_{2m}, b_{3m}, b_{4m} and b_5 (which represents the volumetric transition temperature, T_t, at zero gauge pressure) are data-fitted coefficients.

Below T_t, the specific volume is given by equations 32- 34.

$$V_0 = b_{1s} + b_{2s}(T - b_5) \tag{32}$$

$$B(T) = b_{3s} e^{[-b_{4s}(T-b_5)]} \tag{33}$$

$$V_t(T,p) = b_7 e^{[(b_3-(T-b_5))-(b_9 p)]} \tag{34}$$

Where b_{1s}, b_{2s}, b_{3s}, b_{4s}, b_5, b_7, b_8 and b_9 are data-fitted coefficients.

The value of V_t for semi-crystalline polymers only applies for temperatures below the transition temperature. The dependence of T_t on the pressure follows equation 35.

$$T_t(p) = b_5 + b_6 p \tag{35}$$

The PVT curve for Moplen EP 3307 is presented in Figure 18.

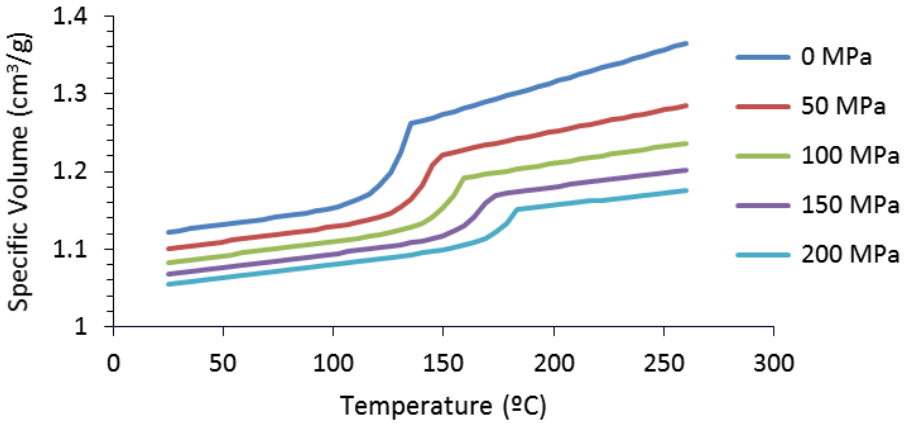

Figure 18: PVT curve for Moplen EP 3307

7.2 Moulding Window Analysis

The processing conditions, namely the injection temperature (T_i), mould temperature (T_w) and maximum and minimum injection times ($t_{i\ min}$ and $t_{i\ max}$) were assessed through Autodesk Moldflow Insight in a moulding window analysis (MWA) simulation in order to ensure feasible processing conditions (Table 7). This analysis uses the part geometry, the selected material and injection location to run a series of calculations varying the process settings each time. For this study a lateral injected disc with 115 mm of diameter and 3 mm of thickness was discretised employing a dual domain mesh with a maximum aspect ratio of 4.1 and a 99.8% of mesh match percentage (Figure 19). The analysis allows the variation of the following parameters:

- Injection time;
- Injection temperature;
- Mould temperature.

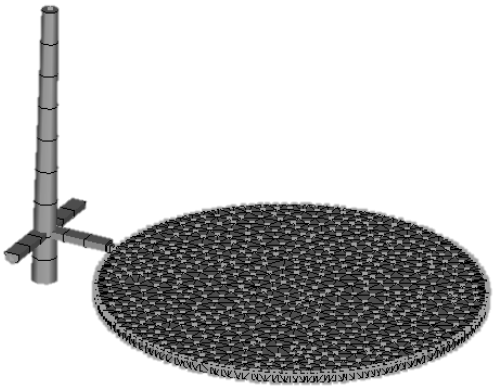

Figure 19: Finite element model (feeding system and part)

The output of this simulation is a graphic showing several coloured regions corresponding to different conditions, i.e., a preferable condition is represented by the colour green, a feasible one by a yellow region and finally, a not feasible or impossible condition with red colouring. The results are shown in Figure 20.

The processing temperatures (T_i and T_w) were defined according to the acceptable limits for this specific moulding. The injection temperature was varied within +/- 30°C in relation to the recommended processing condition (230°C) and the mould temperature +/- 30°C regarding the suggested T_w (40°C).

Table 7: Moulding window analysis conditions: Preferable region

The part is not a short shot	
The injection pressure required to fill the part is less than 50% of maximum machine injection pressure capacity.	$P < 0.5\ P_{max}$
Temperature at the flow front (T_{ff}) is less than 10°C above the injection (melt) temperature.	$T_{ff} < T_i + 10°C$
Temperature at the flow front is greater than 10°C below the injection (melt) temperature.	$T_{ff} < T_i - 10°C$
The shear stress is less than the maximum specified for the material in the material database.	$\tau < \tau_{max}$
The shear rate is less than the maximum specified for the material in the material database	$\dot{\gamma} < \dot{\gamma}_{max}$

The injection times were selected in order to fulfil the frontier conditions established by the moulding window analysis. $t_{i\ min}$ and $t_{i\ max}$ are the minimum and maximum time need to encompass all the conditions. The obtained results are summarised in Table 8.

Table 8: Results from the moulding window analysis

Condition T_i/T_m	$\dot{\gamma}_{max} < 1.0E5\ s^{-1}$	$\tau_{max} < 0.25$ MPa	$T_i - 10\ °C < T_{ff} < T_i + 10°C$	$t_{i\ min}$ (s)	$t_{i\ max}$ (s)
200 / 10	$t_i > 0.0566$ s	$t_i > 0.1294$ s	1.978 s < t_i <0.0786 s	0.129	1.978
200 / 70	$t_i > 0.0566$ s	$t_i > 0.1294$ s	2.860 s < t_i < 0.0761 s	0.129	2.860
260 / 10	$t_i > 0.0566$ s	$t_i > 0.027$ s	$t_i < 1.389$ s	0.056	1.389
260 / 70	$t_i > 0.0566$ s	$t_i > 0.027$ s	$t_i < 1.828$ s	0.056	1.828
Time				0.129	1.389

It can be observed that $t_{i\ min}$ has a value of 0.13s and $t_{i\ max}$ 1.39s. Knowing that the injection flow rate (Q_{inj}) is the product of the material velocity (v) passing through a cross-sectional area (A) and that it may also be given by the ratio between the volume of material passing per unit time, the derivation of equation 36 was carried out in order to determine the maximum and minimum injection velocities.

$$Q_{inj} = \frac{Volume(cm^3)}{time(s)} = Area(cm^2) \times velocity(cm/s) \quad (36)$$

The volume of the moulding (part + feeding system) was obtained by AMI and presents a value of 34.9 cm^3. Knowing that the screw of the IM equipment has a diameter of 40 mm and assuming a constant flow rate during the process, one can assess the injection velocity by rearranging equation 36.

$$v_{inj}(cm/s) = \frac{Volume(cm^3)}{time(s) \times Area(cm^2)} = \frac{Q_{inj}(cm^3/s)}{Area(cm^2)} \quad (37)$$

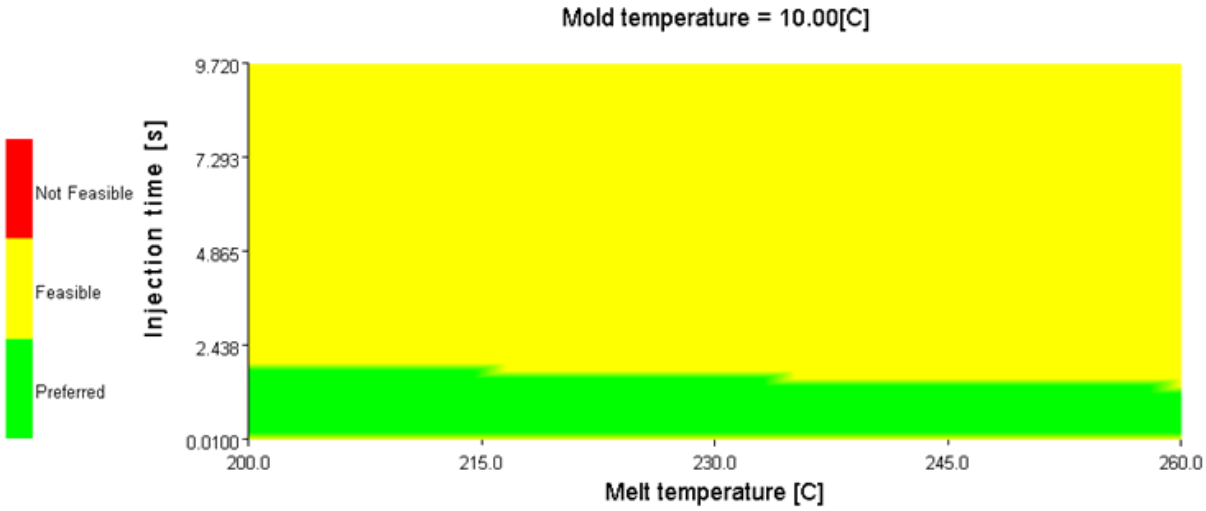

(a)

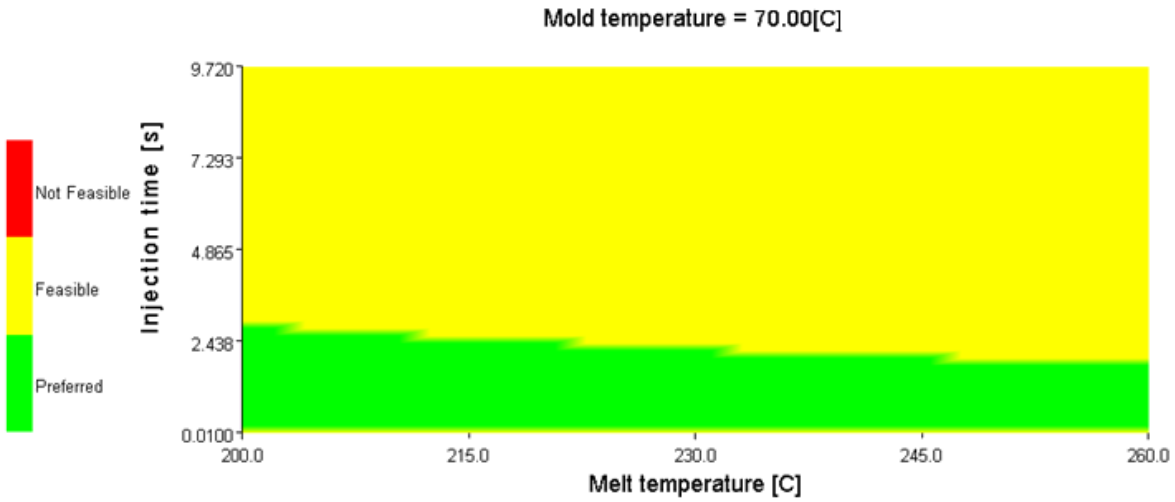

(b)

Figure 20: Graphic visualization of the moulding window analysis: a) Tm= 10 °C; b) Tm= 70°C

The obtained results using the predefined injection times are $v_{i\ max}$= 214 mm/s and $v_{i\ min}$= 20 mm/s. Regarding the holding stage, there isn't a general rule for establishing the correct value for the hold

pressure (P_h). One can assess it by using an empirical approach assuming that the hold pressure generally corresponds to 80-100% of the maximum pressure required to fill the part during the injection phase. However it can be higher or lower in order to obtain good mouldings [88]. The minimum value of this parameter was defined when processing the material, the only criteria was to ensure that the holding pressure could be high enough to guarantee a moulding without sink marks or any other visual defects. The maximum value was set in order to obtain a significant variation of P_h. It was further ensured that the clamping force required to maintain the mould closed was less than 80% of the maximum closing force of the machine.

The setting of the holding time (t_{Ph}) and cooling time (t_c) was made from a gate-seal experiment. This procedure will be explained in section 7.4.

7.3 Design of Experiments and Analysis of Variance

Using a Taguchi orthogonal (L8) array for screening, several combinations of processing conditions were assessed in order to observe their influence on the microstructural development, i.e., the skin ratio (Sa), skin orientation (Ωs), skin crystallinity index (χ_{skin}), β-phase content (k-value) and the bulk crystallinity (χ_{Bulk}) and in some mechanical properties measured in quasi-static and high-speed tensile tests: the yield stress (σ_y), modulus (E) and strain at break (ε_b).

The DOE plan was elaborated with Design Expert 9 trial version (Dx9 t.v.). Four factors were varied within two levels (+ and -): A – Injection velocity (v_i); B – Injection temperature (T_i); C – Mould temperature (T_w); D – Holding pressure (P_h). The L8 offers a type IV resolution, meaning that the main effects will not be confounded but the two factor interaction will. The choice for the levels of variation is presented in the experimental procedure regarding the injection moulding step. Table 9 shows the DOE plan used for this thesis.

The software also allows the use of statistical analysis, namely the use of analysis of variance (ANOVA). It was performed using three criteria:

- The model which encompasses the relevant main factors and interactions must have a significant F-Value, resultant from the Fisher-Snedecor distribution. This value is a test comparing a term's variance with a residual (error) variance. If the variances are close to the same, the ratio will be close to one and it is less likely that the term has a significant effect on the response;

- The difference between an adjusted (adj) and predicted (pred) regression coefficients (R^2) should be less than 0.2, otherwise there may be a problem with either the data or the model The adj R^2 measures the amount of variation around the mean, which is explained by the model and adjusted for the number of terms contained. It decreases as long as the number of terms in the model increase and do not add value to the model. The pred R^2 measures the amount of variation in new data explained by the model;
- The adequate Precision must have a value greater than 4. This parameter quantifies the signal-to- noise ratio and compares the range of the predicted values in the design to the average prediction error.

Table 9: Design of experiments plan

	[A] = v_i (mm.s^{-1})		[B] = T_i (°C)		[C] = T_w (°C)		[D] = P_h (MPa)	
Experiment (E)	Level	Value	Level	Value	Level	Value	Level	Value
1	-	25	-	200	-	10	-	1
2	+	200	-	200	-	10	+	3
3	-	25	+	260	-	10	+	3
4	+	200	+	260	-	10	-	1
5	-	25	-	200	+	70	+	3
6	+	200	-	200	+	70	-	1
7	-	25	+	260	+	70	-	1
8	+	200	+	260	+	70	+	3

7.4 Injection Moulding Plan

For the injection process a Ferromatik- Milacron k85 was used, Figure 21. Using similar results to the ones obtained in the moulding window analysis, 50 lateral injected discs of each condition were produced. The first 10 were discard in order to let the process stabilize, giving a total of 320 used discs. The minimum injection time (0.13 s) was not reachable when moulding the discs. So, in order to avoid flashes and subsequently get feasible mouldings, the maximum injection velocity was set as 200 mm/s resulting in an injection time of 0.23s. The minimum injection velocity was set at 25 mm/s, resulting in an injection time of 1.36 s.

The minimum level of holding pressure was set at 10 bar, being it the minimum value obtain to ensure a moulding without any visual defects. The maximum level was set at 30 bar in order to have a significant variation (3x) of this parameter.

Figure 21: Ferromatik-Milacron k85 injection moulding machine

The holding and cooling times were assessed through a gate seal experiment. The feeding system has a rectangular gate geometry with 2mm of thickness. After establishing the limits of the holding pressure, the holding time (t_{Ph}) was assessed by doing several incremental steps in t_{Ph} and maintaining the rest of the processing conditions. For this, the experiment with the highest values (A+, B+, C+, D+) was used and t_{Ph} increased until the part weight assumed a constant value. Figure 22 shows the results of this test. One can observe that the weight stabilizes roughly at 20s, so this value was taken for all experiments.

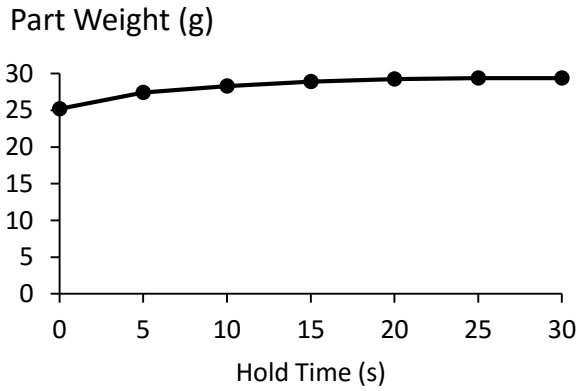

Figure 22: Sample weight variation as a function of the holding time

Afterwards was defined the cooling time. Since it takes around 20s for the gate to freeze one can assume that nearly 2mm of the part is frozen. An empirical method to calculate the cooling time (holding stage included) is given by the equation bellow:

$$t_c = \frac{h^2}{\alpha\,\pi^2}\,Ln\left[\frac{4}{\pi}\left(\frac{T_i - T_m}{T_e - T_m}\right)\right] \tag{38}$$

Where h is the thickness of the part (m), α the thermal diffusivity (m^2s^{-1}) and T_e the ejection temperature (°C). Assuming for PP a thermal diffusivity [42] of 0.65 x 10^{-7} m^2s^{-1}, 3 mm of thickness and that the crystallization temperature (according to Moldflow) is 121°C, the resulting cooling time is equal to 22.12 s. Since the mould temperature is not constant throughout the injection cycle, the cooling time was set at his default value of 10 s, resulting in a cycle time (with the exception of the opening and closing of the mould) of 31.16 s or 30.23 s depending on the used velocity.

7.5 Thermomechanical Indices Methodology

The simulation of the injection moulding process was carried out in Autodesk Moldflow Insight (AMI) 2012. The model was drawn in Solidworks 2014 and the feeding system in AMI. A dual domain mesh was employed in the simulation with 99.7% of match percentage. As previously mentioned, a computer program based on C++ language developed at the Institute of Polymer and Composites was used to calculate the TMI in each element of the mesh along the various stages of the injection moulding process. Following the previously mentioned procedure (3- Thermomechanical Indices) the data obtained from the simulation was stored in several directories for further computation. A rectangular portion of the centre of the disc, containing 398 elements, was chosen for the correlation between the TMI and the regression equations.

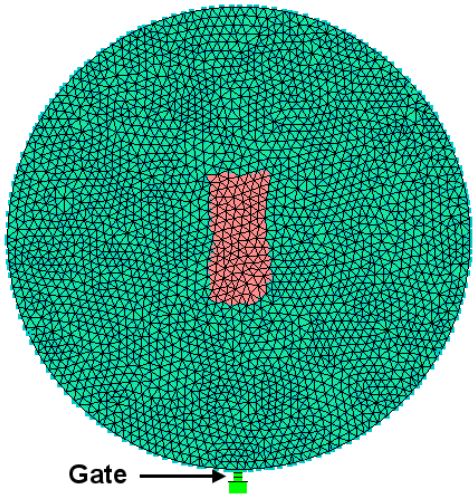

Figure 23: Model mesh with the selected region for the calculation of the TMI

7.6 Morphological Characterisation

7.6.1 PLM

With a DeWalt bandsaw a squared portion (ca. 20x20 mm) from the centre of the disc was cut, Figure 24. Thin films of polypropylene with ca. 20 μm were obtained using a Leitz 1410 microtome equipped with a glass knife. They were submerged in Canada balsam and placed between slid and cover glass to be left to cure for a period of 24h.

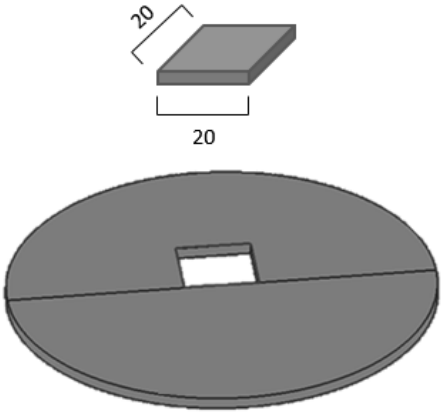

Figure 24: Sample for the skin ratio evaluation

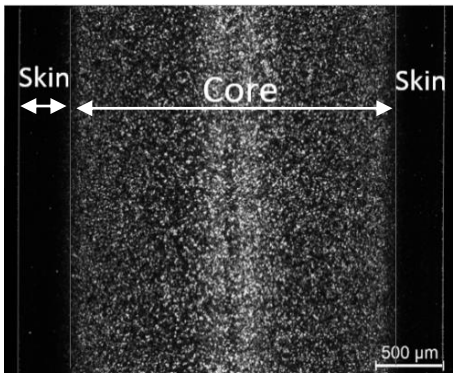

Figure 25: Example of the microstructure observed by PLM

Using an Olympus BH-2 microscope with the software Leica V4.5, the eight different microstructures were observed. In all samples a skin and core region was identifiable (Figure 25). Two samples of each condition were evaluated.

The next step was the assessment of the skin ratio. It was defined as the ratio of a representative skin measurement, given by the average distance between two parallel lines placed along the sample's skin length, and the overall average sample width (assessed by the average value of 5 measurements), equation 39. The distances were obtained using the tools available in Leica's software.

$$Sa = \frac{Representative\ skin\ thickness\ value}{Representative\ width\ value} \tag{39}$$

7.6.2 XRD

One sample obtained from the centre of each disc was skived with sandpaper in order to obtain a predetermined skin thickness. Lower grain size (120-1000) paper was employed to remove the majority

of the material, following finer sized ones (2400-4000) to give a smooth finish. Afterwards, diamond paste of 0.25 μm was used to lightly polish the surface of each specimen. A schematic representation of this procedure is illustrated in Figure 26.

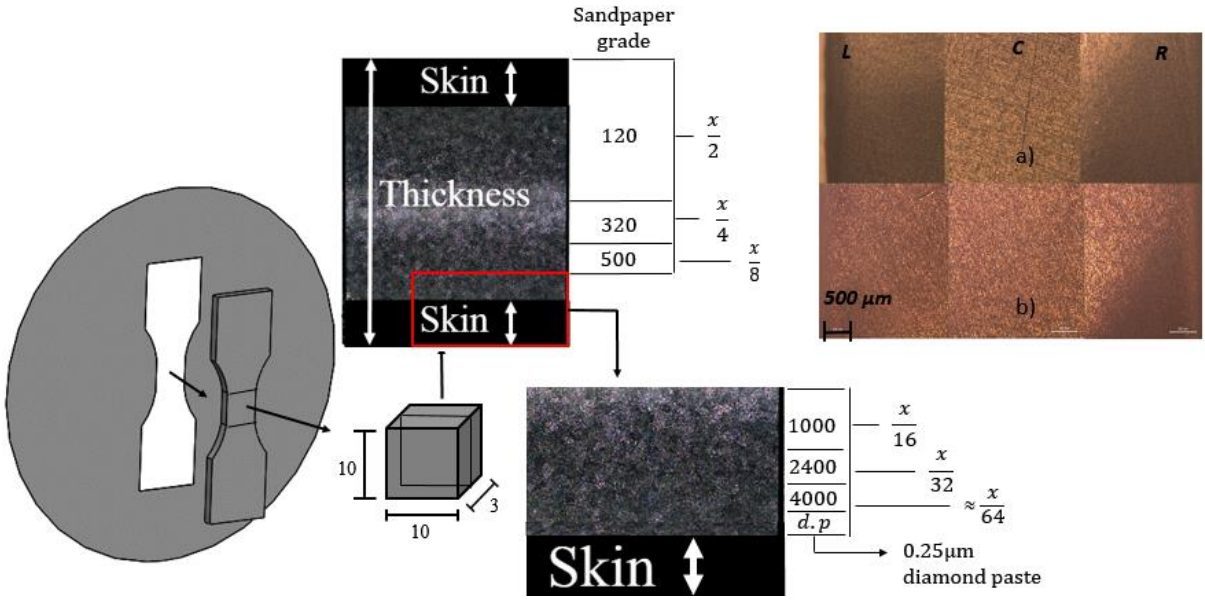

Figure 26: Schematic representation of the procedure used to obtain the skin samples: a) represents the sample before using the diamond paste and b) after using the diamond paste.

The Emyrean x-ray diffractometer from PANalytical containing Cu-Kα radiation with a wavelength of 1.54 Å and a linear detector (1D) were employed. The scans were performed from 10 to 30° with a step size of 0.04°. The molecular orientation (Ωs), the index of crystallinity and the β-phase content of the skin layer were assessed with a Bragg-Brentano reflection setup.

The orientation was calculated by using the average value between the two indices derived by Zipper et al. [73] (A_{110} and A_{130}), equation 40. The skin crystallinity by equation 15 and the β-phase content by equation 16.

$$\Omega s = \frac{A_{110} + A_{130}}{2} \tag{40}$$

The deconvolution procedure was performed in Peak Fit v4.12 where a Gaussian smooth and a background correction were applied to all XRD spectrums. The fitting procedure was performed using a Gaussian + Lorenz curve.

Also, to evaluate the beam penetration on the polymeric samples a study was carried out. X-rays are attenuated as they pass through matter, i.e., the intensity of an X-ray beam decays exponentially the farther it penetrates into matter. This decrease is dependent upon two factors: i) the thickness of the

sample and; ii) the capability of the material to absorb radiation (absorption coefficient). The Beer-Lambert law, equation 41, can be used to describe this phenomena.

$$\frac{I}{I_0} = e^{(-\mu t)} = e^{-MAC\rho t} \tag{41}$$

Where I_0 is the incident intensity, μ the linear absorption coefficient, t the sample thickness (depth of penetration) and MAC is the mass absorption coefficient.

If we consider that the depth of penetration of the x-ray is dependent upon the incidence angle (θ) we can calculating the attenuation length, which is defined as the depth into the material where the intensity of the X-rays has decreased to about $^1/_e$ (37%) by applying equation 42 [89].

$$\ln\left(\frac{1}{e}\right) = \left(-\frac{\mu t}{\sin\theta}\right) \tag{42}$$

A plot of the attenuation length vs incident angle was obtained in [90], Figure 27. At 14.1° the attenuation length as a value of nearly 0.7 mm. Similar penetration values have been reported in [91].

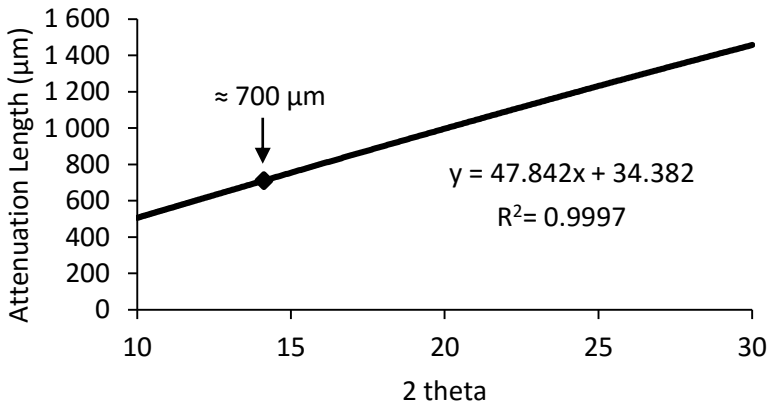

Figure 27: Attenuation length vs 2θ

As an attempt to confirm the previous calculation, the thickest sample evaluated (0.42 mm), corresponding to experiment E1, was placed on top of an oriented silicon sample holder. Silicon has two well-defined peaks around 47 and 56° respectively, whereas PP does not have any diffraction peaks in this region. In Figure 28 it is possible to identify the previously mentioned peaks. This may indicate that at least at 47° the x-ray beam has the capability to penetrate the bulk of the sample.

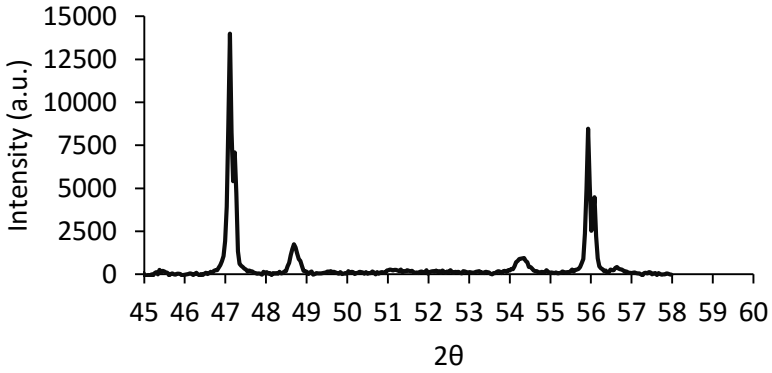

Figure 28: Diffraction plot of a PP sample from 45 to 58°

7.6.3 DSC

For the DSC analysis, 3 discs from each condition were evaluated. Using a 2 millimetre hollow punch, a portion from the centre of each disc with an average weight of 8.917g ± 0.4g was pressed inside Perkin-Elmer aluminium pans. The tests was performed in a Perkin-Elmer DSC-7 from 30 to 200 °C at 10°C/min, the apparatus had been previously calibrated with Indium. To eliminate the background effect, a test was performed without any capsules in order to do a baseline correction. For the calculation of the degree of crystallinity, the enthalpy of fusion value was obtained from the area bellow the DSC curve from 120-180°C and value of the equilibrium enthalpy of fusion (148 J/g) from [92].

7.7 Tensile tests

7.7.1 Quasi-Static

For the quasi-static tensile tests nine specimens of each processing condition were evaluated, resulting in a total of 72 tests. These were conducted in an Instron 4505 tensile machine with a constant cross-head velocity of 20mm/min ($3.33 \times 10^{-4} ms^{-1}$), resulting in a nominal strain-rate of $1.11 \times 10^{-2} s^{-1}$, at 23°C and 50% relative humidity. The tensile specimen was manufactured according to a modified version ISO 8256- type 3 and prepared by a cutting operation from the lateral gated discs as depicted in Figure 29. Further information about the design of the specimen is presented in the next section. (7.7.2- High Speed Tensile Tests).

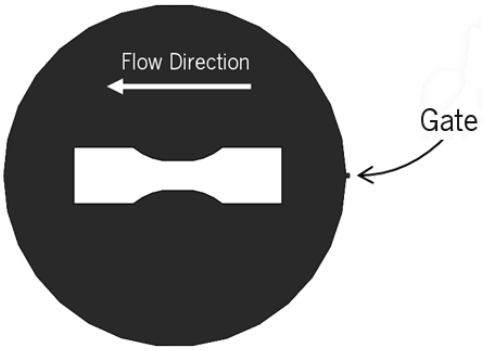

Figure 29: Schematic representation of the test specimens cutting operation

After testing all the specimens a representative homogenous curve was taken for the calculation of the true stress- strain curve. A Samsung HMX- H300BP with a recording capability of 50 frames per second and a resolution of 1280 x 720 pixies was mounted on a tripod and set to record each test. A mirror was placed at approximately 45° in order to observe the variation of the thickness of the specimens. The setup is depicted in Figure 30.

For the construction of the true stress-strain curves, the change in the area of the specimen must be accounted for. Using Image Pro Plus v6, 19 equally spaced frames of each test were evaluated. In each one the change of the cross-section in the thinnest region of the gauge length was calculated. A correction of the area was set by fitting a regression equation in an area vs time plot. An example regarding the construction of the true stress- strain curves for experiment E2 will be given bellow:

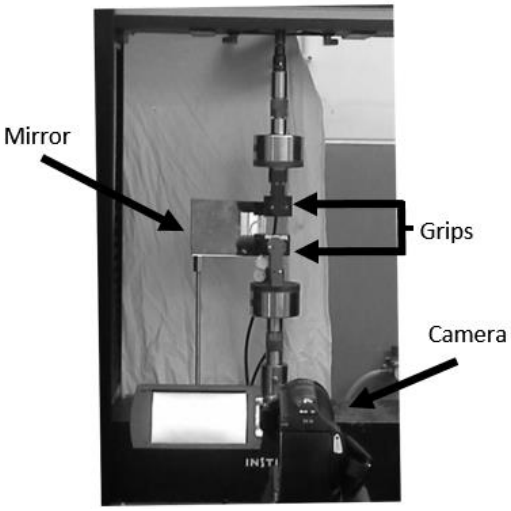

Figure 30: Setup for the quasi-static tensile tests

This tensile test has 2180 points and the tensile apparatus was set with a data collection rate of 30 points/sec. The recording time from the camera is 50 fps, meaning that between the two equipment

there is a data ratio of approximately 1.67 times. Multiplying the number of points from the test with the data ratio we obtain the number of frames representing the test, which in this case is 3633. Afterwards, the number of the last frame representing the test, frame right before fracture (Figures 31 and 32), must be reported. In this case it is the frame 3941.

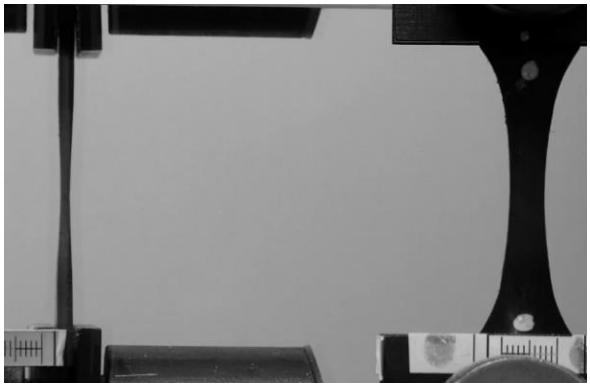

Figure 31: Frame 3941 (before fracture)

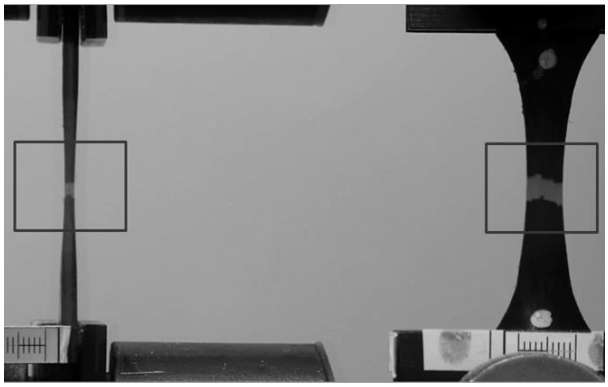

Figure 32: Frame 3942 (after fracture)

So, if the last frame has the number 3941, the first frame must be 3941 – 3633 (total number of frames in the test) which is equal to 308 (number of the first frame). After knowing the first and last frame, the test was segmented. The measurements are reported in Table 10.

The next step involves the correlation of the variation of area (ΔA) in relation to time. Since the cross section of the specimen is a rectangle, the area is simply the product of width x thickness. The time was calculated using the following equation:

$$time\ (s) = \frac{(F_x - F_0)}{frame\ rate} \tag{43}$$

Where F_x is the number of a determinate frame, F_0 is the first frame of the test and the frame rate the number of pictures taken per time period (in this case, seconds).

The plot of ΔA vs time is depicted in Figure 33. A second order polynomial regression equation was employed using Microsoft Excel because it provided the best regression coefficient. After determining the trend of the area in regard to time, a fitting was done to match the first area value. Figure 35 illustrates the variation of the specimen area along the tensile test (the engineering curve was modified assuming the Hencky strain in order to compare both curves).

Table 10: Measurements of the width and thickness variation in experiment E2

Frame number	Width (mm)	Thickness (mm)
308	9.568	3.092
499	9.471	3.092
690	9.375	2.982
882	9.278	2.982
1073	9.085	2.871
1264	8.988	2.871
1455	8.795	2.761
1647	8.698	2.650
1838	8.408	2.650
2029	8.312	2.650
2220	8.118	2.429
2412	7.828	2.429
2603	7.635	2.319
2794	7.442	2.319
2985	7.248	2.209
3176	7.152	2.098
3368	6.959	2.098
3559	6.765	1.988
3750	6.572	1.988
3941	6.282	1.877

In all quasi-static curves the initial modulus was taken without an extensometer from the homogeneous curve as the slope between 0.4 and 0.8%, Figure 34. The use of an extensometer would have compromised the video recording of the tests so the modulus was calculated using the displacement provided by the tensile machine. The strain at break in all tested velocities was defined as the strain value where the stress decreases to $0.85\sigma_M$ in the homogeneous curve.

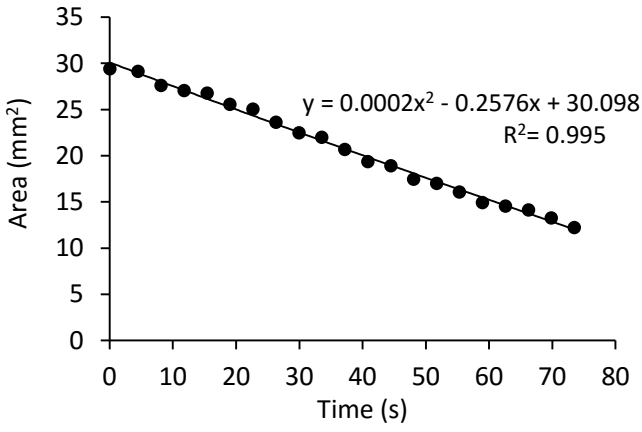

Figure 33: Correlation between area and time

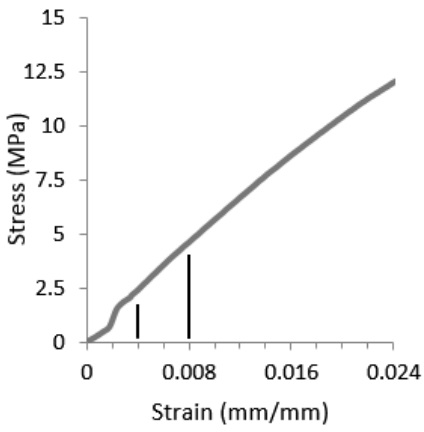

Figure 34: Initial portion of the representative curve of experiment E2

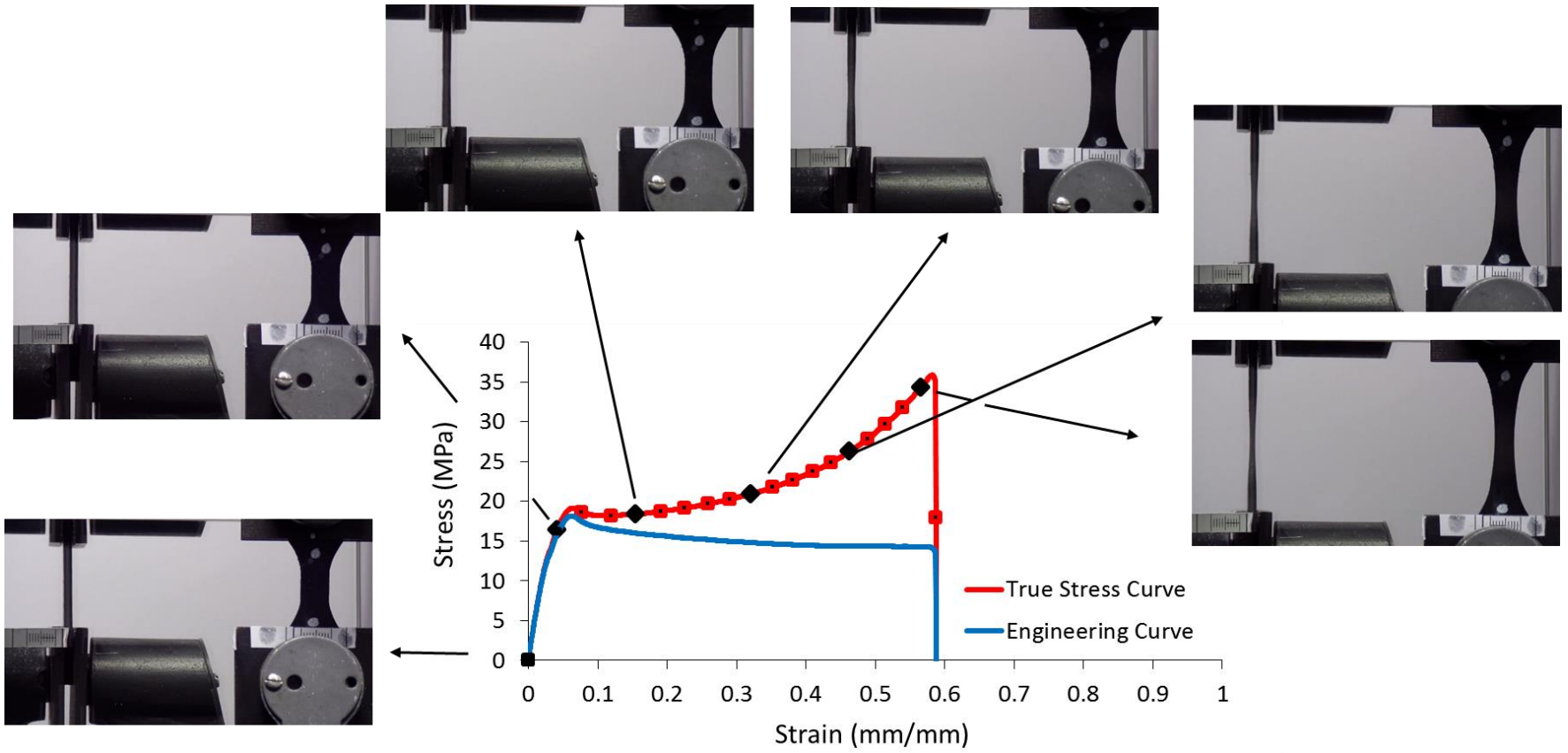

Figure 35: Deformation of the specimen during the tensile test at 20mm/min

7.7.2 High Speed

The high speed tensile tests were performed in a Zwick-Roell Amsler HTM3712 tensile machine at 1 (33.33 s^{-1}) and 3 m/s (100 s^{-1}). The apparatus has the capability of performing tests at a maximum velocity of 12 m/s and 20 kN of maximum load.

The specimen selected for high speed tensile tests was the ISO 8256 type 3 which has already been used for dynamic tensile tests [25]. However it was modified to ensure a proper fitting on the gripping system, Figure 36. The modifications were:

- An increment in the grip section width of the specimen from 15 mm to 19 mm;
- Reduction of the overall length from 80 mm to 70 mm to ensure the fixture of the entire grip section.

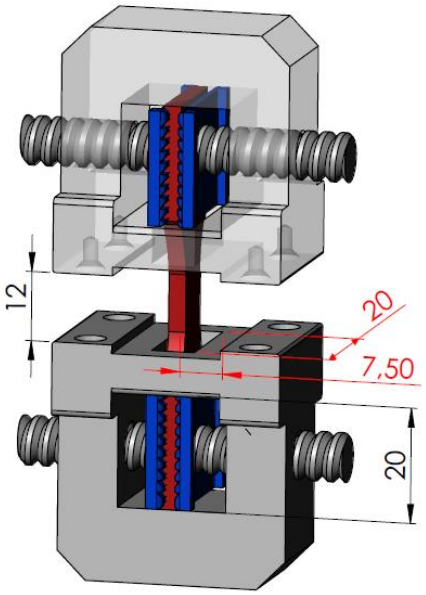

Figure 36: Grip system

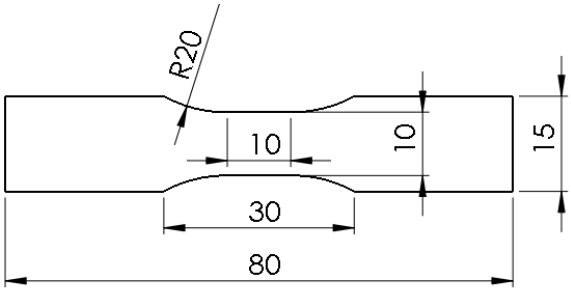

Figure 37: ISO 8256 type 3

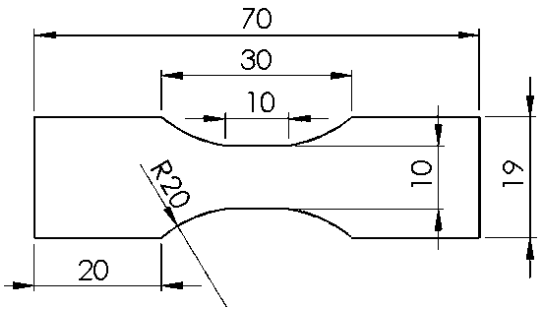

Figure 38: ISO 8256 type 3 modified

The strain calculation was done according to the previously mentioned paper. The author calculated this parameter using the following equation:

$$\varepsilon = \frac{\Delta l}{l_e} \tag{44}$$

Where Δl is the displacement and l_e the clamping length, which in this case is 30mm.

An average of 6 tests were recorded using a Photron AP XRS and 3 with a Photron Mini UX100. With the first camera a resolution of 512 x 384 pixies and a frame rate of 12000 frames per second (fps) was select, and with the latter a resolution of 1280 x 480 and 10000 fps. The criteria for the selection of the resolution was based on the height of the window, which had to allow the visualisation of all the gauge length during the test. Regarding the illumination, two 1000W halogen lamps were implemented and for the background a sheet of cardboard was employed. The recording setup was the same for both cameras and is depicted in Figure 39.

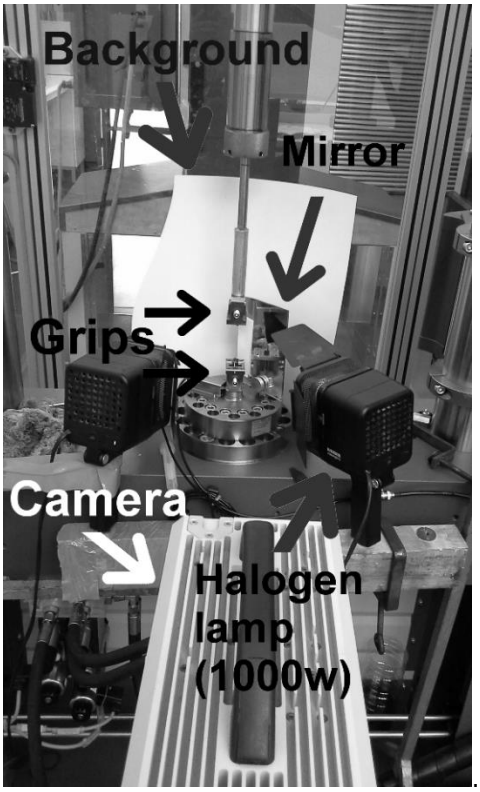

Figure 39: Setup for high speed tensile tests

The force vs displacement curves were treated in order to produce true stress- strain curves in a similar way as the ones in section 7.7.1. For these tests an average of 14 representative frames were

selected and, in accordance with what was done in the previous section an example of how the tensile data was treated will be presented below, taking once again a test from experiment E2 as an example:

The tensile test performed at 1 m/s has 4053 points and the tensile machine at this velocity a data collection rate of 200 points/ms. The representative curve of this condition was recorded using a Photron Mini UX 100 which takes 10 frames per millisecond, representing a data ratio of 0.05, meaning that one frame corresponds to 20 points in the tensile test. Analogously to what was done in the quasi-static tests, the last frame corresponding to the test is the one right before the complete fracture of the specimen, which in this case is the 217 (Figures 40 and 41).

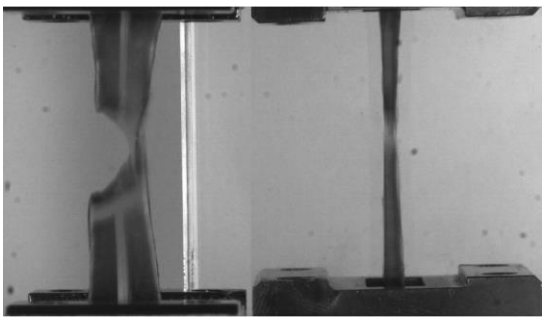

Figure 40: Frame 217 of experiment E2 at 1m/s

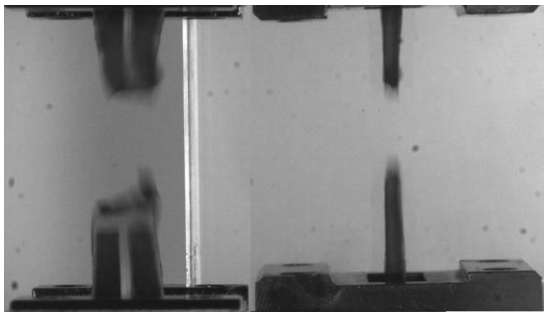

Figure 41: Frame 218 of experiment E2 at 1m/s

For the high speed tests, the first frame was selected as the one right before movement of the grip is detected. Lastly, the test was divided into 14 parts and the variations in the width and thickness of the specimens measured, Table 11.

The plot of ΔA vs time is illustrated in Figure 42. A second order polynomial regression equation was employed, however because of the type of rupture of the specimen, the regression coefficient was not very satisfying. To face this problem the last frames of the test were measured in order to see if an adjustment in the polynomial trend was need, Figure 45.

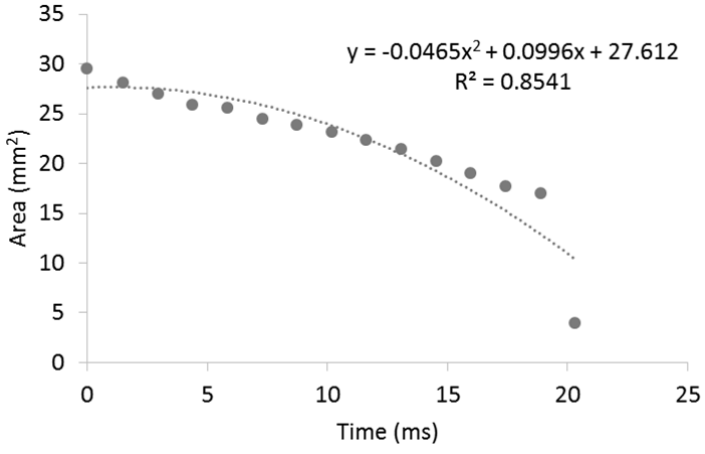

Figure 42: Variation of the area for experiment E2 at 1m/s

Table 11: Variation of the width and thickness for experiment E2 at 1 m/s

Frame	Width (mm)	Thickness (mm)	Time (ms)
14	9.568	3.092	0.000
29	9.402	2.995	1.493
43	9.318	2.899	2.940
58	9.235	2.802	4.387
72	9.152	2.802	5.833
87	9.069	2.706	7.280
101	8.819	2.706	8.727
116	8.570	2.706	10.173
130	8.570	2.609	11.620
145	8.237	2.609	13.067
159	8.070	2.512	14.513
174	7.904	2.416	15.960
188	7.654	2.319	17.407
203	7.322	2.319	18.853
217	2.080	1.933	20.300

Adding more point did not improve significantly the R^2 so, as an alternative, maybe adding a higher order polynomial equation would provide a better fitting. Figure 43 shows a third order polynomial available when using Microsoft Excel. Even though the R^2 improved, it is still unsatisfactory due to large deviation of the predicted area in relation to the measured one at the near end of the curve. To solve this problem, the last 6 point of the curve were removed. Figure 44 shows the final result and, as expected, the R^2 improved considerably. The removed points represent frames 212 to 217 which represent 0.6 ms or 120 data points.

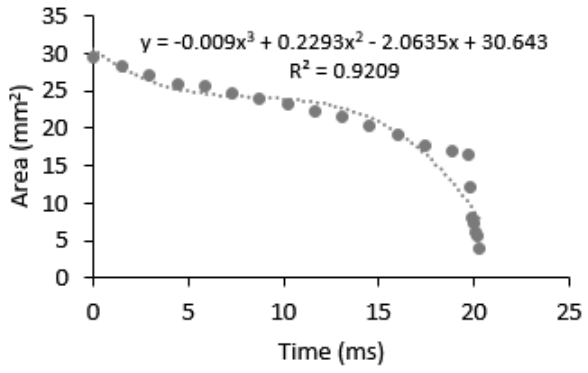

Figure 43: Area fitting using a 3rd order polynomial equation

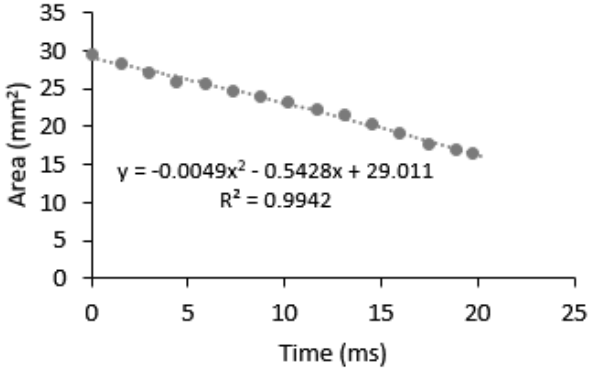

Figure 44: Final area fitting for experiment E2

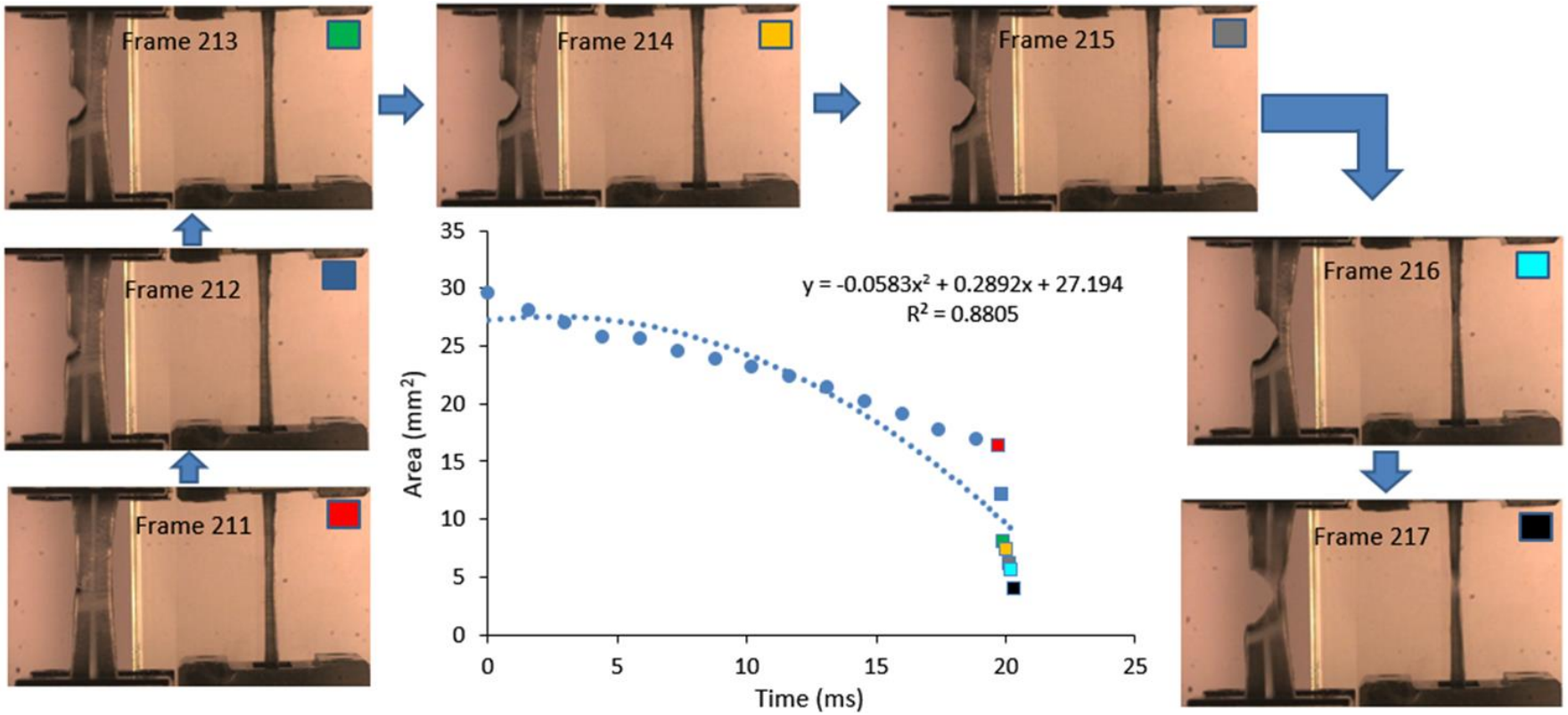

Figure 45: Sequence representing the fracture of the specimen (experiment E2) in a high speed tensile test

Figure 46 shows the true stress-strain plot for experiment E2 with and without the last 120 points. This type correction was performed to all the curves who showed this type of fracture, namely experiments E2 and E3 for the tensile tests at 1m/s and E1, E3, E4 and E8 for 3 m/s. Figures 49 and 50 represent the true stress tensile curves obtained for experiment E2 at 1m/s and 3m/s comparing them to their respective engineering curves. Analogously to the procedure done in the quasi-static curves, the strain used in both true and engineering curves is the Hencky strain.

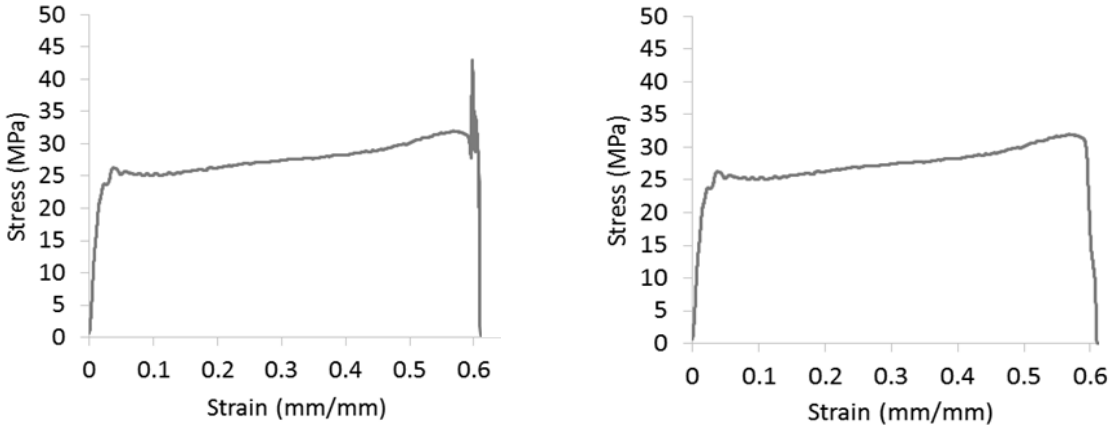

Figure 46:Tensile curves illustrating the correction done to the data: a) before correction; b) after correction

Due to acceleration effects, the σ –ε curves initially exhibit a parabolic effect with increasing strain-rate. The initial modulus was taken from the slope of the homogeneous curve from 0.4- 0.7% at 1 m/s and from 0.8-1.16 % at 3 m/s. Due to the nature of these tests no contact extensometer was used.

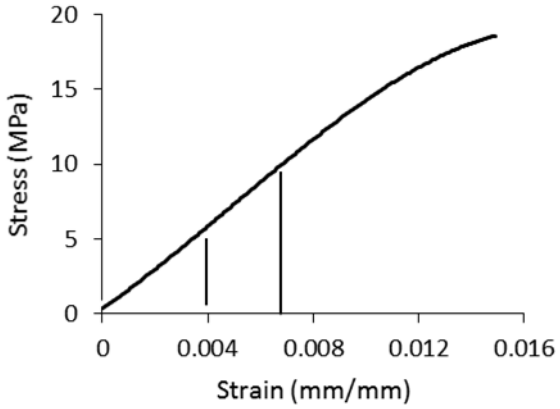

Figure 47: Initial part of the homogenous curve at 1m/s

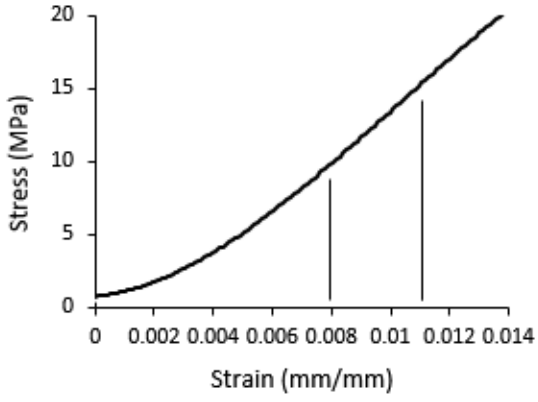

Figure 48: Initial part of the homogenous curve at 3m/s

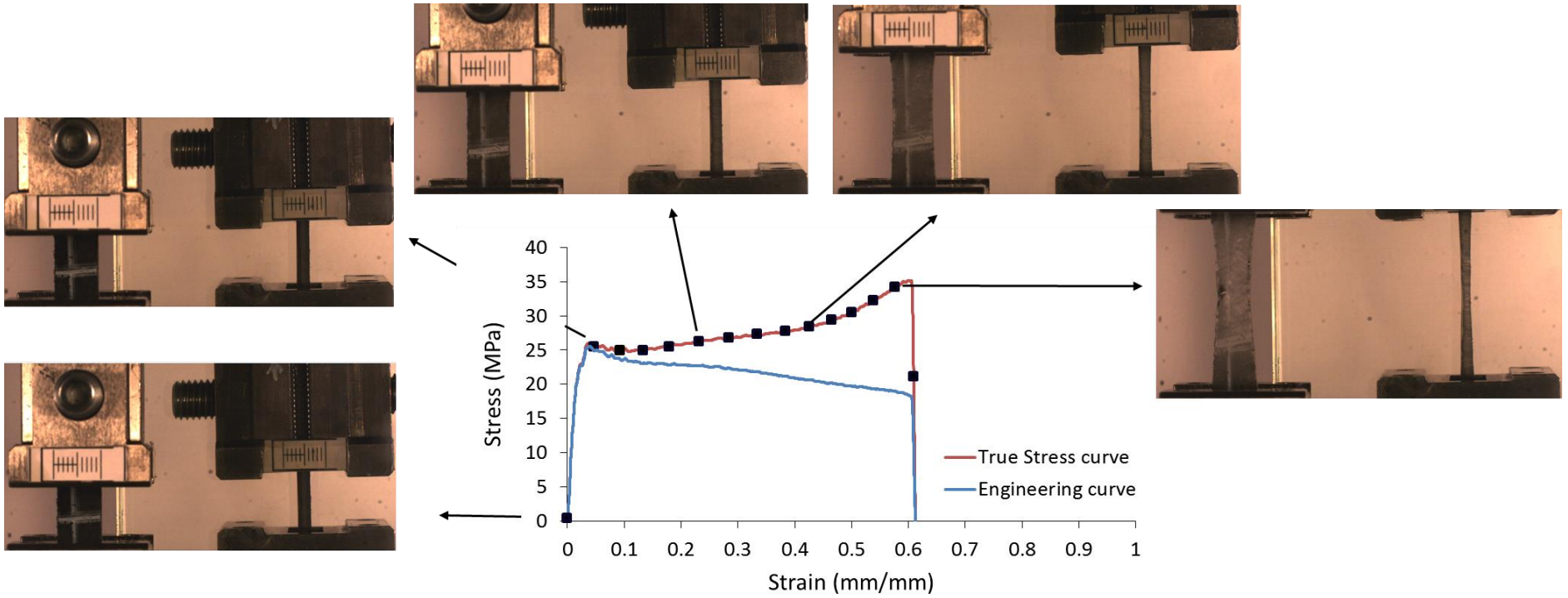

Figure 49: Comparison between the true stress curve and the engineering tensile curve at 1m/s

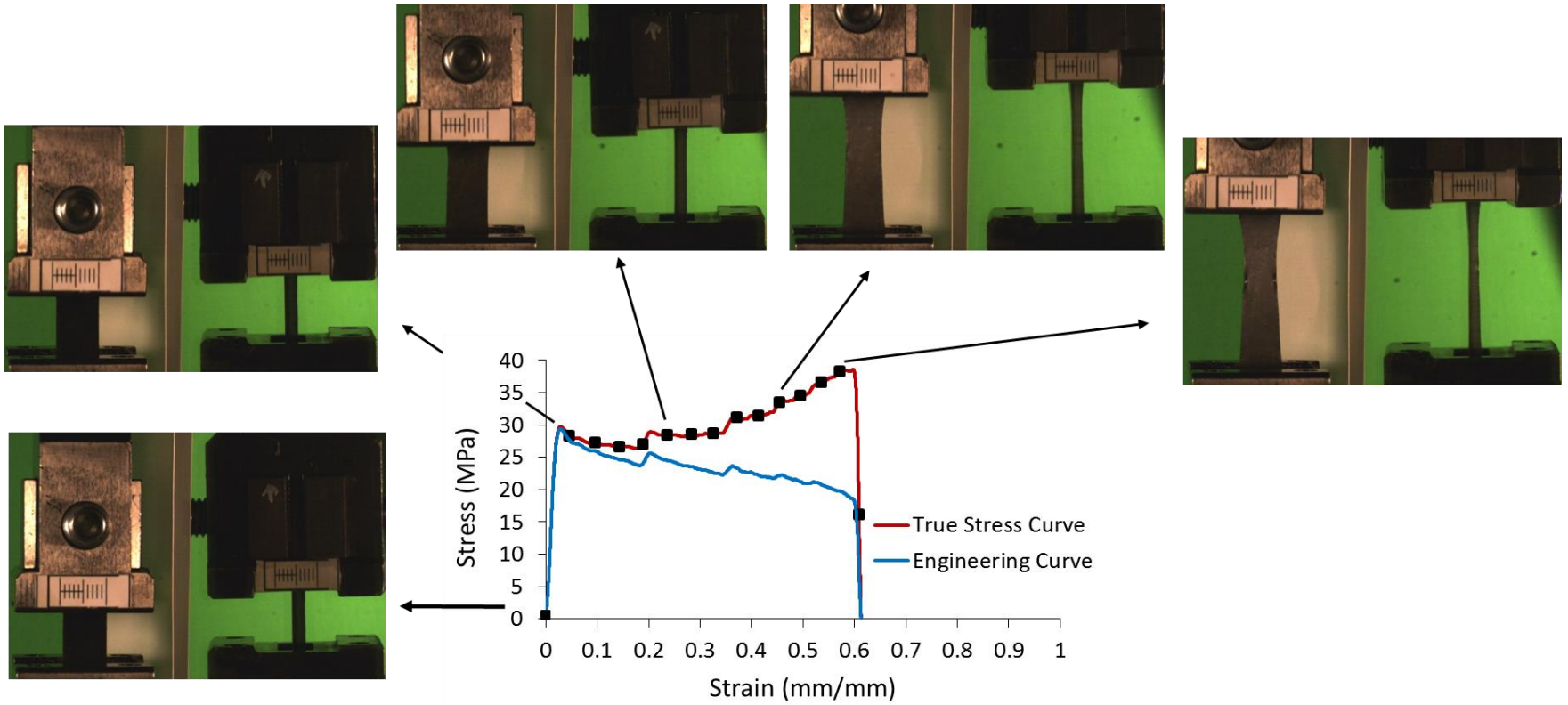

Figure 50: Comparison between the true stress curve and the engineering tensile curve at 3m/s

8. RESULTS AND DISCUSSION

8.1 Thermomechanical Indices

The thermomechanical indices were calculated through several simulations of the IM process using AMI. As previously mentioned, these TMI were calculated from the central part of the disc containing nearly 400 elements. The results are presented in Table 12.

Table 12: Results of the thermomechanical indices

	Filling		Packing (weighted)		Cooling (weighted)	
Condition	Y	τ_Y	Y	τ_Y	Y	τ_Y
E1	0.430	43815	0.061	25738	0.105	19975
E2	0.442	62677	0.052	21813	0.105	16128
E3	0.571	27631	0.100	16958	0.135	14194
E4	0.582	35809	0.023	15826	0.065	13770
E5	0.628	36596	0.178	15982	0.211	12325
E6	0.640	50369	0.031	14648	0.059	12156
E7	0.755	20424	0.123	11238	0.154	6022
E8	0.763	29785	0.028	12840	0.044	5928
Δ	77 %	207 %	681 %	129 %	382 %	237 %

A significant variation (Δ), equation 45, is observed within the DOE plan.

$$\Delta = \frac{(Prop.max - Prop.min)}{Prop.min} \tag{45}$$

The cooling index characterises the thermal level of the moulding and aims to quantifying the crystallinity level, and, the thermal-stress index the level of molecular orientation. For the filling stage, the analysis of variance indicated the influence of the injection (33%) and mould temperature (67%) on the CI and the injection velocity (25%), injection (62%) and mould temperatures (10%) on the TSI. Figure 51 illustrates the normalised effect of the processing conditions on the TMIs. The normalization was done by dividing each value by the respective maximum within each index.

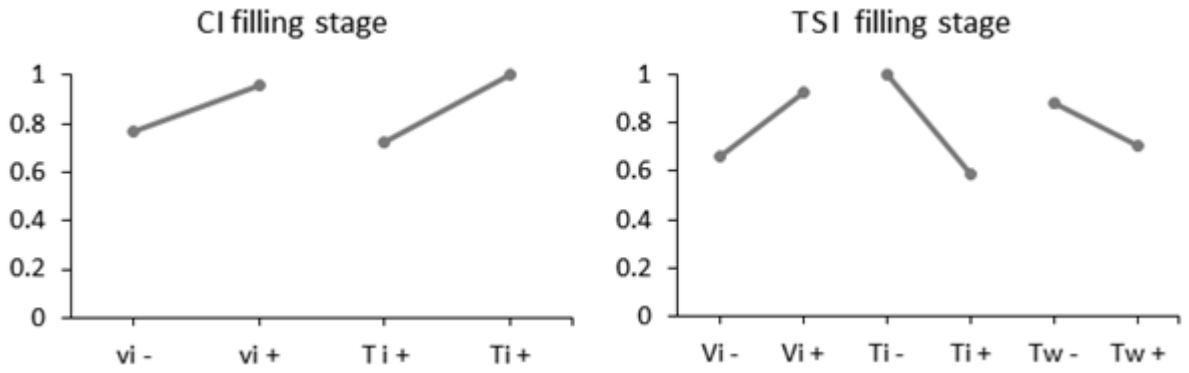

Figure 51: Effect of the processing conditions on the TMI at the end of filling

A summary of the ANOVA regarding the processing conditions vs TMI is presented in Table 13. The cooling index at the end of both packing and cooling stages seems to be affected by the injection velocity and holding pressure. The effect of v_i was detected in the CI for both weighted packing and cooling phases with a contribution of 63%. Since v_i does not appear in the filling stage one can assume that the method used to calculate these indices is not the most correct. This is further noticed when plotting the CI for the filling vs packing and packing vs cooling phase. A lack of correlation exists between the cooling index at the end of filling and packing while a good relationship exists for the weighted indices at the packing and cooling stages.

For this reason the TMI beyond the filling stage will not be used to establish relationships with the mechanical and morphological parameters.

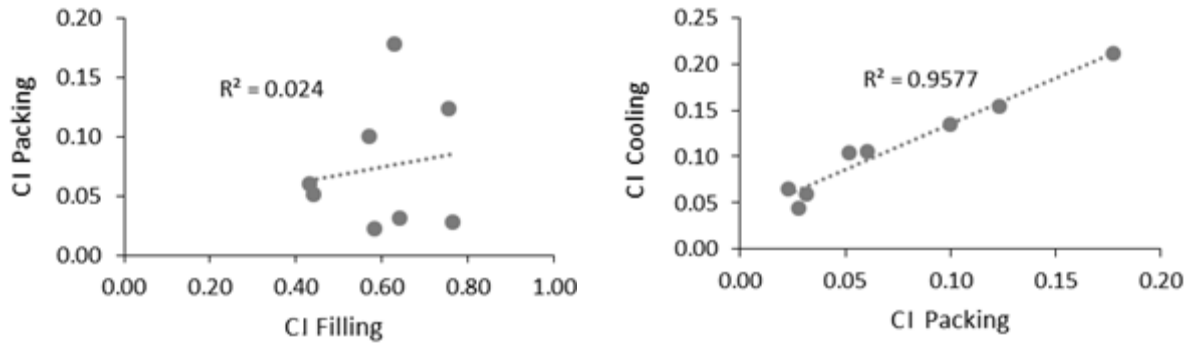

Figure 52: Relationship between the cooling index at different processing stages

Table 13: Effect of the processing conditions on the thermomechanical indices

	Model terms	End of Filling	End of Packing	End of Cooling
Cooling Index	Linear	▲B ▲C	▼A ▲C ▲D	▼A ▲D
	Interactions		AC	AC
	R^2	0.997	0.957	0.915
	R^2 Adj	0.996	0.900	0.851
	R^2 Pred	0.992	0.700	0.660
Thermo-Stress Index	Linear	▲A ▼B ▼C	▼B ▼C	▼B ▼C
	Interactions			
	R^2	0.969	0.880	0.938
	R^2 Adj	0.945	0.832	0.913
	R^2 Pred	0.875	0.693	0.840

8.2 Morphological Characterisation

8.2.1 Skin Ratio

The skin ratio was evaluated by PLM. The results of Sa as a function of the processing conditions are illustrated in Figure 53. From the obtained results it is possible to observe that experiment E1 (▼v_i, ▼T_i, ▼T_w, ▼P_h) and E8 (▲v_i, ▲T_i, ▲T_w, ▲P_h) represent the highest (red colour) and lowest (blue colour) Sa, respectively. This type of colour representation is presented in all the graphs below. Figures 54 and 55 depict the micrographs of these conditions, the remaining being present in Annex IV – PLM images.

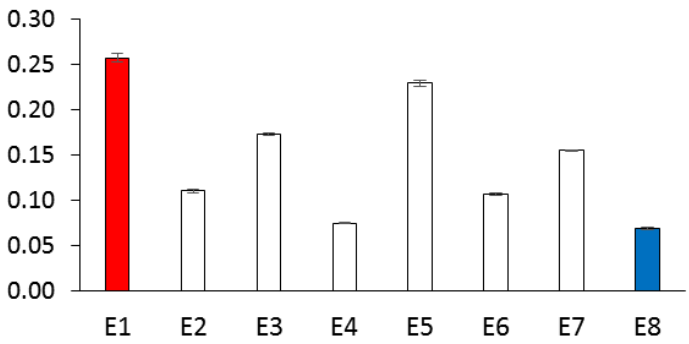

Figure 53: Variation of Sa with each processing condition

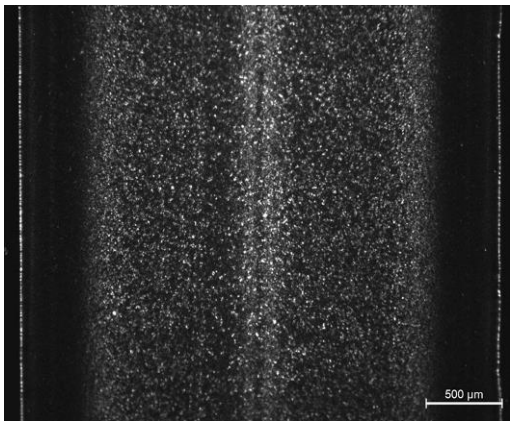

Figure 54: Microstructure of E1

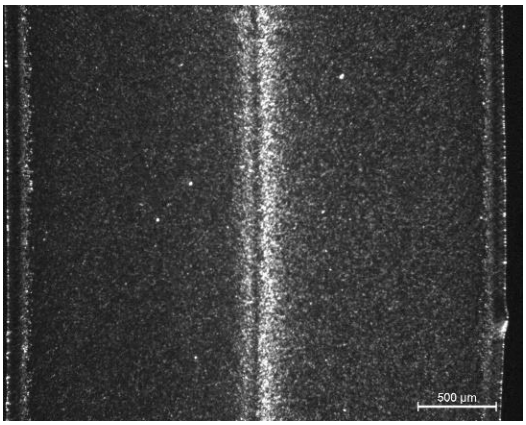

Figure 55: Microstructure of E8

The ANOVA results, Table 14, indicate that the most relevant factors influencing this parameter are the injection velocity with a contribution of nearly 76% and the melt temperature with 20%. The model presents a coefficient of determination (R^2) equal to 0.9569 for a degree of confidence (α) of 99%. The model F-Value indicates a value of 55.56, presenting itself significant with a 0.04 % chance that this value has occurred due to noise.

The dependency of the skin ratio with v_i and T_i is presented in Figure 56.

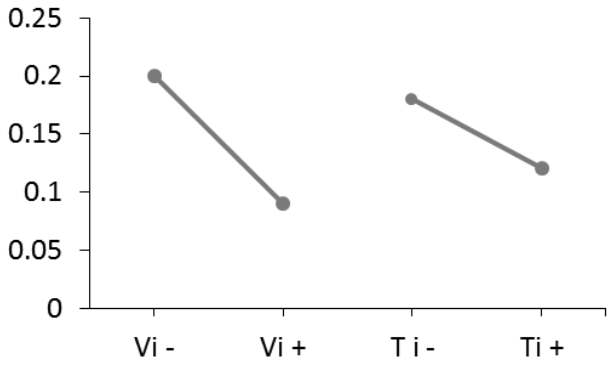

Figure 56: Effect of the processing conditions on the skin ratio

In this case Sa is maximised for the minimum values of v_i and T_i. In the injection moulding process the material at the flow front rapidly solidifies due to the existence of a high temperature gradient. In this case a lower injection speed allows the molten polymer to experience a longer shearing time during the filling stage allowing the melt to be cooled more effectively during the filling stage. The effect of these processing variables goes in accordance to what was found in the literature [3], [4], [6].

Table 14: ANOVA of Sa

	Sum Of Squares	d.f	Mean Square	F-Value	Prob> F	Contribution
Model	0.032	2	0.016	55.56	0.0004	
A-Injection Velocity	0.026	1	0.026	87.98	0.0002	75.76%
B-Injection Temperature	6.748×10^{-3}	1	6.748×10^{-3}	23.15	0.0048	19.93%
Residual	1.458×10^{-3}	5	2.915×10^{-4}			4.31%
Total	0.035	7				100%
	R^2 adj	0.9397		R^2 pred	0.8898	

8.2.2 Skin orientation and crystallinity index

The skin orientation (Ωs) and crystallinity index (χ_{skin}) were evaluated through a WAXS analysis. Ωs was obtain by calculating the average value between 2 orientation indices derived by Peter Zipper, A_{110} and A_{130}, equation 40. χ_{skin} was assessed by equation 15. Figure 57 illustrates the variation of both parameters as a function of the processing conditions. Experiment E7 ($\blacktriangledown v_i$, $\blacktriangle T_i$, $\blacktriangle T_w$, $\blacktriangledown P_h$) presents the lowest value of orientation and skin crystallinity level, whereas experiment E6 ($\blacktriangle v_i$, $\blacktriangledown T_i$, $\blacktriangle T_w$, $\blacktriangledown P_h$) and E2 ($\blacktriangle v_i$, $\blacktriangledown T_i$, $\blacktriangledown T_w$, $\blacktriangle P_h$) the highest value of Ωs and χ_{skin}, respectively.

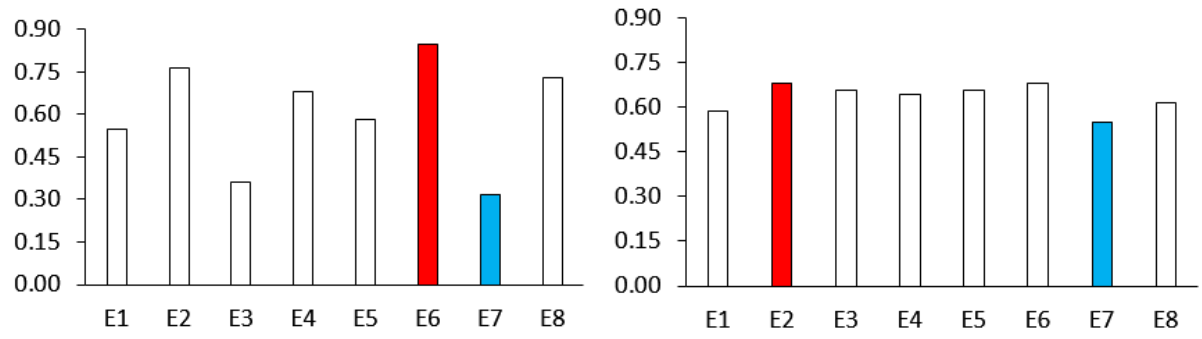

Figure 57: Variation of the skin orientation (a) and crystallinity index (b) with each processing condition

The analysis of variance, Table 15, for the skin orientation (R^2= 0.94, α=0.1) indicated a significant model F-value of 42.23 with 0.07% of probability that this value occurred due to noise. The most significant factors for the variation of skin orientation are the injection velocity (73%) and temperature (22%). For χ_{skin} (R^2= 0.99, α=0.1) a model F-value of 225.12 with 5.1% of chance that this value occurred due to noise. All main factors are significant parameters, even though some present a far lower contribution than others.

Table 15: ANOVA of Ωs and χ_{skin}

		Sum Of Squares	d.f	Mean Square	F-Value	Prob> F	Contribution
Skin Orientation	Model	0.24	2	0.12	42.23	0.0007	
	A-Injection Velocity	0.18	1	0.18	65.22	0.0005	72.89 %
	B-Injection Temperature	0.054	1	0.054	19.25	0.0071	21.50 %
	Residual	0.14	5	2.797×10^{-3}			5.61 %
	Total	0.25	7				100 %
	R^2 adj	0.9218		R^2 pred	0.8569		
Skin Crystallinity Index		Sum of Squares	d.f	Mean- Square	F-Value	Prob> F	Contribution
	Model	0.015	6	2.525×10^{-3}	225.12	0.0510	
	A-Injection Velocity	3.595×10^{-3}	1	3.595×10^{-3}	320.54	0.0355	23.71 %
	B-Injection Temperature	2.357×10^{-3}	1	2.357×10^{-3}	210.15	0.0438	15.55 %
	C-Mould Temperature	6.429×10^{-4}	1	6.429×10^{-4}	57.33	0.0836	4.24 %
	D-Hold Pressure	2.802×10^{-3}	1	2.802×10^{-3}	249.83	0.0402	18.48 %
	AB	5.950×10^{-4}	1	5.950×10^{-4}	53.06	0.0869	3.93 %
	AD	5.156×10^{-3}	1	5.156×10^{-3}	459.80	0.0297	34.02 %
	Residual	1.121×10^{-5}		1.121×10^{-5}			0.07 %
	Total	0.015	7				100 %
	R^2 adj	0.9948		R^2 pred	0.9527		

In accordance to what was found in literature the skin orientation seems to increase for a higher value of v_i and lower T_i, as depicted in Figure 58. A higher shear stress aligns the polymer macromolecules along the flow direction which coupled with a higher degree of undercooling makes the bulk temperature reach the crystallization temperature in a shorter time, minimizing relaxation effects and maintaining the molecules align in the flow direction. According to the ANOVA of χ_{skin}, the injection velocity presents the highest contribution of all the main factors. Even though it indicates that χ_{skin} increases when applying lower temperatures, it was found that shearing strongly increases the nucleation density and growth rate during crystallization which may explain why the skin layer has a higher crystallinity for these conditions [12].

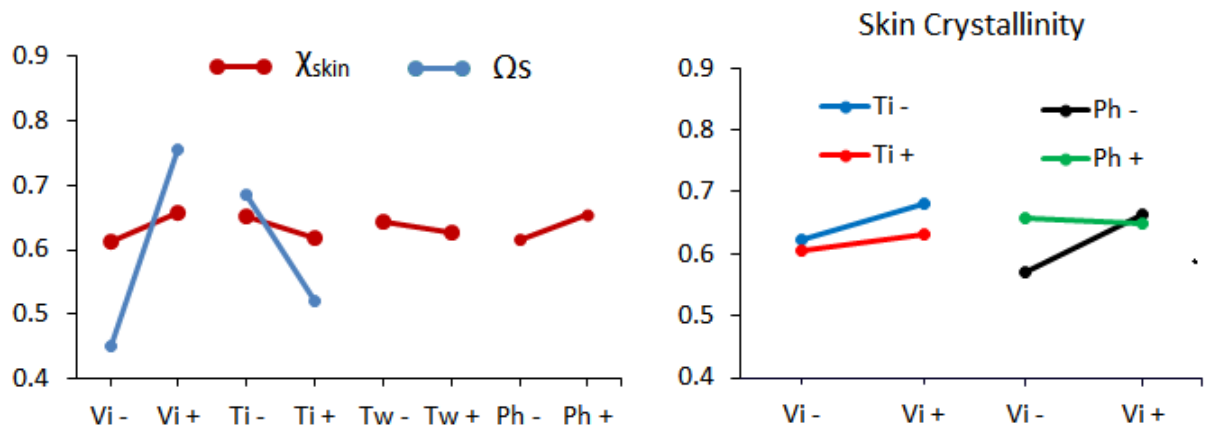

Figure 58: The effect of the processing conditions on the skin orientation and crystallinity

8.2.3 β-phase Content

The β-phase content was evaluated through a WAXS analysis. Figure 59 illustrates the variation of this index as a function of the processing conditions. Experiment E2 (▲v_i, ▼T_i, ▼T_w, ▲P_h) and experiment E7 (▼v_i, ▲T_i, ▲T_w, ▼P_h) present the highest and lowest β-phase content, respectively.

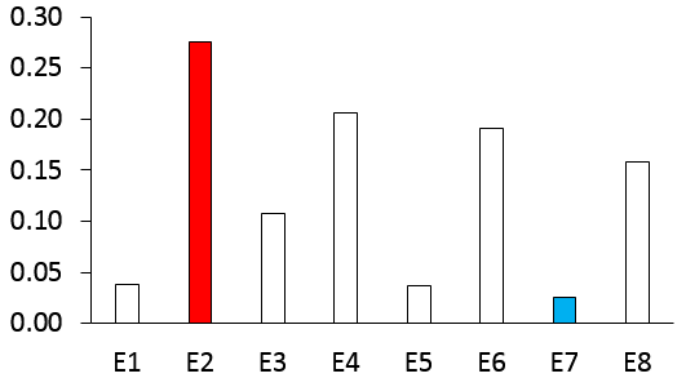

Figure 59: Variation of the β-phase content with each processing condition

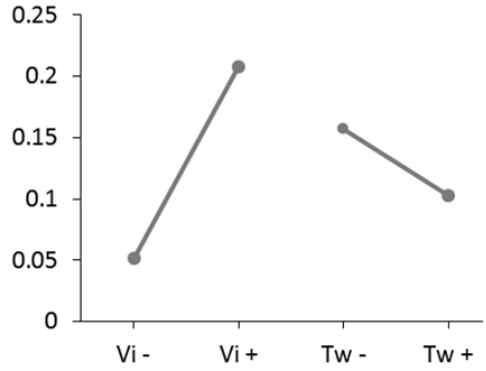

Figure 60: Effect of the processing conditions on the β-phase content

The analysis of variance, Table 16 and Figure 60, (R^2= 0.9062, α=0.1) indicate a significant model F-value of 24.16 with 0.27% of probability that this value has occurred due to noise. The most significant factors are the injection velocity (81%) and mould temperature (10%).

A strong dependency of this parameter with the injection velocity is detected by the analysis of variance. It indicates that an increase in this processing variable induces a higher polymorphism in the mouldings. The mould temperature is also a significant parameter even though with a significant lower contribution, and seemingly with an inverted tendency in regard to what was found in literature. A decrease in this variable leads to a higher β-content. This type of morphological changes seem be

produced in specific shear and temperature conditions leading, according to the literature, to a more expectant ductile behaviour of the material.

Table 16: ANOVA of the β-phase content

	Sum Of Squares	d.f	Mean Square	F-Value	Prob> F	Contribution
Model	0.054	2	0.027	24.16	0.0027	
A-Injection Velocity	0.049	1	0.049	43.13	0.0012	80.89 %
C-Mould Temperature	5.847×10^{-3}	1	5.847×10^{-3}	5.19	0.0717	9.73 %
Residual	5.635×10^{-3}	5	1.127×10^{-3}			9.38 %
Total	0.060	7				100 %
	R^2 adj	0.8687		R^2 pred	0.7599	

8.2.4 Bulk Degree of Crystallinity

The bulk degree of crystallinity was assessed through a DSC analysis. In all 24 tests an average fusion peak of 165.83 °C with a standard deviation of 0.9 °C was reported. The melt enthalpy was calculated from the area below the DSC curve from 120 to 180 °C. The degree of crystallinity was calculated according to equation 17. Figure 61 shows the variation of χ_{Bulk} with each processing condition.

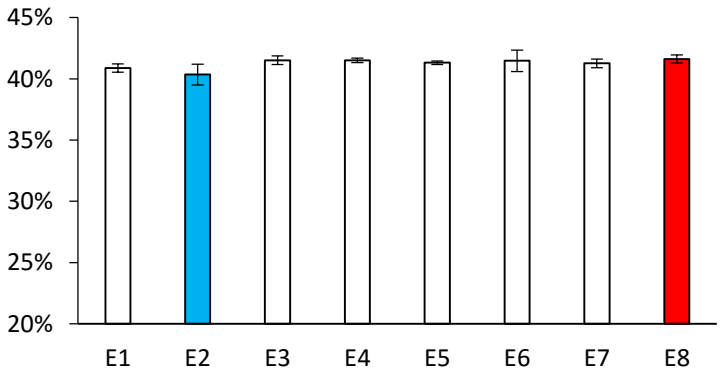

Figure 61: Variation of the bulk degree of crystallinity with the each processing condition

The crystallinity values range from 40.4%, experiment E2 (▲v_i, ▼T_i, ▼T_w, ▲P_h), to 41.6%, experiment E8 (▲v_i, ▲T_i, ▲T_w, ▲P_h) presenting a degree of variation (Δ) of 3.13% with a maximum standard deviation of 0.9%. One can concluded that there is no significant variation within this morphological parameter. A representative DSC curve of each condition is displayed in Figure 62.

Due to lake of significant variation within this parameter no analysis of variance was performed. In the state of the art, Demiray et al. [37] also obtained a rather flat crystallinity profile through the sample thickness of iPP mouldings. Possibly this can be explained by considering that the used processing conditions were not strong enough to slow down the crystallization process of this material.

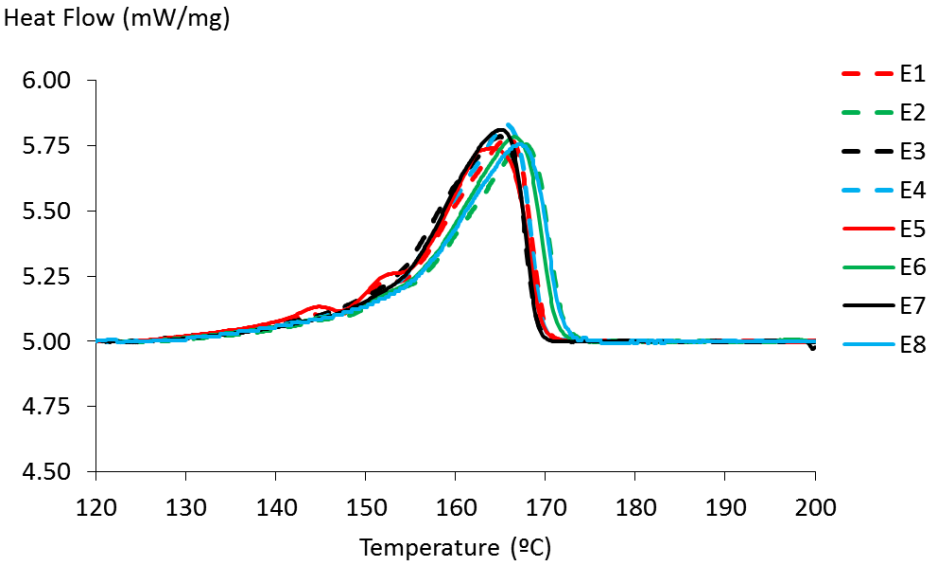

Figure 62: Representative DSC thermogram of each experiment within the DOE

8.3 Mechanical Characterisation

8.3.1 Tensile Properties

In this section the yield stress (σ_y), the initial elastic modulus (E) and strain at break (ε_b) will be addressed. As previously mentioned for the quasi-static tests (1.11 $x10^{-2}s^{-1}$) and high speed tensile (33.33 s^{-1} and 100 s^{-1}) an average of 9 specimens were tested. The five most representative were used to calculate the average value of each property and the results are depicted in Figure 63 and in Table 17.

σ_y in semi-crystalline polymers involves the disruption of the crystalline phase in an irreversible deformation process [21]. Upon this process the spherulitic structure is deformed and transformed into a fibrillar one as deformation increases. Experiment E3 (▼v_i, ▲T_i, ▼T_w, ▲P_h) has the highest value of σ_y for all tested velocities while experiments E5 (▼v_i, ▼T_i, ▲T_w, ▲P_h) and E7 (▼v_i, ▲T_i, ▲T_w, ▼P_h) are the conditions with the lowest σ_y for quasi-static and high speed velocities, respectively. A less regular scenario occurs for the strain at break and the initial modulus. Regarding the modulus, experiments E7,

E2 and E4 (▲v_i, ▲T_i, ▼T_w, ▼P_h) present the highest values of modulus and experiments E2, E1 and E5 the ones with the lowest value of this parameter. Experiments E1 (▼v_i, ▼T_i, ▼T_w, ▼P_h) and E5 have the highest average value of ε_b for all analysed conditions. On the other hand, experiments E7, E6 and E3 present themselves with the lowest value of this parameter with increasing strain-rate.

The results in Table 17 indicate a reduction in the variation with the increase of $\dot{\varepsilon}$, which may indicate that this material when processed with the previously mentioned conditions, experiences a more pronounced effect of the strain-rate than the ones provided by the morphological differences. It is known that an increase of $\dot{\varepsilon}$ leads to a more brittle behaviour, meaning that a higher σ_y, E and lower ε_b should be seen with a rise in the test velocity. However, the strain at break which should decrease with $\dot{\varepsilon}$ doesn't seem to do so. This detour to what was expectable can have several reasons. Higher velocities originate more friction between the polymer molecules leading to the generation of heat in the specimen during the tensile test. It is known that an increase of the test temperature induces a more ductile behaviour, having the opposite effect to that of the strain-rate (lower σ_y, E and higher ε_b). The previously studied morphological parameters also influence the tensile behaviour. Mouldings with higher content of β-spherulites should increase the strain at break and lower both σ_y and the modulus. On the other hand, a higher molecular orientation should lead to a more brittle behaviour. Since the mouldings that present pronounced Ωs are also the ones that show a relatively high β-phase content in the skin layer, their contradictory effect coupled with the low variation in the bulk crystallinity and the effect of $\dot{\varepsilon}$ doesn't allow to take any clear conclusion about what is the morphological parameter governing each tensile parameter. Also, it is reminded that the values of the modulus were calculated based on the displacement provided by the tensile apparatus which aren't the most correct and may lead to erroneous conclusions.

Table 17: Results of σ_y , E and ε_b results for all strain rates

	Yield Stress (MPa)					
	20 mm/min	Std. Dev	1 m/s	Std. Dev	3 m/s	Std. Dev
E1	18.7	0.39	25.8	0.69	29.9	0.51
E2	19.2	0.14	26.4	0.51	30.4	0.36
E3	20.0	0.25	26.8	0.19	31.0	0.37
E4	19.7	0.22	26.5	0.06	30.6	0.21
E5	18.5	0.20	25.8	0.28	29.9	0.18
E6	18.8	0.21	25.7	0.14	29.9	0.22
E7	19.1	0.13	25.1	0.11	29.6	0.13
E8	19.3	0.09	26.3	0.36	30.1	0.39
Δ	8.1%		6.6%		4.7 %	
	Modulus (MPa)					
E1	568	18.28	1499	35.67	1844	83.82
E2	537	16.16	1738	72.56	1818	50.55
E3	559	19.83	1544	36.83	1986	55.93
E4	594	9.23	1590	46.99	1994	47.63
E5	574	19.94	1531	40.58	1769	65.22
E6	590	17.83	1525	53.28	1839	42.85
E7	603	17.23	1567	59.47	1813	56.74
E8	539	19.85	1591	49.06	1962	56.46
Δ	12.3%		15.9%		12.7 %	
	Strain at Break (mm/mm)					
E1	0.773	0.024	0.657	0.031	0.569	0.028
E2	0.573	0.029	0.588	0.038	0.606	0.025
E3	0.494	0.026	0.641	0.022	0.554	0.023
E4	0.494	0.030	0.615	0.026	0.559	0.031
E5	0.664	0.026	0.617	0.028	0.626	0.020
E6	0.472	0.020	0.564	0.011	0.588	0.018
E7	0.405	0.015	0.614	0.026	0.622	0.021
E8	0.411	0.026	0.616	0.019	0.572	0.025
Δ	91.1%		16.4%		12.9 %	

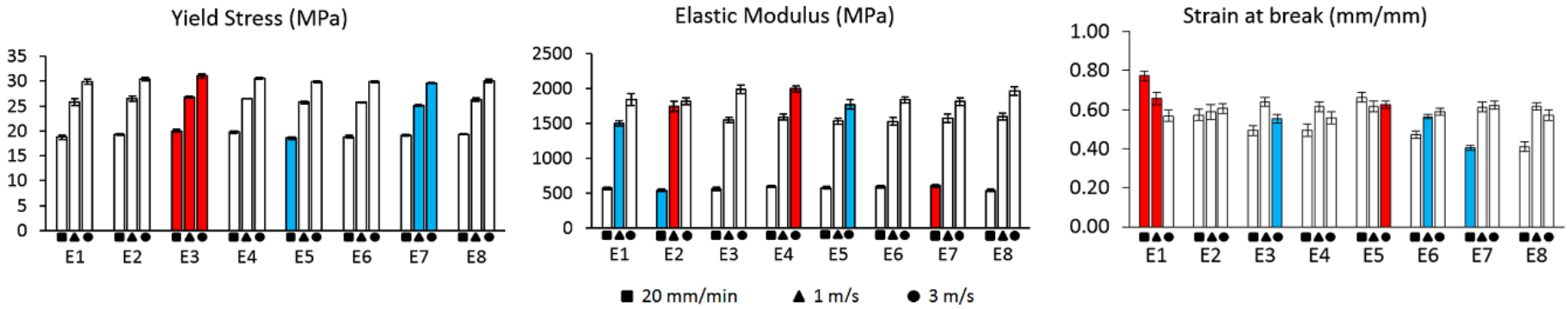

Figure 63: Variation of σ_y, E and ε_b for all experiments. The red and blue colours represent the maximum and minimum value, respectively.

According to the SAE draft [23] the quality of the curves obtained at 1 m/s (Figure 65) are classified as acceptable responses and the ones at 3 m/s (Figure 66), due to ringing, as marginally acceptable. Although the elastic properties don't have much variation, the ones in the plastic regime do. From the observation of Figures 64-66, conditions processed with lower mould temperatures (E1, E2, E3 and E4) seem to have higher strain hardening modulus than the ones processed with higher mould temperatures (E5, E6,E7 and E8). It is also observable that the strain hardening behaviour appears to be attenuated as $\dot{\varepsilon}$ increases.

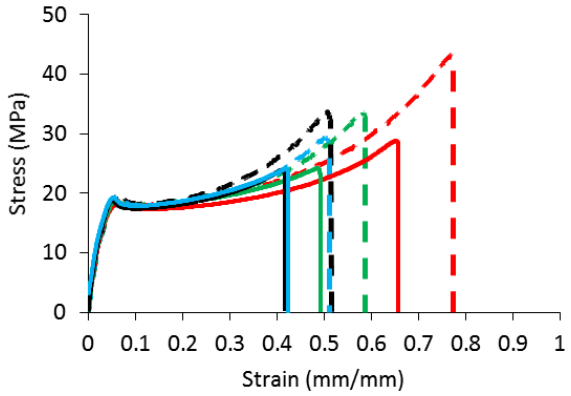

Figure 64: Tensile curves of all experiments in quasi-static tensile tests

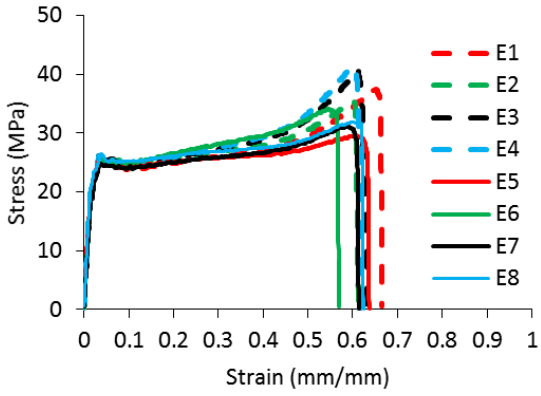

Figure 65: Tensile curves of all experiments in high speed tensile tests (1m/s)

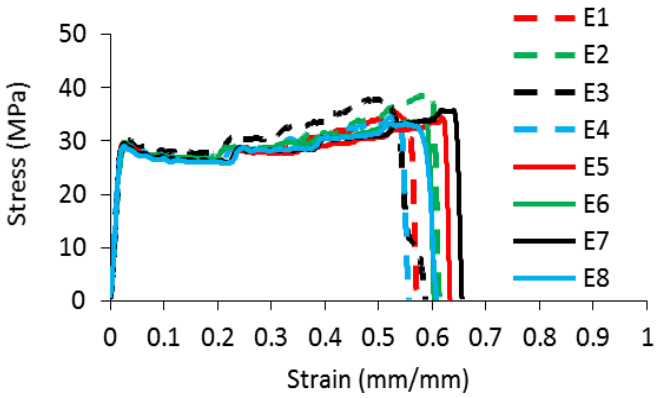

Figure 66: Tensile curves of all experiments in high speed tensile tests (3 m/s)

The analysis of variance for the quasi-static conditions indicate that σ_y is influenced by the injection (55%) and mould temperatures (26%), the modulus by the holding pressure (63%) and ε_b by the injection velocity (16%) and temperature (50%) and mould temperature (16%).

Figure 67 illustrates the influence of the main effects of the processing variables on the quasi-static mechanical properties. The values were normalised by dividing the value of each property by its respective maximum.

Figure 68 represents the interaction between the injection velocity and the injection temperature. It is observed that when using high melt temperatures the effect of the injection velocity on ε_b is almost supressed. The ANOVA tables are presented in Annex VII.

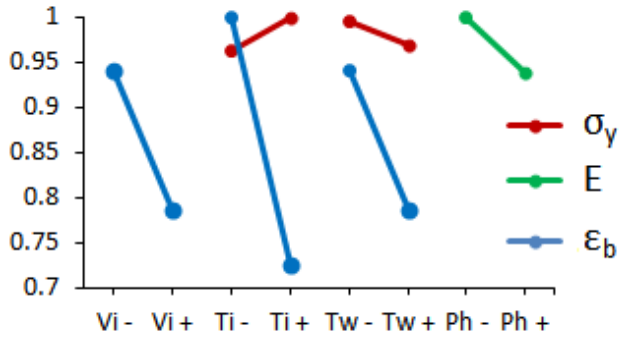

Figure 67: Effect of the main processing variables on the quasi-static tensile properties

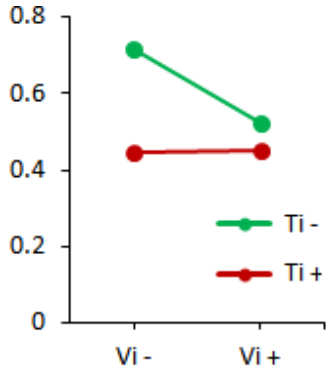

Figure 68: Interaction influencing ε_b at 20 mm/min

At 1m/s the analysis of variance indicates that σ_y is influenced by the mould temperature (38%) and the holding pressure (29%). The modulus by the injection velocity (30%), mould temperature (8%) and holding pressure (16%). Several interactions are observed for this parameter at 1m/s, all of which related to the injection velocity. Higher injection velocities seem to induce an increase in the modulus value when lowering T_i and T_w, and when increasing P_h. Regarding the strain at break, the injection velocity (47%) and mould temperature (18%) are significant parameters. Also, the interaction between the injection velocity and temperature is reported. When using a high value of v_i, lower values of T_i result in higher deformations. σ_y and ε_b both present a difference between the predicted and adjusted R^2 superior to 0.2, suggesting that there may be a large block effect or a possible problem with the statistic model. More likely due to the fact that in a L8 DOE only linear relationships can be established and no quadratic effects are accounted.

At 3 m/s the analysis of variance indicates that σ_y has the injection temperature (12%), mould temperature (52%) and hold pressure (15%) as significant parameters. For the elastic modulus, T_i.(54%), and for the strain at break, T_w (33%). Interactions are observed for both σ_y and ε_b. With high injection velocities a decrease in the hold pressure leads to higher values of σ_y. An opposing effect is observed for ε_b. For higher values of injection velocity, using lower values of T_w increases ε_b. On the other hand, using a higher value of mould temperature results in lower deformations. All evaluated parameters at this velocity presented a difference higher than 0.2 between the predicted and adjusted regression coefficient.

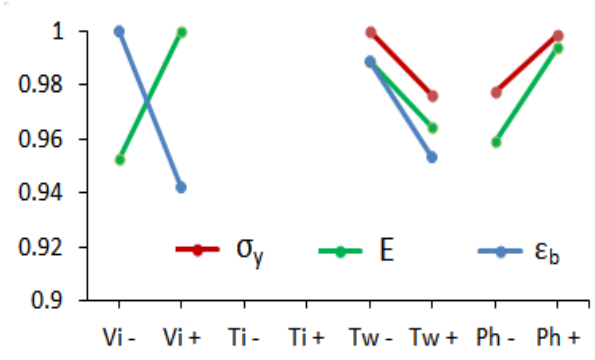

Figure 69:Effect of the main processing variables on the tensile properties measured at 1m/s

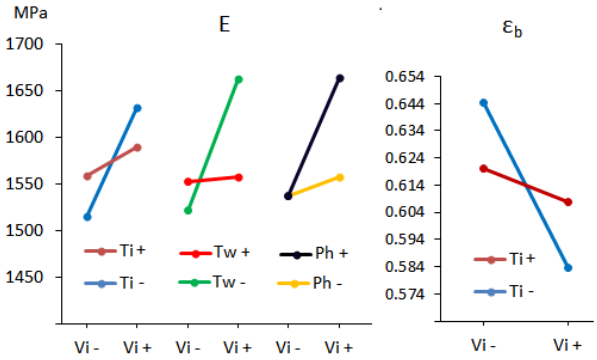

Figure 70: Interactions influencing E and ε_b at 1m/s

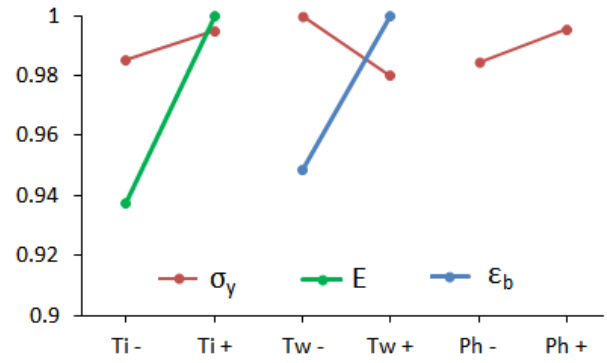

Figure 71: Effect of the main processing variables on the tensile properties measured at 3m/s

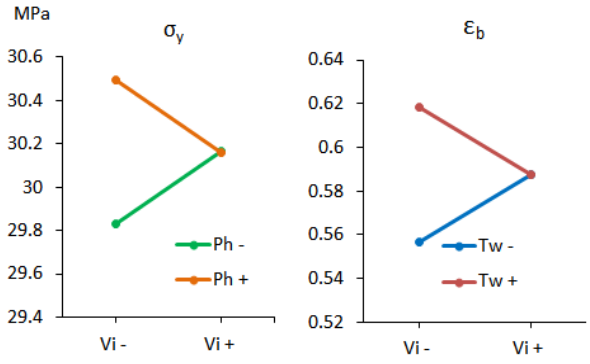

Figure 72: Interactions influencing σ_y and ε_b at 3 m/s

8.4 Relationship between TMI and the Morphological Parameters

In this section the relationship between the thermomechanical indices and the morphological parameters will be assessed in terms of regression equations. 3D plots were generated in Tablecurve3D v4.0 and the TMI (Y_C and τ_Y) were coded between -1 (minimum value) and 1 (maximum value), following equation 46, in order to compare the influence and contribution of both parameters. As was mentioned above, due to the lack of relationship only the TMIs at the end of filling will be used, meaning that the packing phase will not be accounted for. Also, the effect of some thermomechanical variables on the morphological properties were studied. A decomposition of the cooling (Y_C) and thermal-stress index (τ_Y) at the end of filling and was done in order to evaluate the difference between T_b and T_c representing the degree of superheating, and the bulk shear rate (γ) which is derived from the calculation of τ_w.

$$\psi = \frac{X - a}{b};\ \ a = \frac{X_{max} + X_{min}}{2};\ \ b = \frac{X_{max} - X_{min}}{2} \tag{46}$$

Where ψ is the coded value, X is the value of the property intended to code, X_{max} and X_{min} are the maximum and minimum value of the intended property.

As referenced before, Viana [33], [35] pioneered the implementation of the TMI methodology to establish relationships between the thermomechanical environment, morphological features and mechanical properties. The author studied the variation of the TMI in different mouldings (axisymmetric dumbbell and discs). Table 18 resumes and compares the effects of the processing conditions on Y_C and τ_Y published in his and this work's ANOVA.

Depending on the geometry used, the contribution and trend of the TMI can change. For the cooling index, the main contributors (injection temperature and mould temperature) appear to be the same. Regarding the thermal-stress index the author reported, for dumbbell specimens, that a decrease in the injection flow rate resulted in a higher τ_Y, whereas for the disc geometry higher flow rates led to a higher τ_Y. As stated in the previous section, the injection velocity as a large influence on the morphological properties of the used material and, in agreement with what the author referred, it also contributes to an increase of τ_Y.

Figures 75 to 84 compare the previously studied morphological properties with the thermomechamical indices. In all graphs referent to the TMV the coefficient "b" is the shear rate and the coefficient "c" the superheating difference. In the graphs regarding the TMI, "b" is the cooling index and "c" the thermo-stress index.

Table 18: Comparison between TMI

		Viana [33]			ANOVA		
		v_i	T_i	T_w	v_i	T_i	T_w
Disc	Y_C ▲	▲	▲	▲		▲	▲
	τ_Y ▲	▲	▲	▼	▲	▼	▼
Dumbbell	Y_C ▲	▲	▲	▲			
	τ_Y ▲	▼	▼				

Figure 73 shows the dependency of the TSI on the skin orientation. A second order polynomial was used to describe the trend of this morphological parameter. Since τ_Y is supposed to reflect the orientation

level in the moulding, a good relationship was to be expected. With a R^2 of nearly 0.61, τ_Y can be assumed to be proportional to Ωs, and it can be taken as a quantitative indication of the skin orientation. The targeted relationship between TMI and their supposed morphological parameters is further noticed when comparing the relationship between the bulk crystallinity and the cooling index. Despite not having a considerable variation the trend of CI is what was expected (higher index, higher degree of crystallinity).

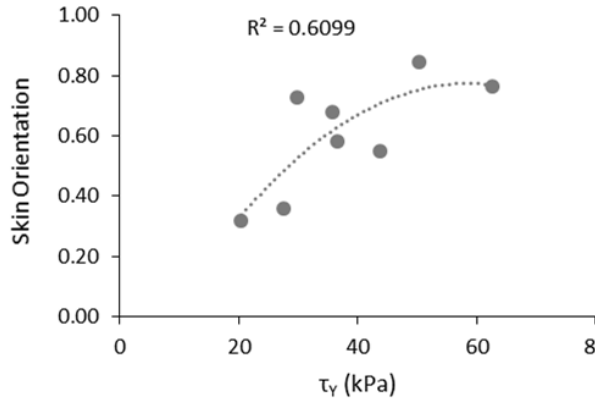

Figure 73: Relationship between the thermal-stress index and the skin orientation

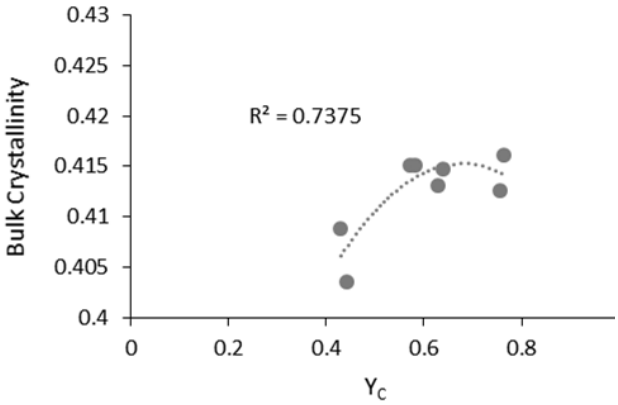

Figure 74: Relationship between the cooling index and the bulk crystallinity

As depicted in Figure 75, Sa increases for lower levels of Y_C and τ_Y. Viana in his doctoral thesis [33], reported the same trend for his injection moulded discs. Comparing the relationship between TMI and TMV it seems that Sa is more dependent upon the shear-rate and the degree of superheating than on Y_C and τ_Y. However, the trend of the dumbbell specimens studied by Viana et al. [10], [28] differs from what was obtained in this work. They reported that Sa increased with an increase of τ_Y and decrease of Y_C and observed that for higher values of Sa a high τ_Y was obtained, indirectly indicating that thicker skin layers were also more orientated.

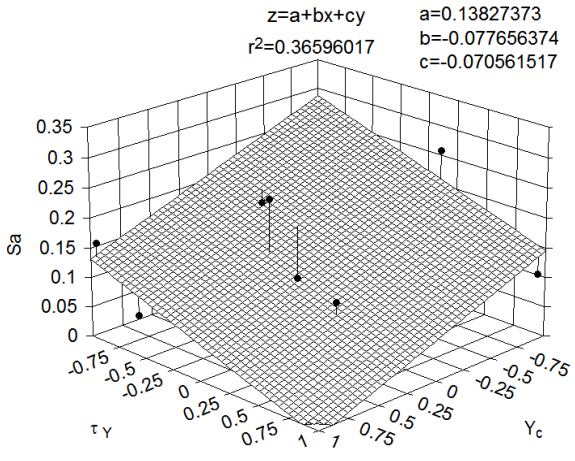

Figure 75: Relationship between the TMI and Sa

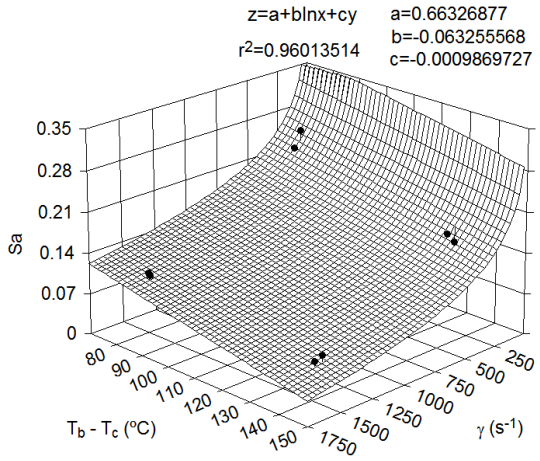

Figure 76: Relationship between the TMV and Sa

Figure 77 shows a linear relationship between the TMI and the skin orientation. It indicates that higher values of orientation are obtained for higher values of both of Y_C and τ_Y, with the double contribution by the thermo-stress index. On the other hand, when analysing

Figure 78, it is observed that the skin orientation increases for a lower value of superheating difference. Viana et al. [10] reported that higher values of Ωs were obtained for higher shear stress values and lower cooling index. In this case, the fact that the orientation increased with the thermal level can be explained by the preponderant effect of the stress level owing to rapid cooling (high heat exchanged by conduction due to a large surface area).

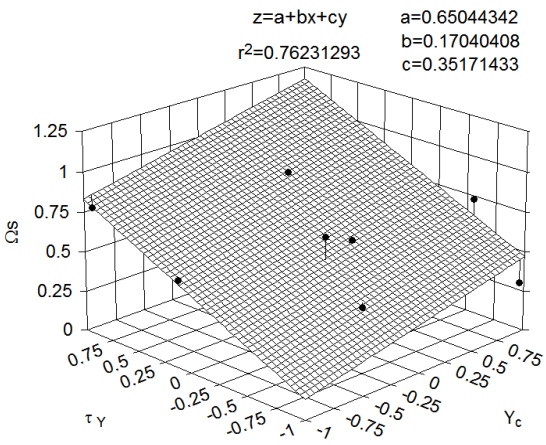

Figure 77:Relationship between the TMI and Ωs

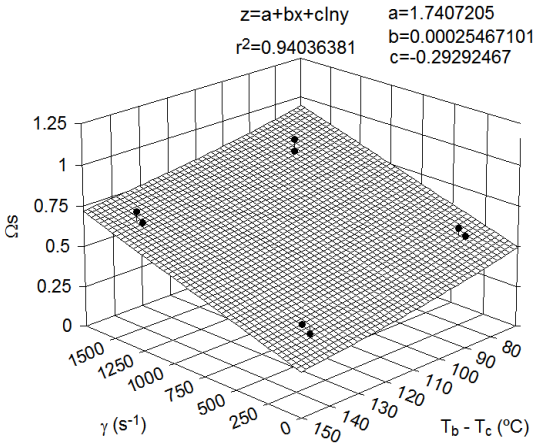

Figure 78: Relationship between the TMV and Ωx

By analysing Figure 79 one can observe the large contribution that τ_Y has on the skin crystallinity when compared to the cooling index. Higher values of this morphological parameter are reported for lower Y_C (even though with a fairly lower contribution) and higher values of the thermo-stress index. The physical significance can be explained remembering that the skin layer is formed in the first moments of the injection moulding cycle and, due to the high temperature gradient existent near the mould wall the thermal level can have its effect supressed. Also, since shear increases the nucleation density it explains the positive effect of the shear-rate on χ_{skin}.

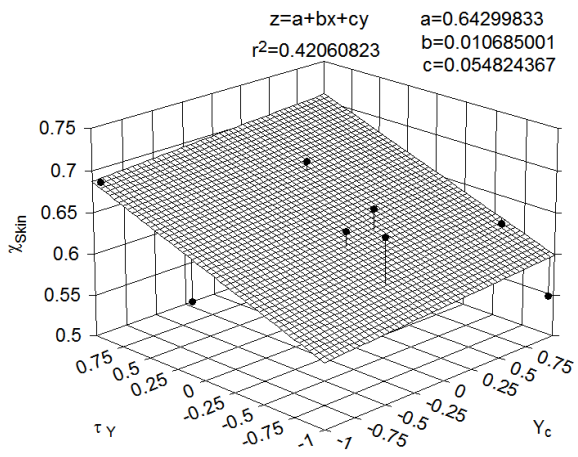

Figure 79: Relationship between the TMI and χskin

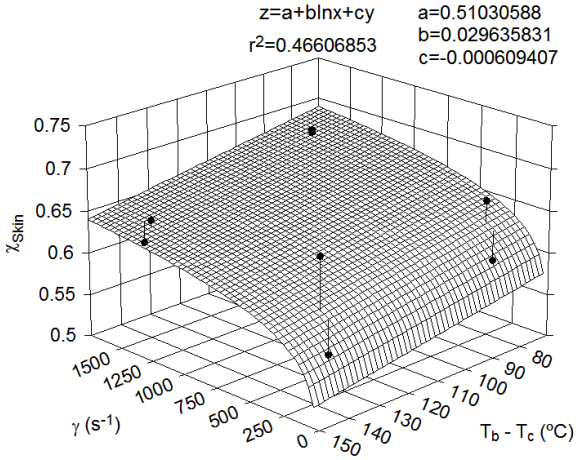

Figure 80: Relationship between the TMV and χskin

The β-phase content increases for high values of injection velocity, leading to higher values of τ_Y. In fact, the thermo-stress appears to dominate this morphological parameter with 3 times the contribution of the thermal level. The regression coefficient improves considerably when comparing the results with the thermomechanical variables. Viana et al. [10] observed in dumbbell specimens, that the β-phase content increased for higher values of the superheating difference. This difference can be due to the larger dissipation of heat in the disc geometry rendering major contribution to the shear field.

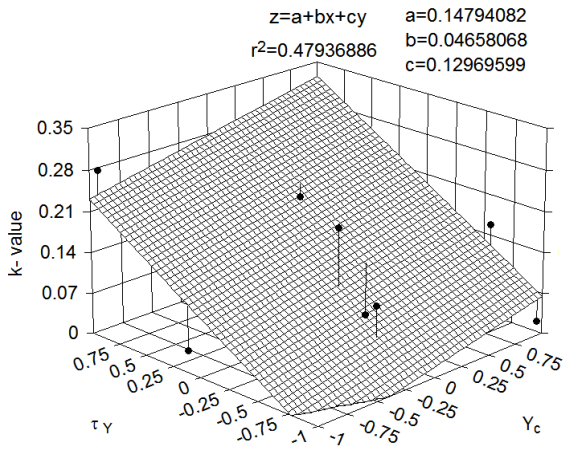

Figure 81: Relationship between the TMI and k- value

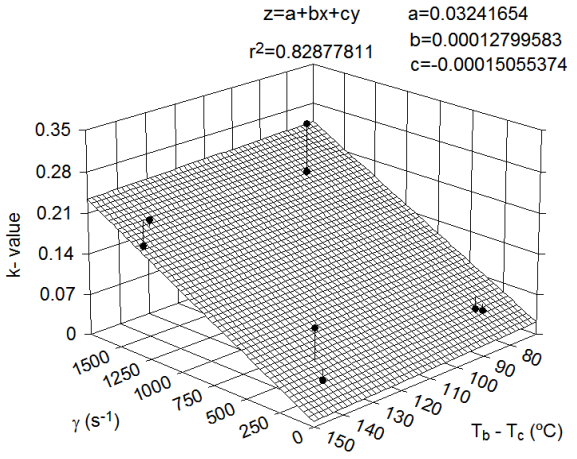

Figure 82: Relationship between the TMV and k- value

The bulk crystallinity, even though with a low variation coefficient, presents higher values for a higher thermal and lower stress level. The former level can indicate that a lower stress level, leading to more quiescent conditions tends to develop higher degree of crystallinity in the melt. Figure 84 shows the variation of χ_{Bulk} with the temperature differences that contribute for Y_C. A higher χ_{Bulk} is obtained for the highest (T_b-T_c) and lowest values of (T_b-T_{int}). However it seems that the former has the strongest

contribution, suggesting that the degree of crystallinity is governed by the cooling rate and the melt temperature [10]: it decreases with increasing cooling rate and for low melt temperatures.

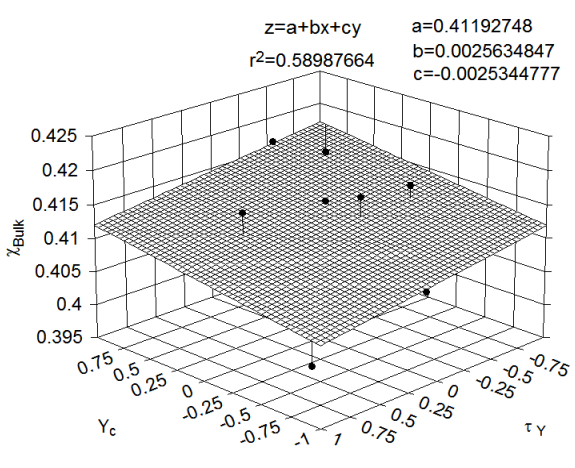

Figure 83: Relationship between the TMI and χ bulk

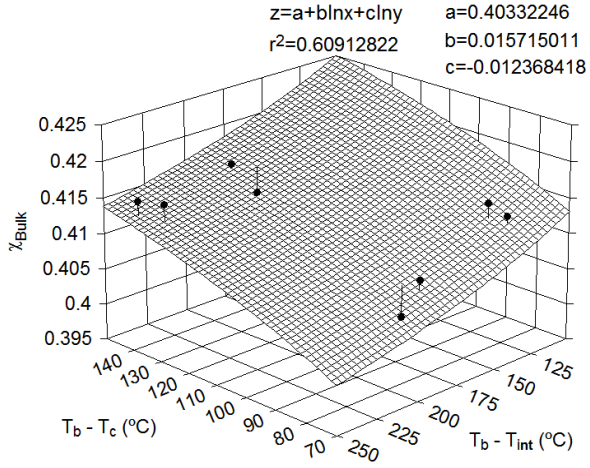

Figure 84: Relationship between the TMV and χ bulk

As a concluding remark, it appears that besides the material's physical and thermo-rheological properties, the processing conditions and geometry of the moulding show great importance to the final development of morphological properties, which in due turn have an important effect on the performance of the part. Table 19 summarizes the effect of the TMI on the evaluated morphological parameters.

Table 19: Resume of the effect of the thermomechanical indices on the morphological parameters (double arrow signifies a stronger effect)

	Y_C	τ_Y
▲ Skin Layer	▼	▼
▲ Skin Orientation	▲	▲▲
▲ Skin Crystallinity	▼	▲▲
▲ β-phase content	▲	▲▲
▲ Bulk Crystallinity	▲	▼

8.5 Relationship between TMI and the Mechanical Properties

The relative dimensions of the skin layer in the sandwich-like structure can be used to weight the effect of the TMI on the final mechanical response by assuming that the skin is mainly governed by its degree of molecular orientation and the core essentially by the degree of crystallinity. Cunha et al. [34] proposed

the following weighted TMIs: i) a weighted cooling index, ((1-Sa)Y_C), and ii) a weighted thermo-stress index (Sa τ_Y).

A comparison between non-weighted and weighted TMIs is presented in Table 20. Generally the latter results in a better fitting, so they will be used to model the mechanical properties as a function of (1-Sa) Y_C and Sa τ_Y.

Table 20: Comparison between weighted and non-weighted thermomechanical indices

	20 mm/min		R^2	1 m/s		R^2	3 m/s		R^2
	Y_C	τ_Y		Y_C	τ_Y		Y_C	τ_Y	
▲ σ_y	▼	▼	0.16	▼	▼	0.14	▼	▼	0.20
▲ E	▲	▼	0.14	▲	▲	0.25	▼	▼	0.15
▲ ε_b	▼	▼	0.59	▼	▼	0.83	▲	▲	0.17
	Weighted Indices								
	(1-Sa) Y_C	Sa τ_Y		(1-Sa) Y_C	Sa τ_Y		(1-Sa) Y_C	Sa τ_Y	
▲ σ_y	▼	▼	0.84	▼	▼	0.47	▼	▼	0.68
▲ E	-	-	0.04	▼	▼	0.27	▼	▼	0.52
▲ ε_b	▼	▲	0.92	▼	▲	0.12	▲	▲	0.24

For all tested velocities σ_y increases for lower levels of both weighted TMIs, which may indicate that a thicker skin layer, although less orientated, presents a higher yield stress. This trend is contrary to what was found in literature [28] where the yield stress increased for both weighted indices. However, in the previously mentioned study the skin thickness and molecular orientation increased with the thermo-stress index whereas with the geometry used in this work an opposing effect was observed.

The models obtained for the modulus indicate the same trend as the ones obtained for the yield stress, however with a lower relationship. If we look at the analysis of variance, it indicated that the hold pressure plays an important role in this parameter, which is not accounted for with the TMIs from the filling stage. In literature it was found that the modulus increases for higher values of both weighted thermomechanical indices following the same trend as the yield stress.

The relationship between the weighted TMIs and ε_b shifts with the imposed strain-rate, which can mean that different types of failure mechanism are activated depending on the test velocity. This type of behaviour was also found in [34].

As a concluding remark, it seems that the lack of variation in the bulk crystallinity, coupled with the concurrent effect of important morphological parameters (such as skin ratio, skin orientation and k-value)

and the effect of the strain-rate, renders rather difficult the optimization and description of these tensile properties.

9. CASE STUDY

As previously mentioned, a case study was conducted in order to evaluate the performance of the material under impact loading (falling weight impact test) to simulate the real life performance of a part. Lateral gated discs referent to 12 different processing conditions were previously moulded and provided for this project. A Taguchi L8 DOE plan was used to apply the TMI methodology and the remaining four to predict both morphological and mechanical properties. More specifically, Sa, the peak force (F_p) and puncture energy (U_b).The DOE plan for the provided mouldings is presented in Table 21.

Table 21: Case study DOE plan

		[A] = v_i (mm.s^{-1})		[B] = T_i (°C)		[C] = T_w (°C)		[D] = P_h (MPa)	
	Experiment (C)	Level	Value	Level	Value	Level	Value	Level	Value
Taguchi L8	1	-	30	-	200	-	10	-	0.5
	2	+	300	-	200	-	10	+	3
	3	-	30	+	280	-	10	+	3
	4	+	300	+	280	-	10	-	0.5
	5	-	30	-	200	+	70	+	3
	6	+	300	-	200	+	70	-	0.5
	7	-	30	+	280	+	70	-	0.5
	8	+	300	+	280	+	70	+	3
Prediction	9	-1	30	+1	280	-1	10	-1	0.5
	10	-1	30	-1	200	+1	70	-1	0.5
	11	+1	300	0	240	0	40	0	1.8
	12	0	165	0	240	0	40	0	1.8

9.1 Skin layer prediction

The skin layer was evaluated using the procedure described in section 7.6.1. Only one disc of each condition was analysed. The results range from 0.0429 (experiment C8) to 0.2334 (experiment C1) representing a variation of 444%. Figure 85 depicts the results of Sa with each processing condition for the Taguchi L8 DOE and compares them to the previously obtained values (reference).

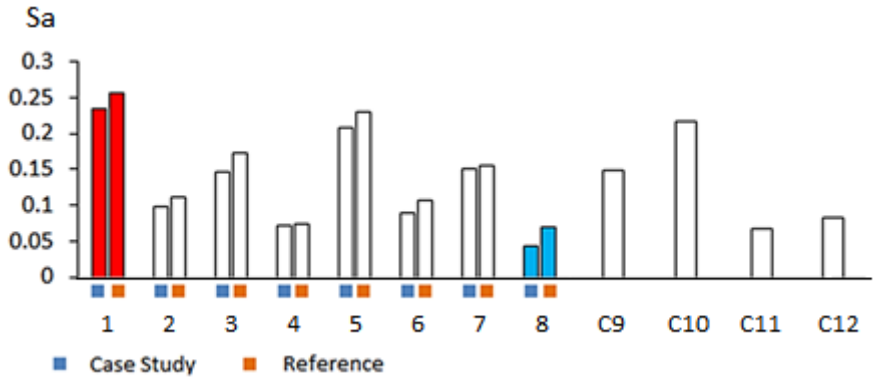

Figure 85: Variation of the skin ratio with each processing condition and comparison with reference

For the prediction of this morphological parameter, two exercises were be performed:

1. Predicting the skin ratio through the L8 DOE for the remaining 4 conditions;
2. Predicting the skin ratio through the 12 conditions the results obtained in section 8.2.1.

Since broader processing conditions were used in the case study, the idea behind the latter point assumes that the prediction is within the range of the processing conditions (interpolation). The differences between the predictions using TMI and TMV will be given bellow. Again, the bulk shear-rate and the superheating difference will be used as they provided a better regression coefficient. The 3D graphs for the TMV and respective equations are illustrated in Figures 86 and 87. The results are summarised in Table 22 and the error (Er) of prediction was calculated using equation 47.

$$Er\ (\%) = \frac{\left|Value_p - Value_m\right|}{Value_m} \times 100 \qquad (47)$$

Where the subscript p, m, represent the predicted and measured values.

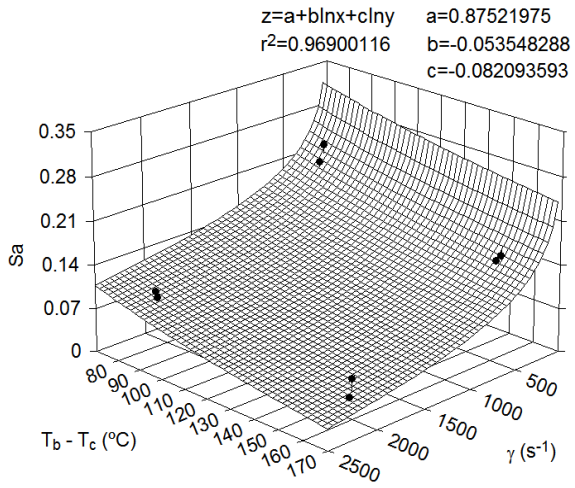

Figure 86: Relationship between the TMV and Sa for the case study's DOE plan

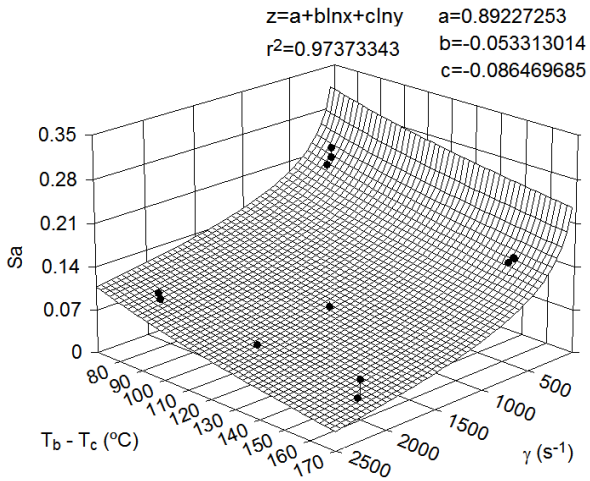

Figure 87: Relationship between the TMV and Sa for all case study's experiments

In all equations regarding the TMV the parameter "b" is the bulk shear-rate and "c" the superheating difference.

The highest error reported corresponds to experiment C12 (15%) when predicting the values with the case study's DOE and experiment E1 (13%) when using all points.

Table 22: Results of Sa prediction resorting to thermomechanical variables. The suffix –m and –P mean measured and predicted, respectively.

		γ (s^{-1})	T_b-T_c (°C)	Sa-m	Sa-P	Er (%)			γ (s^{-1})	T_b-T_c (°C)	Sa-m	Sa-P	Er (%)
Case Study	C1	265.8	78.9	0.233			DOE	E1	237.9	78.5	0.256	0.223	12.9
	C2	2176.4	83.3	0.098				E2	1538.8	82.3	0.110	0.120	8.6
	C3	334.1	155.7	0.146				E3	311.3	135.4	0.173	0.162	6.4
	C4	2046.7	161.9	0.070				E4	1449.7	141.4	0.074	0.076	2.3
	C5	312.9	79.1	0.207				E5	293.5	78.4	0.229	0.212	7.4
	C6	2170.9	83.8	0.089				E6	1533.3	82.6	0.107	0.120	12.0
	C7	271.0	155.4	0.150				E7	251.1	135.5	0.154	0.173	12.2
	C8	2072.7	162.0	0.043				E8	1507.2	141.3	0.068	0.074	8.2
	C9	271.3	155.7	0.149	0.161	7.9							
	C10	273.3	79.1	0.217	0.216	0.3							
	C11	2107.2	122.7	0.068	0.071	3.5							
	C12	1346.5	121.7	0.083	0.095	15.1							

The 3D graphs and respective equations when using the TMIs are depicted in Figures 88 and 89. In all correlations using TMIs the x-axis is represented by the cooling index and the y-axis by the thermo-stress index.

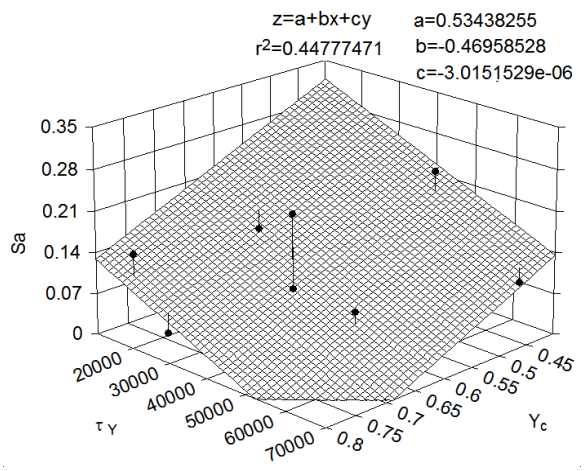

Figure 88: Relationship between the TMI and Sa for the case study's DOE plan

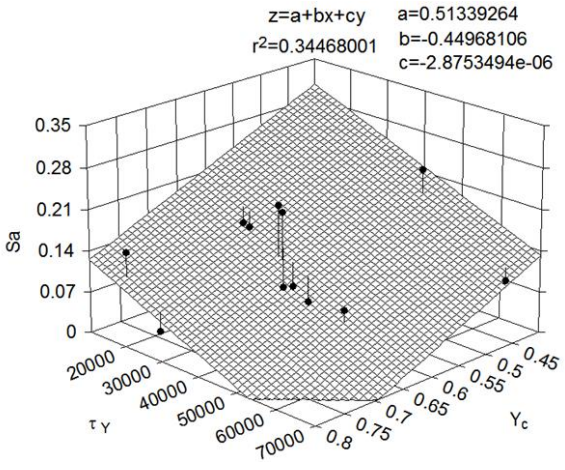

Figure 89: Relationship between the TMI and Sa for all case study's experiments

The results for the skin layer prediction are reported in Table 23. In general a higher percentage of error is evident when compared to the results obtained using TMV. When using eight points, the maximum Er obtained is 68% (experiment C11) whereas for the DOE prediction the maximum is 100% (experiment E4). The lower regression coefficient reflects itself when predicting Sa.

It is worth mentioning that the TMIs used only reflect the filling stage and that there is no calculation for the time it takes to have a fully defined skin layer within the injection cycle. Also, Y_C and τ_Y are indices which intend to have a high complexity of effects attached to them in order to quantify the thermomechanical environment. However, for some parameters such as Sa which in its core is basically a geometric reference of the sandwich-like structure, it may not have the need to be explained by such indices, where the possibility of error due to their high complexity increases.

Table 23: Results of Sa prediction using TMI

		Y_C	τ_Y	Sa- P	Er (%)			Y_C	τ_Y	Sa- P	Er (%)
Case Study	C1	0.432	44006			DOE	E1	0.430	43815	0.194	24.4
	C2	0.444	67027				E2	0.442	62677	0.135	22.1
	C3	0.607	23347				E3	0.571	27631	0.177	2.4
	C4	0.616	33881				E4	0.582	35809	0.149	100.0
	C5	0.630	35988				E5	0.628	36596	0.126	45.2
	C6	0.643	53995				E6	0.640	50369	0.081	24.3
	C7	0.783	17730				E7	0.755	20424	0.115	25.4
	C8	0.790	28144				E8	0.763	29785	0.085	23.8
	C9	0.607	21691	0.184	23.4						
	C10	0.631	34959	0.133	38.7						
	C11	0.625	41945	0.114	67.8						
	C12	0.623	37628	0.128	55.0						

9.2 Peak Force and Puncture Energy prediction

The impact tests were performed according to the ISO 6603-2 in a Fractovis Plus falling weight impact tester. The apparatus provides in detail the impact event, from the initial contact to final rupture of the specimen by recording the force- time curve of the entire impact event through a data acquisition system connected to a computer. As mentioned above, the peak force (F_p) and puncture energy (U_b) were studied. F_p is simply the highest point on the force vs time curve and U_b the amount of energy that the specimen absorbs during the complete test (with full disc penetration), defined by the ISO standard as the area bellow the curve up to the point where the force decays to 0.5 F_p. The tests were performed at

4.43 m/s (roughly 16 km/h), in order to simulate a crash at medium parking speed, with a mass of 20kg, no lubrication and a 20mm hemispherical dart. Six samples of each condition were tested, resulting in a total of 72 tests.

Figures 90 and 91 display the variation of F_p and U_b with each processing condition. Experiment C5 (▼v_i, ▼T_i, ▲T_w, ▲P_h) and C3 (▼v_i, ▲T_i, ▼T_w, ▲P_h) present, respectively, the highest value of peak force and puncture energy, while experiment C7 (▼v_i, ▲T_i, ▲T_w, ▼P_h) is the one with the lowest value for both parameters.

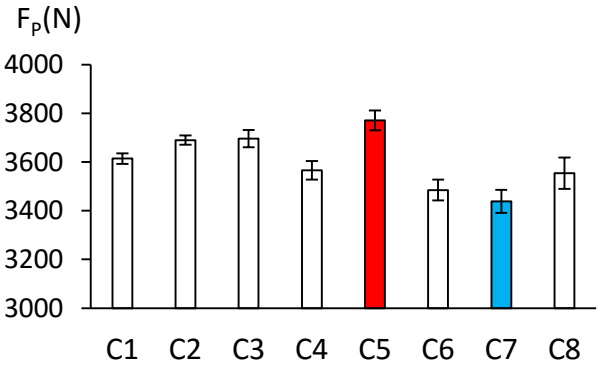

Figure 90: Variation of F_P with each processing condition

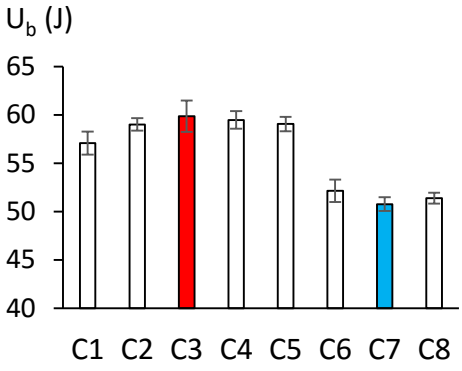

Figure 91: Variation of U_b with each processing condition

Among all the L8 experiments a variation of 10% and 20% is reported for the peak force and puncture energy, respectively. In a similar way to what happened in the high speed tensile tests a lack of variation in the mechanical properties up to the end of the elastic regime is event, only being noticed when the rupture of the specimen succeeds. However, the rupture phenomenon is a chaotic process and is influenced by several parameters which makes it hard to fully comprehend. The TMI models are depicted in Figures 92 and 93 and the prediction results in Table 24.

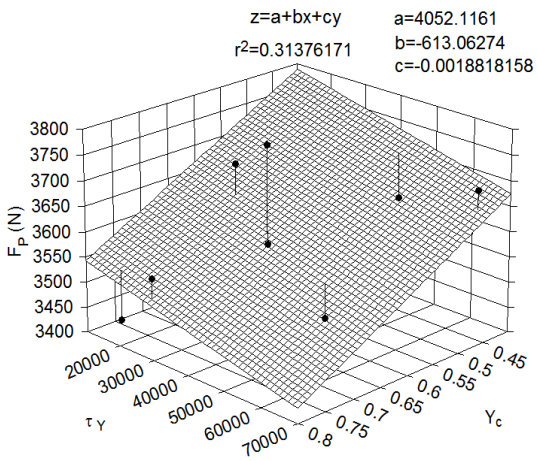

Figure 92:Relationship between the TMI and F_P

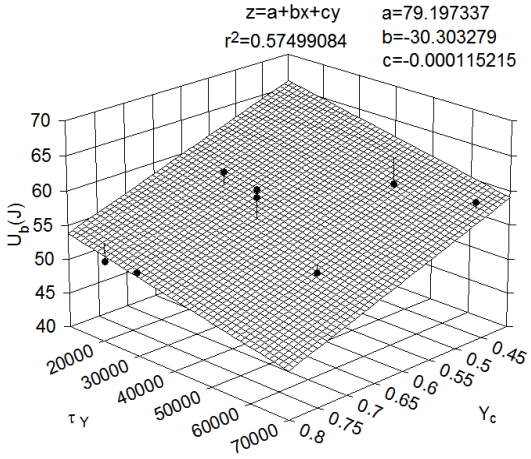

Figure 93: Relationship between the TMI and U_b

From the analysis of the predictive models one can denote a low correlation between the TMIs and the peak force, however at this test velocity the moulding presented a low coefficient of variation which is reflected in the prediction of this parameter. The maximum error for F_p is presented by experiment C9 with a value of 2.1%. Regarding the puncture energy, a higher R^2 model is obtained although it's still considered to have a low correlation. Experiment C12 presents the highest percentage of error (3.2%).

Table 24: Results of the prediction of F_p and U_b using TMI

		Y_C	τ_Y	F_P- m	Std. dev	F_P-P	Er (%)	U_b-m	Std. dev	U_b-P	Er (%)
Taguchi L8	C1	0.432	44006	3614.3	21.6			57.06	1.20		
	C2	0.444	67027	3690.1	19.1			59.00	0.65		
	C3	0.607	23347	3696.1	35.6			59.84	1.61		
	C4	0.616	33881	3566.1	38.1			59.46	0.91		
	C5	0.63	35988	3771.1	40.8			59.04	0.73		
	C6	0.643	53995	3485.1	42.4			52.14	1.16		
	C7	0.783	17730	3438.3	47.6			50.76	0.71		
	C8	0.79	28144	3554.1	64.5			51.39	0.56		
Prediction	C9	0.607	21691	3564.1	41.8	3639.2	2.1	59.80	0.86	58.30	2.5
	C10	0.631	34959	3616.0	36.4	3599.5	0.5	54.86	1.16	56.05	2.2
	C11	0.625	41945	3568.7	19.1	3590.0	0.6	56.84	0.79	55.43	2.5
	C12	0.623	37628	3638.5	31.8	3599.2	1.1	57.83	0.70	55.98	3.2

A comparison between the falling weight tests and the tensile tests can be made. With this material an increase in strain-rate leads to a more uniform behaviour up to the elastic limit. If higher variations of the mechanical parameters were observed within the case study's DOE, the results of these predictions could as been classified as undoubtedly good, however it is not the case and the TMI methodology couldn't be used to its fullest extent. A representative curve of each condition of this case study's DOE is presented in Figure 94.

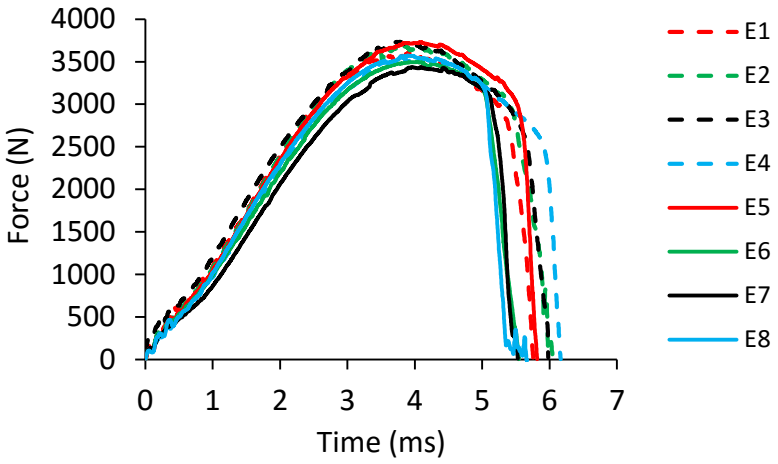

Figure 94: Falling weight impact test curves for all experiments in the DOE

10. CONCLUSIONS

In the present work different studies addressing distinct, but complementary, subjects regarding the injection moulding process were made. These contribute to the knowledge about the injection moulding process and subsequent morphological and mechanical development. The main conclusions of the thesis concerning the objectives defined in Section 1 are:

Objective i: Identify and quantify the effect of processing conditions that mainly influence the skin ratio, molecular orientation, crystallinity, the β-phase content and some mechanical properties (yield stress, modulus and strain at break)

Conclusion: The injection velocity and temperature are the main processing variables affecting the morphological development and T_w and P_h the mechanical performance.
Table 25 provides a resume of all the effects and contributions provided by the analysis of variance. Since the bulk crystallinity didn't showed a significant variation no statistical analysis was performed.

Table 25: Effect of the processing variables on the analysed morphological and mechanical properties

	v_i	%p	T_i	%p	T_w	%p	P_h	%p
Skin Ratio	▼	76	▼	20				
Skin Orientation	▲	73	▼	22				
χ_{Skin}	▲	24	▼	16	▼	4	▲	19
β-phase content	▲	81			▼	10		
Quasi-static σ_y			▲	55	▼	26		
Quasi-static E							▼	63
Quasi-static ε_b	▼	16	▼	50	▼	16		
σ_y at 1 m/s					▼	38	▲	29
E at 1m/s	▲	30			▼	8	▲	16
ε_b at 1m/s	▼	47			▼	18		
σ_y at 3 m/s			▲	12	▼	52	▲	15
E at 3m/s			▲	54				
ε_b at 3m/s					▲	33		

Objective ii: Characterise the thermomechanical environment of the different processing conditions with an injection moulding simulation software, namely Autodesk Moldflow Insight 2012;

Conclusion: The execution of this goal was carried out by calculating several thermomechanical indices referent to different stages of the injection moulding cycle. A lack of correlation was found between the indices calculated for the filling stage and the ones at the end of the packing and cooling stages, which can suggest that the method by which they were weighted is not the most correct. For the rest of the work the TMIs pertaining to the filling stage were used.

Objective iii: Correlate the obtained results from the morphological and mechanical characterisation with the thermomechanical indices methodology.

Conclusion: The thermo-stress index represents a major contribution in all morphological parameters. Morphological parameters that should improve and decrease mechanical properties were found to be promoted by the same indices and processing variables.
Regarding the mechanical properties, it was employed the use of skin weighted TMIs since they provided a better fitting. A relatively good regression coefficient was obtained for the yield stress, and a less good for the remaining mechanical parameters. Apparently, with this geometry, the yield stress and modulus increase for lower levels of both weighted indices. The strain at break shows an inversion in the relationship with increasing strain-rate which can indicate that different failure mechanism are activated depending on the test velocity.

Objective iv: Evaluate the performance of some supplied lateral injected discs in a falling weight impact test and establish a model to predict the peak force and puncture energy (case study).

Conclusion: It was found that experiment C5 and C3 present the highest value of peak force and puncture energy, respectively. Experiment C7 showed the lowest values of both parameters.
The predictive models established by the TMI methodology were used to describe the previous mechanical properties, however no significant results were obtained. The prediction of a morphological parameter, namely the skin ratio, was also carried out. Models established by thermomechanical variables and indices were used to predict this parameter. A good relationship and subsequent prediction values were obtained when using thermomechanical variables, which can indicate that for some

morphological parameters the used TMIs, due to their large account of effects, can induce more error in the regression models.

As a final remark it is worth mentioning that in both the case study's DOE and the one previously executed, a small variation of the mechanical properties was reported. This can be due to the synergetic effect provided by the lack of variation in the bulk crystallinity of the specimens, the opposing effect of the morphological parameters and the effect of strain-rate which didn't allow the use of the full extent of this methodology. Also, it is reminded that the thermomechanical indices methodology is still under development and that the used TMIs didn't account the effect of the hold pressure and the effect of polymorphism (β-phase content) which are important for the correct modelling of the mechanical behaviour of this material.

10.1 Future Work

For future work the following is proposed:

- Assess the elastic modulus by performing a dynamic mechanical analysis test to obtain its value in both quasi-static and high speed solicitations.
- Extend the morphological characterisation by, for example, assessing the crystalline lamella thickness. Further morphological parameters may allow other kind of insight on what controls the mechanical response of this material.
- Further development in the TMI equations to allow the passage of the TMIs calculated at the end of filling to the other stages.
- Evaluate the strain and displacement fields to observe the deformation behaviour of a specimen. This can be done by filming a tensile test and use a technique called Digital Image Correlation. It consists in painting a random speckle pattern on a tensile specimen and with the use of an algorithm track the deformation of the pattern, which after computation results in a displacement and strain field.

REFERENCES

[1] PlasticsEurope, "ISSUU - Plastics - the facts 2014/2015 by PlasticsEurope." pp. 1–34, 2015.

[2] M. Fujiyama and T. Wakino, "Structure of skin layer in injection-molded polypropylene," J. Appl. Polym. Sci., vol. 35, no. Journal of Applied Polymer Science, pp. 29–49, 1988.

[3] M. Fujiyama and K. Azuma, "Skin/ Core Morphology and Tensile Impact Strength of Injection-Molded Polypropylene," J. Appl. Polym. Sci., vol. 23, pp. 2807–2811, 1979.

[4] J. Housmans, M. Gahleitner, G. W. M. Peters, and H. E. H. Meijer, "Structure – property relations in molded , nucleated isotactic polypropylene," Polymer (Guildf)., vol. 50, no. 10, pp. 2304–2319, 2009.

[5] C. Shen, G. Zheng, C. Liu, Y. Wang, J. Chen, and X. Peng, "Skin Thickness and β - Crystals Development in Injection-Molded iPP Along the Flow Direction," J. Macromol. Sci. Part B, vol. 48, no. February, pp. 439–448, 2009.

[6] J. C. Viana, "Development of the skin layer in injection moulding: Phenomenological model," Polymer (Guildf)., vol. 45, pp. 993–1005, 2004.

[7] M. M. Favaro, M. C. Branciforti, and R. E. S. Bretas, "A X-ray study of β - phase and molecular orientation in nucleated and non-nucleated injection molded polypropylene resins," Mater. Res., vol. 12, no. 4, pp. 455–464, 2009.

[8] R. Mendoza, G. Régnier, W. Seiler, and J. Lebrun, "Spatial distribution of molecular orientation in injection molded iPP: influence of processing conditions," Polymer (Guildf)., vol. 44, pp. 3363–3373, 2003.

[9] T. B. Van Erp, L. E. Govaert, and G. W. M. Peters, "Mechanical performance of injection-molded poly(propylene): Characterization and modeling," Macromol. Mater. Eng., vol. 298, pp. 348–358, 2013.

[10] J. C. Viana, A. M. Cunha, and N. Billon, "The thermomechanical environment and the microstructure of an injection moulded polypropylene copolymer," Polymer (Guildf)., vol. 43, pp. 4185–4196, 2002.

[11] J. Varga and J. Karger-Kocsis, "Rules of Supermolecular Structure Formation in Sheared Isotactic Polypropylene Melts," J. Polym. Sci. Part B Polym. Phys., vol. 34, pp. 657–670, 1996.

[12] C. Tribout, B. Monasse, and J. M. Haudin, "Experimental study of shear-induced crystallization of an impact polypropylene copolymer," Colloid Polym. Sci., vol. 274, no. 3, pp. 197–208, 1996.

[13] R. Čermák, M. Obadal, P. Ponížil, M. Polášková, K. Stoklasa, and J. Hecková, “Injection-moulded α and β -polypropylenes: I. Structure vs. processing parameters,” Eur. Polym. J., vol. 41, no. 8, pp. 1838–1845, Aug. 2005.

[14] C. Zhang, G. Liu, Y. Song, Y. Zhao, and D. Wang, “Structural evolution of β - iPP during uniaxial stretching studied by in-situ WAXS and SAXS,” Polymer (Guildf)., vol. 55, no. 26, pp. 6915–6923, 2014.

[15] R. Čermák, M. Obadal, P. Ponížil, M. Polášková, K. Stoklasa, and J. Hecková, “Injection-moulded α - and β - polypropylenes:II . Tensile properties vs . processing parameters,” Eur. Polym. J., vol. 42, pp. 2185–2191, 2006.

[16] G. Kalay and J. Bevis, “Injection molding of isotactic polypropylene,” in Polypropylene: An A-Z Reference, J. Karger-Kocsis, Ed. Springer Netherlands, 1999, pp. 329–34.

[17] J. Viana, A. Cunha, and N. Billon, “The effect of the skin thickness and spherulite size on the mechanical properties of injection mouldings,” J. Mater. Sci., no. 36, pp. 4411–4418, 2001.

[18] A. Van Der Wal, J. J. Mulder, and R. J. Gaymans, “Fracture of polypropylene : 2 . The effect of crystallinity,” Polymer (Guildf)., vol. 39, no. 22, pp. 5477–5481, 1998.

[19] T. Parenteau, G. Ausias, Y. Grohens, and P. Pilvin, “Structure, mechanical properties and modelling of polypropylene for different degrees of crystallinity,” Polymer (Guildf)., vol. 53, no. 25, pp. 5873–5884, Nov. 2012.

[20] P. Tordjeman, C. Robert, G. Marin, and P. Gerard, “The effect of α , β -crystalline structure on the mechanical properties of polypropylene,” Eur. Phys. J. E, vol. 4, pp. 459–465, 2001.

[21] J. C. Viana, “Structural interpretation of the strain-rate, temperature and morphology dependence of the yield stress of injection molded semicrystalline polymers,” Polymer (Guildf)., vol. 46, no. 25, pp. 11773–11785, 2005.

[22] G. Kalay and M. J. Bevis, “Processing and Physical Property Relationships in Injection- Molded Isotactic Polypropylene . 1 . Mechanical Properties,” J. Polym. Sci., vol. 35, pp. 241–263, 1997.

[23] “High Strain Rate Tensile Testing of Polymers J2749.” SAE international, 2008.

[24] M. Zrida, H. Laurent, V. Grolleau, G. Rio, M. Khlif, D. Guines, N. Masmoudi, and C. Bradai, “High-speed tensile tests on a polypropylene material,” Polym. Test., vol. 29, no. 6, pp. 685–692, 2010.

[25] S. R. Raisch and B. Möginger, “High rate tensile tests - Measuring equipment and evaluation,” Polym. Test., vol. 29, pp. 265–272, 2010.

[26] M. Schoßig, C. Bierögel, W. Grellmann, and T. Mecklenburg, “Mechanical behavior of glass-fiber reinforced thermoplastic materials under high strain rates,” Polym. Test., vol. 27, pp. 893–900, 2008.

[27] X. Xiao, “Dynamic tensile testing of plastic materials,” Polym. Test., vol. 27, pp. 164–178, 2008.

[28] J. C. Viana, N. Billon, and A. M. Cunha, “The Thermomechanical Environment and the Mechanical Properties of Injection Moldings,” Polym. Eng. Sci., vol. 44, no. 8, pp. 1522–1533, 2004.

[29] M. Zrida, H. Laurent, G. Rio, S. Pimbert, V. Grolleau, N. Masmoudi, and C. Bradai, “Experimental and numerical study of polypropylene behavior using an hyper-visco-hysteresis constitutive law,” Comput. Mater. Sci., vol. 45, no. 2, pp. 516–527, 2009.

[30] F. Bédoui, J. Diani, and G. Régnier, “Micromechanical modeling of elastic properties in polyolefins,” Polymer (Guildf)., vol. 45, pp. 2433–2442, 2004.

[31] J. S. Godinho, A. Cunh, and R. J. Crawford, “Prediction of mechanical properties of polyethylene mouldings based on laminate theory and thermomechanical indices,” Plast. Rubber Compos., vol. 29, no. 7, pp. 329–339, 2000.

[32] C. N. Barbosa, F. Carvalho, J. C. Viana, M. Franzen, and R. Simoes, “Impact performance prediction of injection-molded talc-filled polypropylene through thermomechanical environment assessment,” Int. J. Adv. Manuf. Technol., vol. 77, pp. 873–883, Oct. 2015.

[33] J. Viana, “Mechanical Characterization of Injection Moulded Plates,” Ph.D dissertation, Dep.Polymer Eng., University of Minho, 1999.

[34] A. M. Cunha, J. S. Godinho, and J. C. Viana, “Processing-structure-properties relationships in injection moulded parts,” in Structure Development During Polymer Processing, 2000, pp. 255 – 277.

[35] J. C. Viana, M. Cunha, and N. Billon, “The Tensile Behaviour of an Injection-Moulded Propylene – Ethylene Copolymer : the Effect of the Local,” Polym. Int., vol. 43, no. 2, pp. 159–166, 1997.

[36] A. W. Phillips, A. Bhatia, P. Zhu, and G. Edward, “Shish Formation and Relaxation in Sheared Isotactic Polypropylene Containing Nucleating Particles,” Macromolecules, vol. 44, no. 9, pp. 3517–3528, May 2011.

[37] M. Demiray and A. I. Isayev, “Effect of Processing Conditions on Crystallinity and Microstructure of Injection Moldings of Polypropylenes of various Molecular Weights,” in SPE ANTEC, 1996, pp. 1576–1580.

[38] Y. Zhou and P. K. Mallick, “Effects of Melt Temperature and Hold Pressure on the Tensile and Fatigue Properties of an Injection Molded Talc-Filled Polypropylene,” Polym. Eng. Sci., vol. 45, no. 6, pp. 755–763, 2005.

[39] J. L. Way, J. R. Atkinson, and J. Nutting, “The effect of spherulite size on the fracture morphology of polypropylene,” J. Mater. Sci., vol. 9, pp. 293–299, 1974.

[40] A. M. Cunha and A. J. Pontes, “Non-Conventional Injection Molds,” in Injection Molding: Fundamentals and Applications, Hanser, 2009, pp. 167–190.

[41] A.M.Cunha, “Processo de moldação de injecção de termoplásticos,” in Manual do Projectista para moldes de injecção de plástico, University of Minho, 2003, pp. 13–78.

[42] J. C. Viana, “Reduction of Cycle Time in Injection Molding.” Class Lecture for Polymer Processing II, Dept. of Polymer Eng.,University of Minho, pp. 1–14, 2013.

[43] M. Vishnuvarthanan, R. Panda, and S. Ilangovan, “Optimization of Injection Molding Cycle Time Using Moldflow Analysis,” Middle East J. Sci. Res., vol. 13, no. 7, pp. 944–946, 2013.

[44] J. Zhu and C. Wang, “Flow analysis in injection molding process based on MoldFlow,” in Mechanic Automation and Control Engineering (MACE), 2010 International Conference on, 2010, pp. 19–22.

[45] H. Shin and Eun-Soo Park, “Analysis of Crack Phenomenon for Injection-Molded Screw Using Moldflow Simulation,” Polym. Polym. Compos., vol. 21, pp. 449–456, 2013.

[46] M. Juraeva and K. J. R. D.J.Song, “Gate Shape Optimization using Design of Experiment to Reduce the Shear Rate aroung the Gate,” Int. J. Automot. Technol., vol. 14, no. 4, pp. 659–666, 2013.

[47] C. . Barbosa, F. Carvalho, Viana J.C., M. Franzen, T. Baranowski, and R. Simoes, “Applying flow simulation outputs in the development process of thermoplastic parts,” in 6th Internation PMI Conference, 2014, pp. 165–171.

[48] C. N. Barbosa, R. Simoes, M. Franzen, and J. C. Viana, “Thermomechanical environment characterisation in injection moulding and its relation to the mechanical properties of talc-filled polypropylene,” J. Mater. Sci., vol. 48, no. 6, pp. 2597–2607, 2013.

[49] D. Tripathi, “Introduction,” in Practical Guide to Polypropylene, Rapra Technology Ltd., 2002, p. 1.

[50] J. H. . Han, William J . Kissel, and Jeffrey A . Meyer, “Polypropylene: Structure, Properties, Manufacturing Processes, and Applications,” in Handbook of Polypropylene and Polypropylene composites, H. Karian, Ed. 2003, pp. 10–27.

[51] C. Zhang, Y. Shangguan, R. Chen, Y. Wu, F. Chen, Q. Zheng, and G. Hu, “Morphology, microstructure and compatibility of impact polypropylene copolymer,” Polymer (Guildf)., vol. 51, no. 21, pp. 4969–4977, 2010.

[52] F. J. Keith and Padden H. D., “Spherulitic Crystallization in Polypropylene,” J. Appl. Phys., vol. 30, pp. 1479–1484, 1959.

[53] J. Varga, “β - Modification of Isotactic Polypropylene: Preparation, Structure, Processing, Properties, and Application,” J. Macromol. Sci. Part B, vol. 41, no. 4, pp. 1121–1171, Jan. 2002.

[54] R. G. Alamo, M.-H. Kim, M. J. Galante, J. R. Isasi, and L. Mandelkern, “Structural and kinetic factors governing the formation of the γ polymorph of isotactic polypropylene,” Macromolecules, vol. 32, p. 4050, 1999.

[55] G. Kalay, Z. Zhong, P. Allan, and M. J. Bevis, “The occurrence of the γ - phase in injection moulded polypropylene in relation to the processing conditions,” Polymer (Guildf)., vol. 37, no. 11, pp. 2077–2085, 1996.

[56] A. Marigo, V. Causin, C. Marega, and P. Ferrari, “Crystallization of the y- form in random propylene-ethylene copolymers,” Polym. Int., vol. 53, no. August 2004, pp. 2001–2008, 2004.

[57] V. Brucato, S. Piccarolo, and V. La Carrubba, “An experimental methodology to study polymer crystallization under processing conditions . The infuence of high cooling rates,” Chem. Eng. Sci., vol. 57, pp. 4129–4143, 2002.

[58] J. Antony, “Fundamentals of Design of Experiments,” in Design of Experiments for Engineers and Scientists, Second Edi., Elsevier, 2014, pp. 7–8.

[59] M.-T. Chuang, Y.-K. Yang, and Y.-H. Hsiao, “Modeling and Optimization of Injection Molding Process Parameters for Thin-Shell Plastic Parts,” Polym. Plast. Technol. Eng., vol. 48, no. 7, pp. 745–753, Jun. 2009.

[60] J. C. Viana and A. M. Cunha, “The Impact Behavior of Weld-Lines in Injection Molding,” J. Inject. Molding Technol., vol. 6, no. 4, pp. 259–271, 2002.

[61] R. E. Walpole, Raymond H. Myers, Sharon L. Myers, and Keying Ye, “Probability & Statistics for Engineers & Scientists.” Pearson Education, Inc, pp. 507–654, 2011.

[62] D. Murphy, “Properties of Polarized Light,” in Fundamentals of light microscopy and Electronic, John Wiley & Sons, Inc., 2001, pp. 117–119.

[63] M. Kudrna and M. Mitterpachova, “Orientation of polypropylene fibre,” Colloid Polym. Sci., vol. 261, pp. 903–907, 1983.

[64] X. Yu, H. Wu, J. Li, S. Guo, and J. Qiu, “Structure and property of injection-molded polypropylene along the flow direction,” Polym. Eng. Sci., vol. 49, no. 4, pp. 703–712, Apr. 2009.

[65] D. W. van der Meer, B. Pukánszky, and G. J. Vancso, “On the Dependence of Impact Behavior on the Crystalline Morphology in Polypropylenes,” J. Macromol. Sci. Part B, vol. 41, no. 4, pp. 1105–1119, Jan. 2002.

[66] B. E. Tiganis, R. a. Shanks, and Y. Long, “Effects of processing on the microstructure, melting behavior, and equilibrium melting temperature of polypropylene,” J. Appl. Polym. Sci., vol. 59, no. 4, pp. 663–671, 1996.

[67] J. Jay Theoddore Cremer, “Brief History and Overview of Diffractive and Reflective X-Ray Optics and Microscopy,” in Advances in Imaging and Electron Physics, Elsevier Inc, 2012, pp. 283–284.

[68] M. Teena and A. Manickavasagan, “Introduction to the Electromagnetic Spectrum,” in Imaging with Electromagnetic Spectrum, 2014, pp. 1–2.

[69] N. Stribeck, “Applications of Synchrotron Light to Scattering and Diffraction in Materials and Life Sciences,” in Springer-Verlag Berlin Heidelberg, vol. 776, no. 2009, 2009, pp. 23–60.

[70] Z. Z. Denchev and J. C. Viana, “X-ray Scattering Studies on Multiphasic Polymer Systems,” in Handbook of Multiphase Polymer Systems, John Wiley & Sons, Ltd, 2011, pp. 673–678.

[71] A. M. Glazer and G. Burns, “Space Groups for Solid State Scientists.” Academic Press Inc., pp. 16–63, 1990.

[72] R. K. , Rajagopal, “Crystal Physics,” in Engineering Physics, 2007, pp. 43–72.

[73] P. Zipper, A. Jánosi, W. Geumayer, E. Ingolic, and E. Fleischmann, “Comparative X-Ray Scattering, Microscopical, and Mechanical Studies on Rectangular Plates Injection Molded From Different Types of Isotactic,” Polym. Eng. Sci., vol. 36, no. 4, pp. 467–482, 1996.

[74] M. L. Maspoch, J. Gamez-Perez, E. Gimenez, O. Santana, and A. Gordillo, “Influence of processing on ethylene-propylene block copolymers: Structure and mechanical behavior,” J. Appl. Polym. Sci., vol. 93, no. 6, pp. 2866–2878, Sep. 2004.

[75] A. T. Jones, J. M. Aizlewood, and D. R. Beckett, “Crystalline forms of isotactic polypropylene,” Die Makromol. Chemie, vol. 75, no. 1, pp. 134–158, 1964.

[76] J. D. Menczel and R. B. Prime, “Differential Scanning Calorietry (DSC),” in Thermal Analysis of Polymers: Fundamentals and Applications, 2008, pp. 7–8.

[77] J. R. Davis, “Introduction to Tensile Testing,” in Tensile testing, Second Edi., A. International, Ed. 2004, pp. 1–13.

[78] C. A. Daniels, “Tensile Properties,” in Polymer structure and properties, Technomic Publishing Company, 1989, pp. 43–48.

[79] D. A. Şerban, G. Weber, L. Marşavina, V. V. Silberschmidt, and W. Hufenbach, “Tensile properties of semi-crystalline thermoplastic polymers: Effects of temperature and strain rates,” Polym. Test., vol. 32, pp. 413–425, 2013.

[80] Plastics and Rubber Standard Policy Committe, “Part 1: General principles,” BS EN ISO 527-2 Plast. - Determ. tensile Prop., vol. 1, no. 1, pp. 1–16, 1996.

[81] X. S. Xiao and M. Leach, “Intermediate And High Strain Rate Tensile Testing Of Plastic Materials,” General Motors Corporation, Warren, MI (2005): 48090-9055. .

[82] P. H. Mott, J. N. Twigg, D. F. Roland, H. S. Schrader, J. a. Pathak, and C. M. Roland, “High-speed tensile test instrument,” Rev. Sci. Instrum., vol. 78, pp. 1–6, 2007.

[83] L. Aretxabaleta, J. Aurrekoetxea, I. Urrutibeascoa, and M. Sa, “Characterisation of the impact behaviour of polymer thermoplastics,” Polym. Test., vol. 24, pp. 145–151, 2005.

[84] S. F. Lee and G. M. Swallowe, “Direct measurement of high rate stress-strain curves using instrumented falling weight and high-speed photography,” Imaging Sci. J., vol. 52, pp. 193–202, 2004.

[85] T. Gzigany and J. Karger-Kocsis, “Comparison of the Instrumented Falling Weight Impact Response of Polypropylene Composites Reinforced by Continuous and Discontinuous Fiber Mats,” J. Reinf. Plast. Compos., vol. 20, no. 12, pp. 996–1012.

[86] S. C. Chou, K. D. Robertson, and J. H. Rainey, “The effect of strain rate and heat developed during deformation on the stress-strain curve of plastics,” Exp. Mech., vol. 13, no. October, pp. 422–432, 1973.

[87] J. M. Berry, W. Brostow, M. Hess, and E. G. Jacobs, “P-V-T relations in a series of longitudinal polymer liquid crystals with varying mesogen concentration,” Polymer (Guildf)., vol. 39, no. 17, pp. 4081–4088, 1998.

[88] Autodesk Moldflow Insight Standard 1: Practice for release 2010. Autodesk, Inc, 2009.

[89] T. Nishino, T. Matsumto, and K. Nakamae, “Surface structure of isotactic polypropylene by X-ray diffraction,” Polym. Eng., vol. 40, no. 2, 2000.

[90] “http://henke.lbl.gov/optical_constants/atten2.html,” 2015.

[91] M. Farah and R. E. S. Bretas, “Characterization of i-PP Shear-Induced Crystallization Layers Developed in a Slit Die,” Polymer (Guildf)., 2003.

[92] B. Monasse and J. M. Haudin, “Effect of random copolymerization on growth transition and morphology change in polypropylene,” Colloid Polym. Sci., vol. 266, no. 8, pp. 679–687, 1988.

ANNEXES

Table of Contents

INDEX OF FIGURES

INDEX OF TABLES

ANNEX I – DATA SHEET OF HOSTACOM EP3307

lyondellbasell

Hostacom EP3307

Compounded Polyolefin

Product Description

EP3307 is a low density, high impact , UV stabilised grade for automotive interior parts

Product Characteristics

Status	Commercial: Active
Test Method used	ISO
Features	Copolymer, Low Density, Good Impact Resistance , Good Processability, Medium Rigidity , UV Resistant
Typical Customer Applications	Interior Applications

Typical Properties	Method	Value Unit
Physical		
Density	ISO 1183	0.92 g/cm³
Melt flow rate (MFR) (230°C/2.16Kg)	ISO 1133	15 g/10 min
Mechanical		
Flexural modulus	ISO 178	1100 MPa
Impact		
Notched izod impact strength	ISO 180	
(- 30 °C)		5 kJ/m²
(23 °C)		40 kJ/m²
Thermal		
Heat deflection temperature B (0.45 MPa) Unannealed	ISO 75B-1, -2	95 °C

Notes

Typical properties; not to be construed as specifications.

Figure i: Data sheet of Hostacom EP3307

ANNEX II – FEEDING SYSTEM AND PART ENGINEERING DRAWING

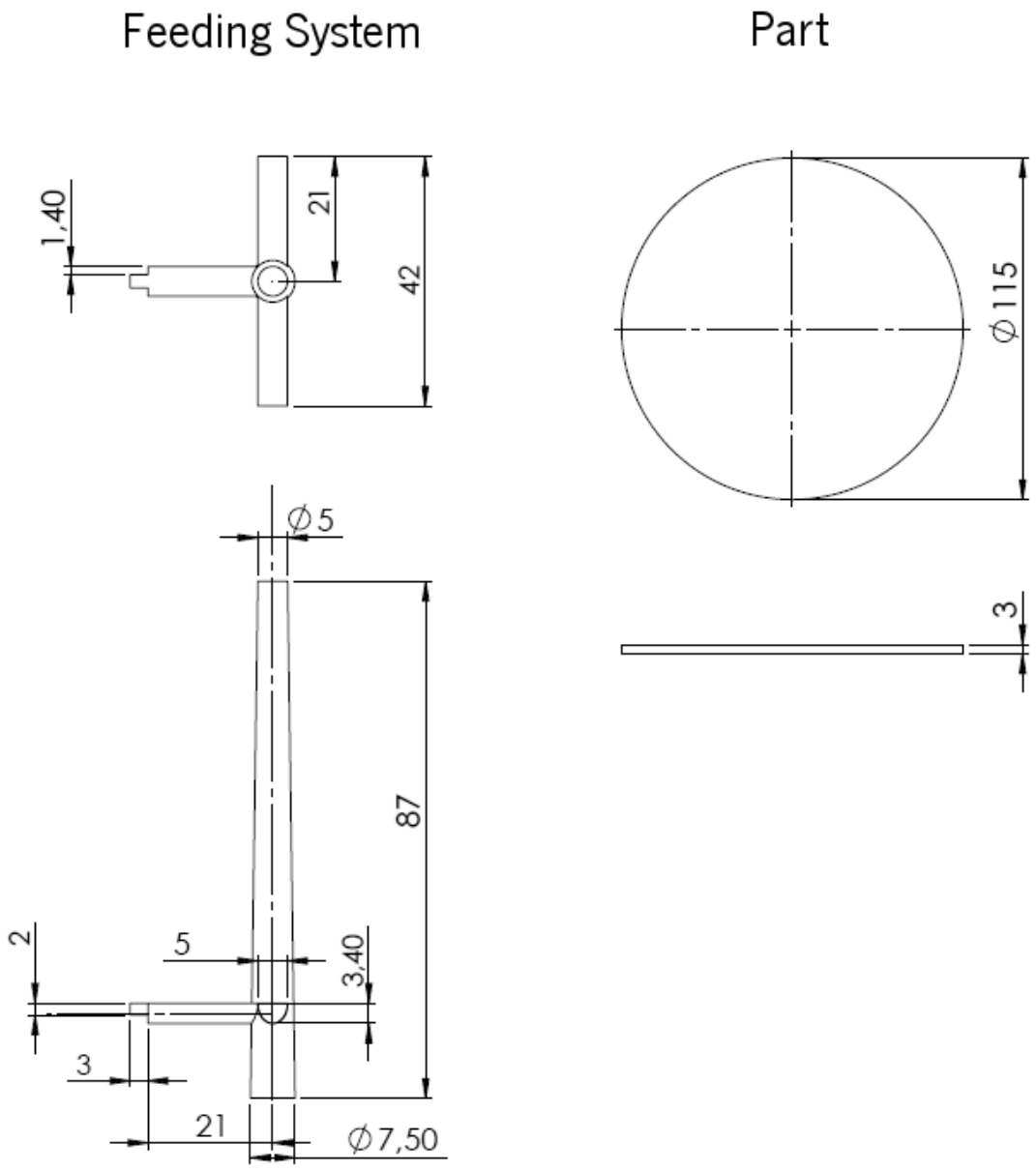

Figure ii: Technical drawing of the feeding system and part

ANNEX III – ANOVA RESULTS FOR THE THERMOMECHANICAL INDICES

Table i: ANOVA of the cooling index for the filling stage

Source	Sum of Squares	df	Mean Square	F Value	Prob > F	Contribution
Model	0.11	2	0.054	777.30	< 0.0001	
B-Injection Temperature	0.035	1	0.035	509.39	< 0.0001	32.66 %
C-Mould Temperature	0.072	1	0.072	1045.22	< 0.0001	67.02 %
Residual	3.464×10^{-4}	5	6.928×10^{-5}			0.32%
Total	0.11	7				
	R^2 adj	0.9955		R^2 pred	0.9918	

The cooling index for the end of the filling stage presents a model F-value of 777.30 implies the model is significant. There is only a 0.01% chance that a "Model F-Value" this large could occur due to noise. It also indicates an adequate precision of 63.392 and a R^2 of 0.9968.

Table ii: ANOVA of the cooling index for the packing stage

Source	Sum of Squares	df	Mean Square	F Value	Prob > F	Contribution
Model	0.020	4	5.053×10^{-3}	16.82	0.0215	
A-Injection Velocity	0.013	1	0.013	44.72	0.0068	63.62 %
C-Mould Temperature	1.969×10^{-3}	1	1.969×10^{-3}	6.56	0.0832	9.33 %
D-Hold Pressure	1.789×10^{-3}	1	1.789×10^{-3}	5.96	0.0925	8.47 %
AC	3.022×10^{-3}	1	3.022×10^{-3}	10.06	0.0504	14.31 %
Residual	9.011×10^{-4}	3	3.004×10^{-4}			4.27 %
Total	0.021	7				
	R^2 adj	0.900		R^2 pred	0.700	

The weighted cooling index for the end of the packing stage presents a model F-value of 16.82 implies the model is significant. There is only a 2.15% chance that a "Model F-Value" this large could occur due to noise. It also indicates an adequate precision of 11.001 and a R^2 of 0.9573.

Table iii: ANOVA of the cooling index for the cooling stage

Source	Sum of Squares	df	Mean Square	F Value	Prob > F	Contribution
Model	0.020	3	6.640×10^{-3}	14.36	0.0131	
A-Injection Velocity	0.014	1	0.014	29.87	0.0055	63.43 %
D-Hold Pressure	1.539×10^{-3}	1	1.539×10^{-3}	3.33	0.1421	7.07 %
AC	4.573×10^{-3}	1	4.573×10^{-3}	9.89	0.0347	21.01 %
Residual	1.849×10^{-3}	4	4.622×10^{-4}			8.49 %
Total	0.022	7				
	R^2 adj	0.8514		R^2 pred	0.6603	

The weighted cooling index for the end of the cooling stage presents a model F-value of 14.36. There is only a 1.31% chance that a "Model F-Value" this large could occur due to noise. It also indicates an adequate precision of 10.436 and a R^2 of 0.9151.

Table iv: ANOVA of the thermo-stress index for the end of the filling stage

Source	Sum of Squares	df	Mean Square	F Value	Prob > F	Contribution
Model	1.245×10^9	3	4.150×10^8	41.23	0.0018	
A-Injection Velocity	3.147×10^8	1	3.147×10^8	31.26	0.0050	24.40 %
B-Injection Temperature	7.962×10^8	1	7.962×10^8	79.10	0.0009	61.95 %
C-Mould Temperature	1.341×10^8	1	1.341×10^8	13.33	0.0218	10.44 %
Residual	4.026×10^7	4	1.007×10^7			3.21 %
Total	1.285×10^9	7				
	R^2 adj	0.9452		R^2 pred	0.8747	

The thermo-stress index for the end of the filling stage presents a model F-value of 41.23. There is only a 0.18% chance that a "Model F-Value" this large could occur due to noise. It also indicates an adequate precision of 18.136 and a R^2 of 0.9687.

Table v: ANOVA of the weighted thermo-stress index for the end of the packing stage

Source	Sum of Squares	df	Mean Square	F Value	Prob > F	Contribution
Model	1.389×10^8	2	6.945×10^7	18.32	0.0050	
B-Injection Temperature	5.681×10^7	1	5.681×10^7	14.99	0.0117	35.99 %
C-Mould Temperature	8.208×10^7	1	8.208×10^7	21.65	0.0056	52.00 %
Residual	1.895×10^7	5	3.791×10^6			12.01 %
Total	1.578×10^8	7				
	R^2 adj	0.8319		R^2 pred	0.6926	

The weighted thermo-stress index for the end of the packing stage presents a model F-value of 18.32. There is only a 0.50% chance that a "Model F-Value" this large could occur due to noise. It also indicates an adequate precision of 9.844 and a R^2 of 0.8799.

Table vi: ANOVA of the weighted thermo-stress index for the end of the cooling stage

Source	Sum of Squares	df	Mean Square	F Value	Prob > F	Contribution
Model	1.489×10^8	2	7.444×10^7	37.51	0.0010	
B-Injection Temperature	5.341×10^7	1	5.341×10^7	26.91	0.0035	33.63 %
C-Mould Temperature	9.547×10^7	1	9.547×10^7	48.10	0.0010	60.12 %
Residual	9.923×10^6	5	1.985×10^6			6.25 %
Total	1.588×10^8	7				
	R^2 adj	0.9125		R^2 pred	0.8400	

The weighted thermo-stress index for the end of the cooling stage presents a model F-value of 37.51. There is only a 0.10% chance that a "Model F-Value" this large could occur due to noise. It also indicates an adequate precision of 13.999 and a R^2 of 0.9375.

ANNEX IV – PLM IMAGES

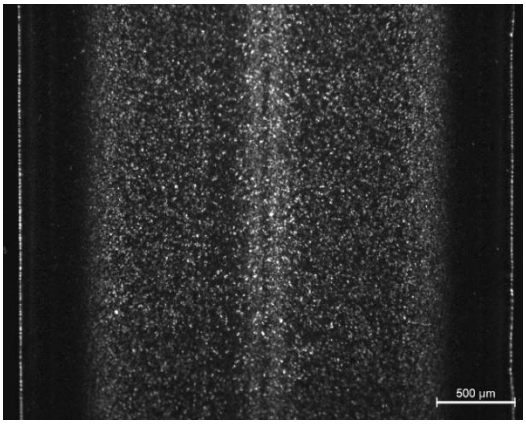

Figure iii: Microstructure of experiment E1

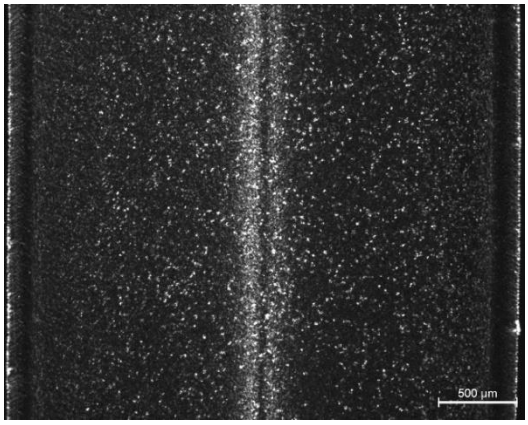

Figure iv: Microstructure of experiment E2

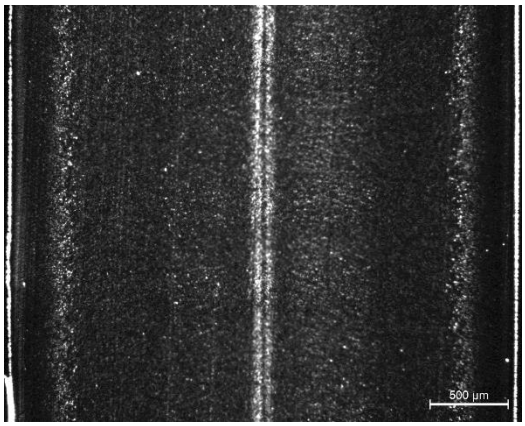

Figure v: Microstructure of experiment E3

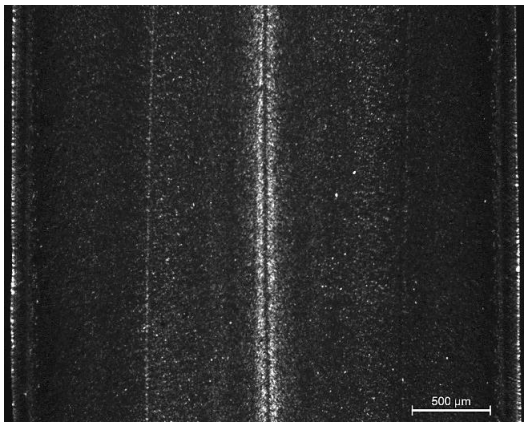

Figure vi: Microstructure of experiment E4

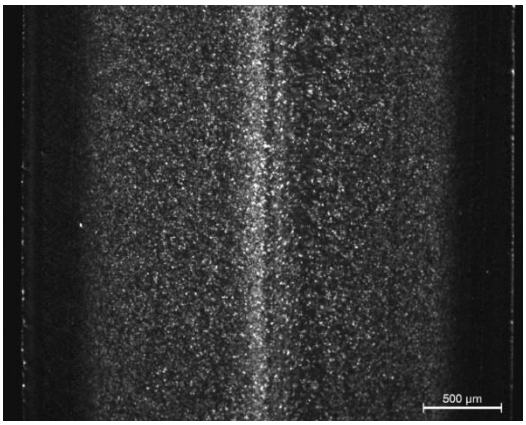

Figure vii: Microstructure of experiment E5

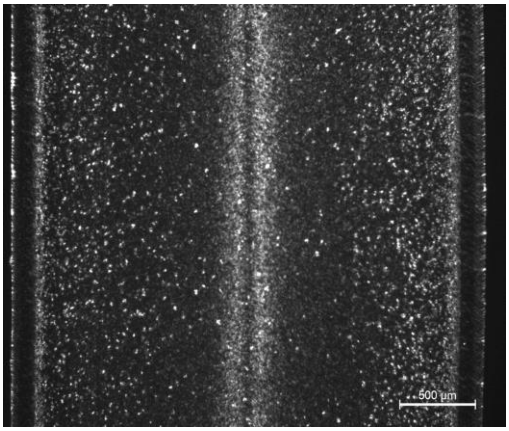

Figure viii: Microstructure of experiment E6

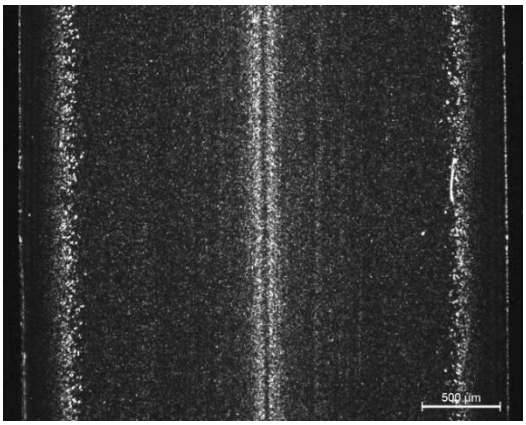

Figure ix: Microstructure of experiment E7

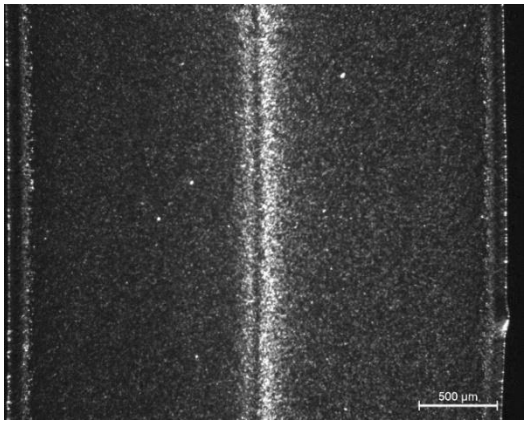

Figure x: Microstructure of experiment E8

Table vii: Sa measurement results

Experiment	Sa Average	Standard Deviation
E1	0.256	0.005
E2	0.110	0.002
E3	0.173	0.001
E4	0.074	0.001
E5	0.229	0.003
E6	0.107	0.002
E7	0.154	0.001
E8	0.068	0.001

ANNEX V – DSC CURVES

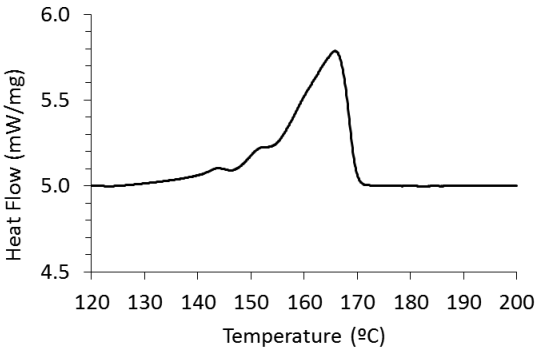

Figure xi: DSC thermogram of experiment E1

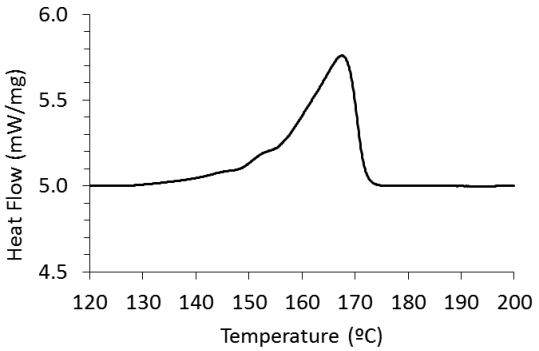

Figure xii: DSC thermogram of experiment E2

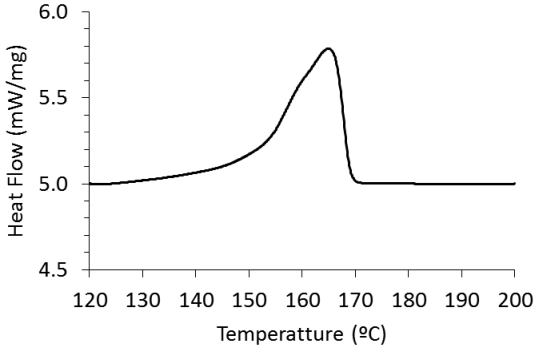

Figure xiii: DSC thermogram of experiment E3

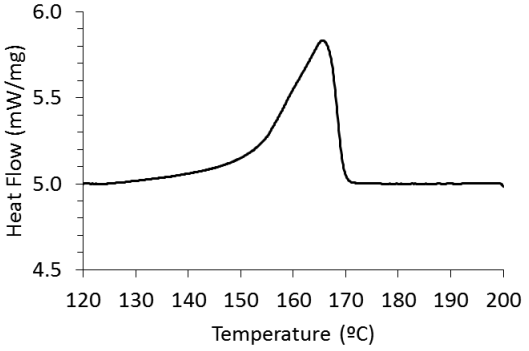

Figure xiv: DSC thermogram of experiment E4

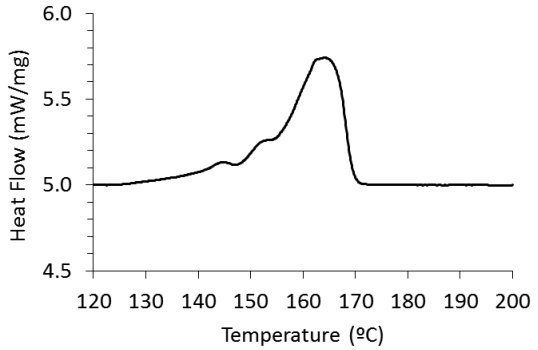

Figure xv: DSC thermogram of experiment E5

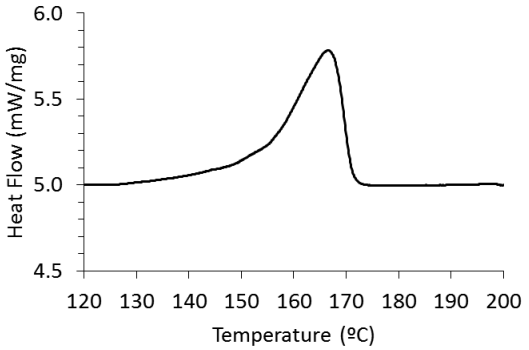

Figure xvi: DSC thermogram of experiment E6

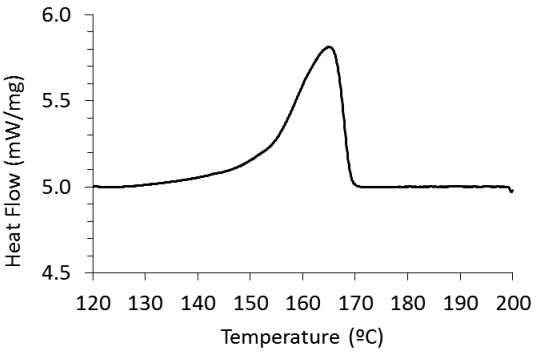

Figure xvii: DSC thermogram of experiment E7

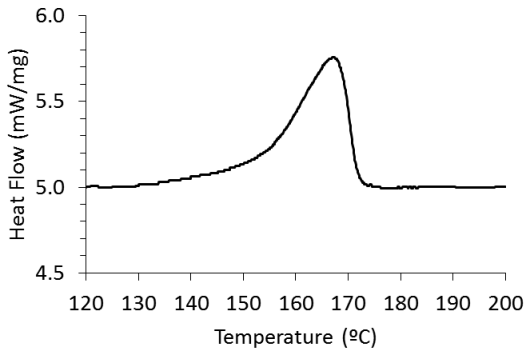

Figure xviii: DSC thermogram of experiment E8

Table viii: Bulk crystallinity results

	χ_{Bulk}	Standard Deviation
E1	40.88%	0.33%
E2	40.35%	0.85%
E3	41.51%	0.35%
E4	41.51%	0.18%
E5	41.31%	0.15%
E6	41.47%	0.87%
E7	41.26%	0.36%
E8	41.61%	0.33%

ANNEX VI – X-RAY DIFFRACTION

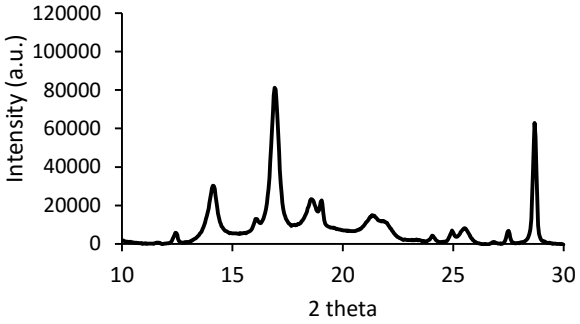

Figure xix: XRD spectrum of experiment E1

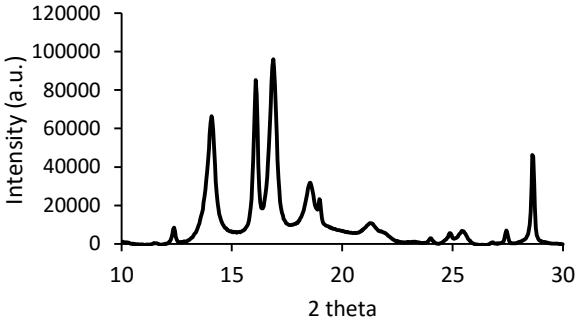

Figure xx: XRD spectrum of experiment E2

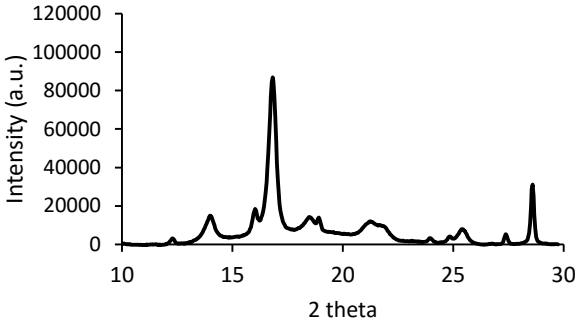

Figure xxi: XRD spectrum of experiment E3

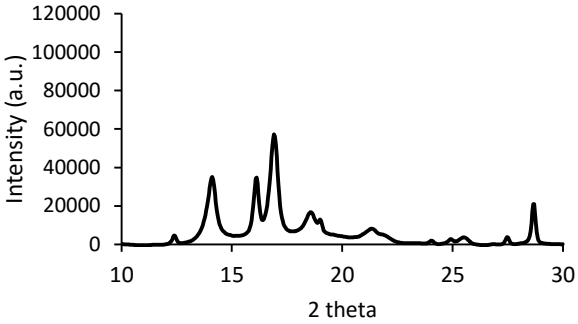

Figure xxii: XRD spectrum of experiment E4

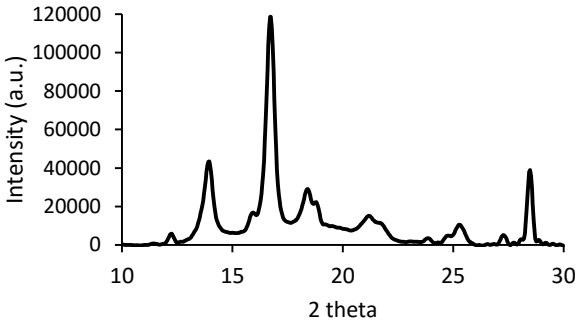

Figure xxiii: XRD spectrum of experiment E5

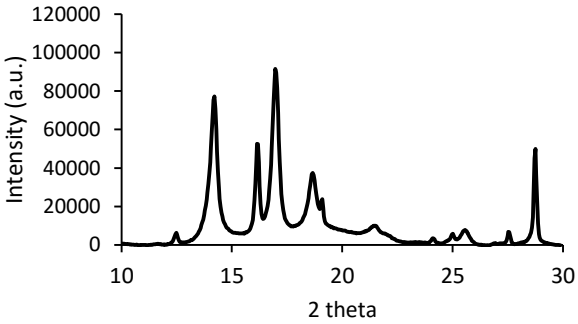

Figure xxiv: XRD spectrum of experiment E6

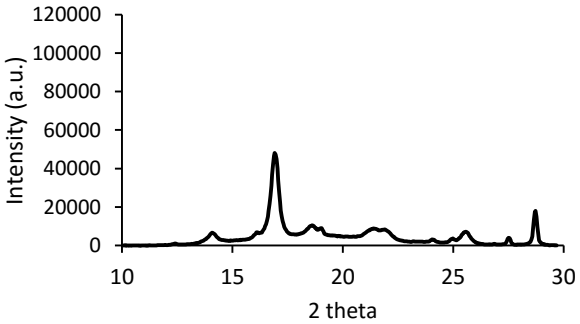

Figure xxv: XRD spectrum of experiment E7

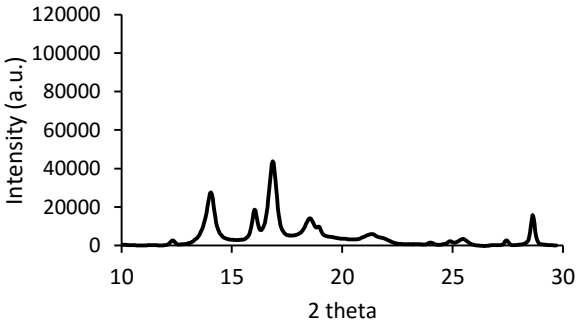

Figure xxvi: XRD spectrum of experiment E8

Table ix: XRD deconvolution results

	(1 1 0) α		(3 0 0) β		(040) α		≈ 17.5° (halo)	
	Area	Amplitude	Area	Amplitude	Area	Amplitude	Area	Amplitude
E1	15701	29617	1580	4795	34848	75024	66555	9034
E2	34027	57226	18978	60006	38859	79997	57336	10000
E3	8064	11821	3792	11638	39577	78985	40419	7655
E4	19080	34711	9280	25080	25927	50861	41854	6897
E5	23087	37522	2406	6102	61495	106440	67422	11207
E6	42015	67105	12685	40690	40032	78498	61363	9552
E7	3183	4643	246	1343	24280	42732	37642	5517
E8	14406	24980	5846	13750	17059	38795	32493	4966
	(1 3 0) α		(1 1 1) α		(1 3 1/ 0 4 1) α		(1 5 0/0 6 0) α	
E1	8765	15989	6747	9811	7402	8035	4779	8000
E2	10093	20945	6291	7420	1265	2600	3698	6342
E3	2480	5517	6982	8001	6589	6759	3804	6586
E4	6880	10695	4641	5914	1950	2617	1993	3501
E5	9886	17034	7933	10703	4761	7131	5948	10185
E6	13632	26624	3824	5652	786	1591	3528	7095
E7	2437	4443	3750	4911	3766	4856	3632	6891
E8	4837	9189	2999	3901	958	1450	1541	3164
	(2 0 0) α							
E1	15359	49778						
E2	10439	36988						
E3	7042	23626						
E4	6284	18963						
E5	13287	39610						
E6	14490	35896						
E7	4922	15837						
E8	4492	14239						

ANNEX VII – TENSILE TESTS

Quasi-Static Curves

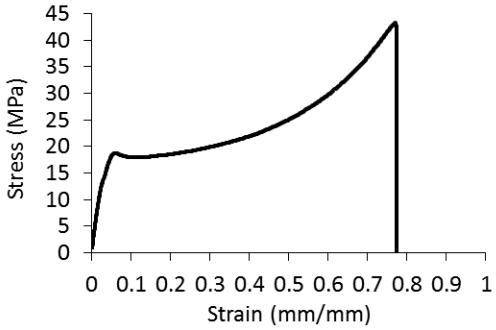

Figure xxvii: Quasi-static tensile curve of experiment E1

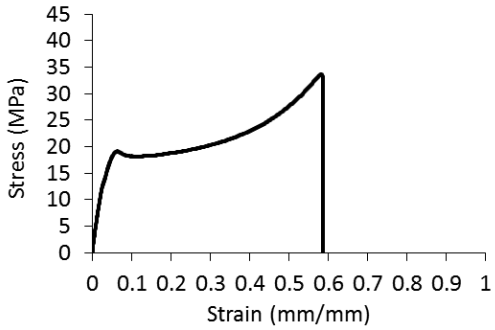

Figure xxviii: Quasi-static tensile curve of experiment E2

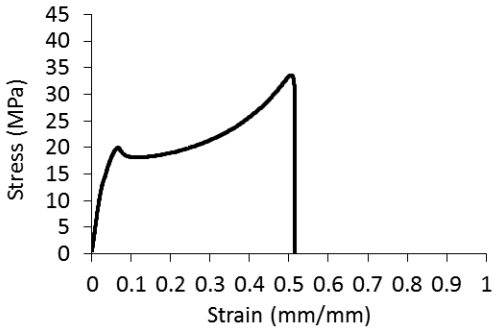

Figure xxix: Quasi-static tensile curve of experiment E3

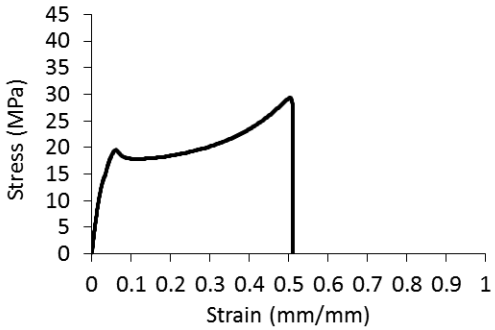

Figure xxx: E Quasi-static tensile curve of experiment E4

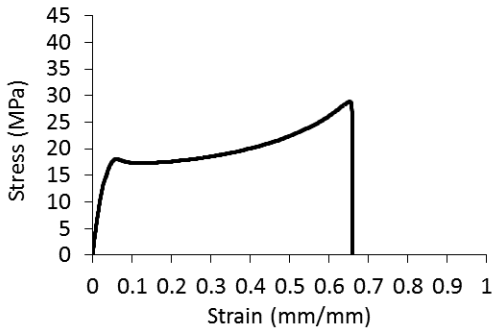

Figure xxxi: Quasi-static tensile curve of experiment E5

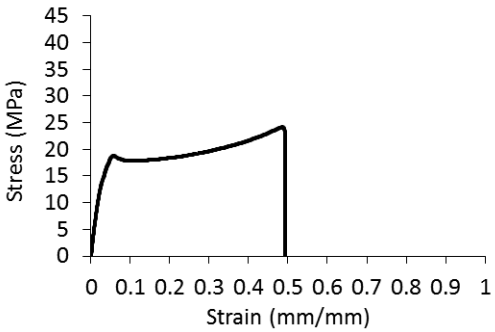

Figure xxxii: Quasi-static tensile curve of experiment E6

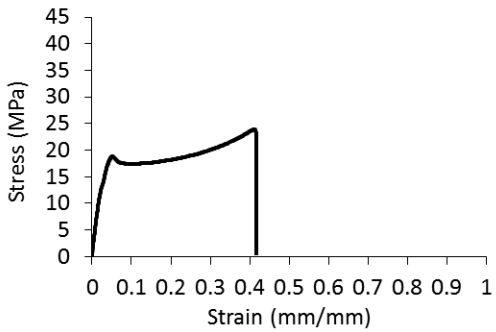

Figure xxxiii: Quasi-static tensile curve of experiment E7

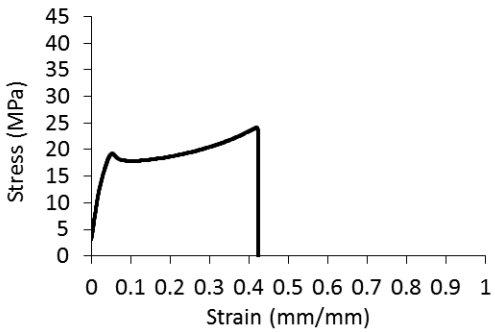

Figure xxxiv: Quasi-static tensile curve of experiment E8

High Speed tensile Curves: 1 m/s

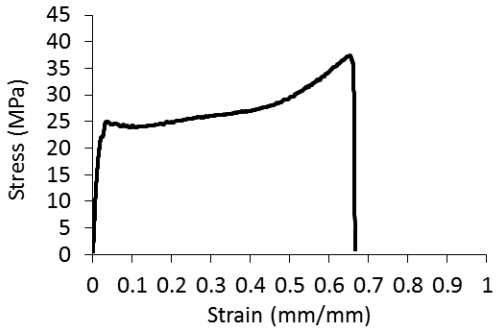

Figure xxxv: Tensile curve of experiment E1 at 1m/s

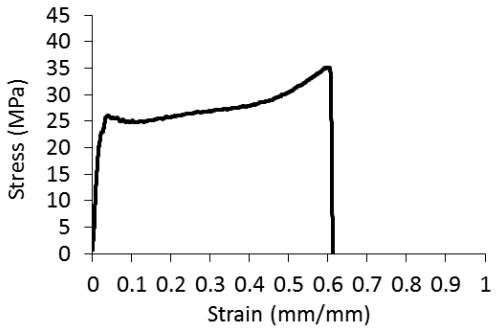

Figure xxxvi: Tensile curve of experiment E2 at 1m/s

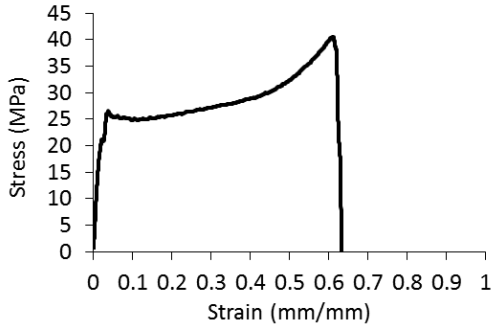

Figure xxxvii: Tensile curve of experiment E3 at 1m/s

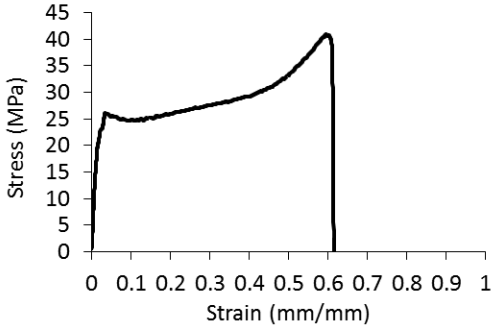

Figure xxxviii: Tensile curve of experiment E4 at 1m/s

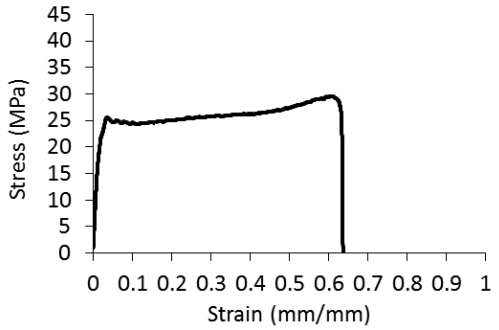

Figure xxxix: Tensile curve of experiment E5 at 1m/s

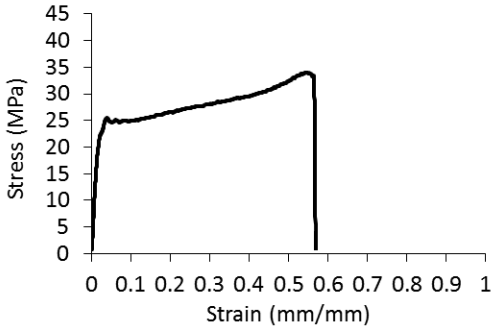

Figure xl: Tensile curve of experiment E6 at 1m/s

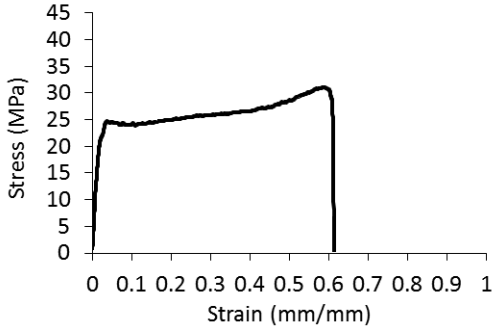

Figure xli: Tensile curve of experiment E7 at 1m/s

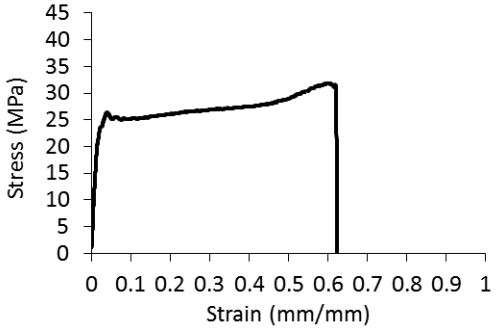

Figure xlii: Tensile curve of experiment E8 at 1m/s

High Speed tensile Curves: 3 m/s

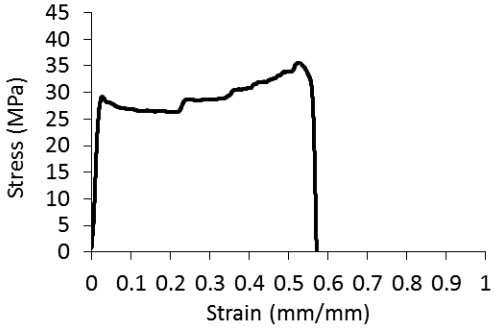

Figure xliii: Tensile curve of experiment E1 at 3m/s

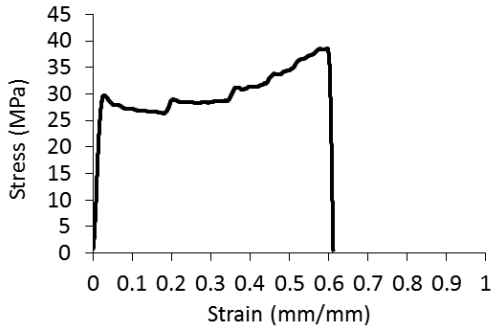

Figure xliv: Tensile curve of experiment E2 at 3m/s s

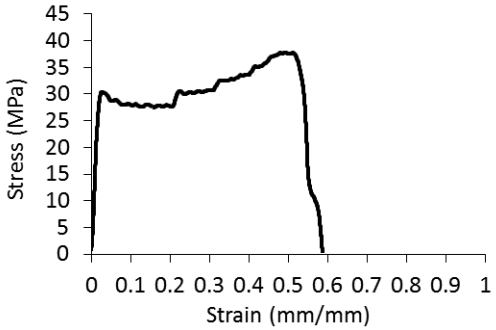

Figure xlv: Tensile curve of experiment E3 at 3m/s

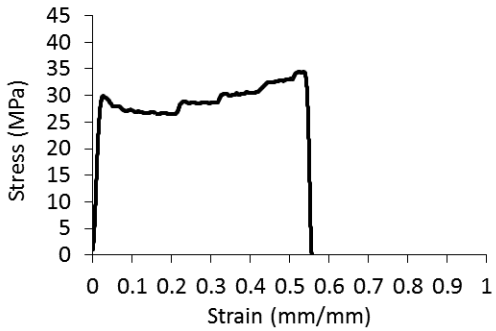

Figure xlvi: Tensile curve of experiment E4 at 3m/s

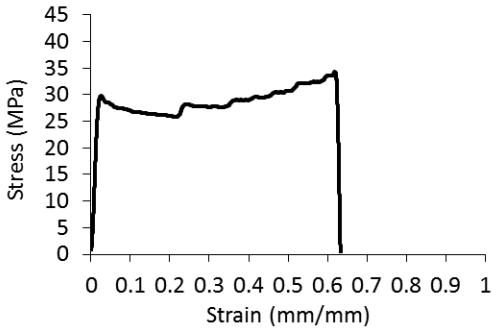

Figure xlvii: Tensile curve of experiment E5 at 3m/s

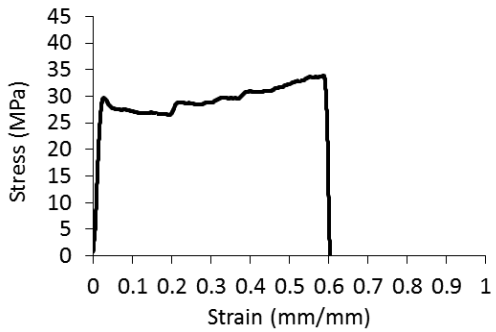

Figure xlviii: Tensile curve of experiment E6 at 3m/s

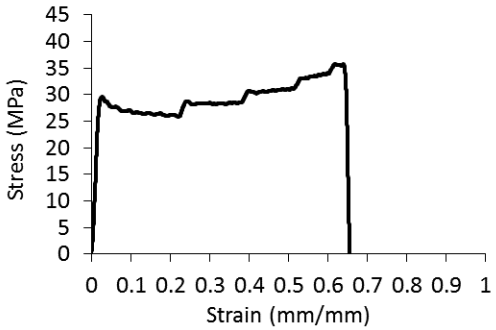

Figure xlix: Tensile curve of experiment E7 at 3m/s

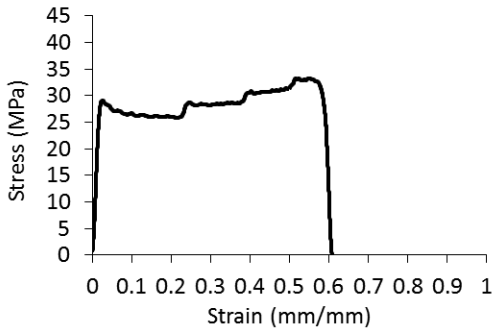

Figure l: Tensile curve of experiment E8 at 3m/s

Area variation equations

Table x: Area variation equation and regression coefficient

Quasi-static (20 mm/min)		
	Equation	R^2
E1	$5 \times 10^{-4}x^2 - 0.233x + 28.934$	0.997
E2	$2 \times 10^{-4}x^2 - 0.2576x + 30.098$	0.995
E3	$3 \times 10^{-4}x^2 - 0.3101x + 29.499$	0.995
E4	$-4 \times 10^{-4}x^2 - 0.2336x + 29.558$	0.995
E5	$-2 \times 10^{-5}x^2 - 0.1698x + 28.661$	0.996
E6	$2 \times 10^{-4}x^2 - 0.2045x + 28.301$	0.992
E7	$1 \times 10^{-3}x^2 - 0.193x + 28.54$	0.994
E8	$1 \times 10^{-4}x^2 - 0.2486x + 29.324$	0.995
1 m/s		
E1	$-0.0108x^2 - 0.4376x + 28.013$	0.994
E2	$-0.013x^2 - 0.4414x + 29.403$	0.990
E3	$-0.0152x^2 - 0.4911x + 28.561$	0.991
E4	$-0.0159x^2 - 0.5404x + 29.361$	0.997
E5	$-0.006x^2 - 0.3825x + 28.43$	0.990
E6	$-0.003x^2 - 0.6308x + 27.833$	0.991
E7	$-0.0061x^2 - 0.475x + 28.605$	0.994
E8	$-0.0073x^2 - 0.4416x + 28.907$	0.988
3 m/s		
E1	$-0.1248x^2 - 1.5991x + 28.606$	0.992
E2	$-0.1649x^2 - 1.3453x + 29.139$	0.993
E3	$-0.0955x^2 - 2.1383x + 28.792$	0.993
E4	$-0.0996x^2 - 1.6912x + 29.094$	0.991
E5	$-0.097x^2 - 1.0629x + 28.112$	0.991
E6	$-0.0417x^2 - 1.5061 + 28.082$	0.991
E7	$-0.0542x^2 - 1.447 + 27.996$	0.992
E8	$-0.0468x^2 - 1.7011x + 28.329$	0.992

Quasi-Static tensile: ANOVA tables

Table xi: ANOVA of the Yield Stress obtained at quasi-static conditions

	Sum Of Squares	d.f	Mean Square	F-Value	Prob> F	Contribution
Model	1.50	2	0.75	11.04	0.0146	
B-Injection Temperature	1.02	1	1.02	14.97	0.0118	55.27%
C- Mould Temperature	0.48	1	0.48	7.12	0.0445	26.28%
Residual	0.34	5	0.068			18.45%
Total	1.84	7				100%
	R^2 adj	0.7416		R^2 pred	0.5475	

The quasi-static yield stress presents a Model F-Value of 11.04 with a 1.46% change that this value occurred due to noise (R^2=0.8154). It also indicates an adequate precision of 7.548

Table xii: ANOVA of the Modulus obtained at quasi-static conditions

	Sum Of Squares	d.f	Mean Square	F-Value	Prob> F	Contribution
Model	2677.75	1	2677.75	10.24	0.0186	
D- Holding Pressure	2677.75	1	2677.75	10.24	0.0186	63.05%
Residual	1569.10	6	261.52			36.95 %
Total	4246.85	7				100%
	R^2 adj	0.5689		R^2 pred	0.3432	

The quasi-static modulus presents a Model F-Value of 10.24 with a 1.86% change that this value occurred due to noise (R^2= 0.6305). It also indicates an adequate precision of 4.525.

Table xiii: ANOVA of the Strain at break obtained at quasi-static conditions

	Sum Of Squares	d.f	Mean Square	F-Value	Prob> F	Contribution
Model	0.11	4	0.029	424.07	0.0002	
A-Injection Velocity	0.019	1	0.019	274.88	0.0005	16.18 %
B- Injection Temperature	0.058	1	0.058	854.51	< 0.0001	50.29%
C- Mould Temperature	0.018	1	0.018	271.78	0.0005	15.99 %
AB	0.020	1	0.020	295.12	0.0004	17.37 %
Residual	2.022×10^{-4}	3	6.741×10^{-5}			0.17%
Total	0.11	7				
	R^2 adj	0.9959		R^2 pred	0.9874	

The quasi-static strain at break present a model F-Value of 424.07 with a 0.02% change that this value occurred due to noise (R^2=0.9982). It also indicates an adequate precision of 56.257.

High Speed tensile: ANOVA tables

Table xiv: ANOVA of the Yield Stress at 1 m/s

	Sum Of Squares	d.f	Mean Square	F-Value	Prob> F	Contribution
Model	1.38	2	0.69	5.06	0.0629	
C- Mould Temperature	0.78	1	0.78	5.77	0.0615	38.13%
D- Holding Pressure	0.59	1	0.59	4.36	0.0912	28.80%
Residual	0.68	5	0.14			33.07%
Total	2.06	7				100%
	R^2 adj	0.5371		R^2 pred	0.1536	

The yield stress evaluated at 1 m/s presents a model F-Value of 5.06 with a 6.29% change that the value occurred due to noise (R^2= 0.6694). It also indicates an adequate precision of 5.183

Table xv: ANOVA of the Yield Stress at 3 m/s

	Sum Of Squares	d.f	Mean Square	F-Value	Prob> F	Contribution
Model	1.36	4	0.34	13.43	0.0295	
B- Injection Temperature	0.17	1	0.17	6.92	0.0783	12.20%
C- Mould Temperature	0.74	1	0.74	29.48	0.0123	51.99%
D- Holding Pressure	0.22	1	0.22	8.61	0.0608	15.18%
AD	0.22	1	0.22	8.70	0.0600	15.35%
Residual	0.076	3	0.025			5.28%.
Total	1.43	7				
	R^2 adj	0.8766		R^2 pred	0.6238	

The yield stress evaluated at 3 m/s presents a model F-Value of 13.43 with a 2.95% change that the value occurred due to noise (R^2= 0.9471). It also indicates an adequate precision of 10.119.

Table xvi: ANOVA of the Young Modulus at 1m/s

	Sum Of Squares	d.f	Mean Square	F-Value	Prob> F	Contribution
Model	38235.15	6	6372.52	77730.42	0.0027	
A-Injection Velocity	11442.97	1	11442.97	1.396×10^5	0.0017	29.93 %
C- Mould Temperature	3078.54	1	3078.54	37551.22	0.0033	8.05 %
D- Holding Pressure	6233.53	1	6233.53	76034.94	0.0023	16.30 %
AB	3353.65	1	3353.65	40907.00	0.0031	8.77 %
AC	8799.39	1	8799.39	1.073×10^5	0.0019	23.01 %
AD	5327.07	1	5327.07	64978.20	0.0025	13.93 %
Residual	0.082	1	0.082			0.01 %
Total	38235.23					100%
	R^2 adj	1		R^2 pred	0.999	

The modulus evaluated at 1 m/s presents a model F-Value of 77730.42 with a 0.27% change that the value occurred due to noise (R^2= 1). It also indicates an adequate precision of 891.405.

Table xvii: ANOVA of the Young Modulus at 3m/s

	Sum Of Squares	d.f	Mean Square	F-Value	Prob> F	Contribution
Model	29332.16	1	29332.16	7.00	0.0383	
B-Injection Temperature	29332.16	1	29332.16	7.00	0.0383	53.83%
Residual	25156.13	6	4192.69			46.17%
Total	54488.29	7				
	R^2 adj	0.4614		R^2 pred	0.1792	

The modulus evaluated at 3 m/s presents a model F-Value of 7.00 with a 3.83% change that the value occurred due to noise (R^2= 0.5383).

Table xviii: ANOVA of the Strain at break at 1m/s

	Sum Of Squares	d.f	Mean Square	F-Value	Prob> F	Contribution
Model	4.851×10^{-3}	3	1.617×10^{-3}	7.45	0.0410	
A-Injection Velocity	2.665×10^{-3}	1	2.665×10^{-3}	12.27	0.0248	46.59%
C- Mould Temperature	1.009×10^{-3}	1	1.009×10^{-3}	4.65	0.0974	17.64%
AB	1.178×10^{-3}	1	1.178×10^{-3}	5.42	0.0803	20.59%
Residual	8.684×10^{-4}	4	2.171×10^{-4}			15.18%
Total	5.719×10^{-3}	7				
	R^2 adj	0.7343		R^2 pred	0.3927	

The strain at break evaluated at 1 m/s presents a model F-Value of 7.45 with a 4.10% change that the value occurred due to noise (R^2= 0.8482). It also indicates an adequate precision of 7.988.

Table xix: ANOVA of the Strain at break at 3m/s

	Sum Of Squares	d.f	Mean Square	F-Value	Prob> F	Contribution
Model	3.883×10^{-3}	2	1.941×10^{3}	6.01	0.0468	
C- Mould Temperature	1.784×10^{-3}	1	1.784×10^{-3}	5.52	0.0656	32.45%
AC	2.099×10^{-3}	1	2.099×10^{-3}	6.50	0.0514	38.17%
Residual	1.615×10^{-3}	5	3.231×10^{-4}			29.38%
Total	5.498×10^{-3}	7				
	R^2 adj	0.5887		R^2 pred	0.2478	

The strain at break evaluated at 3 m/s presents a model F-Value of 6.41 with a 4.68% change that the value occurred due to noise (R^2= 0.7062). It also indicates an adequate precision of 5.656.

ANNEX VIII – WEIGHTED TMI MODELS

Quasi-static

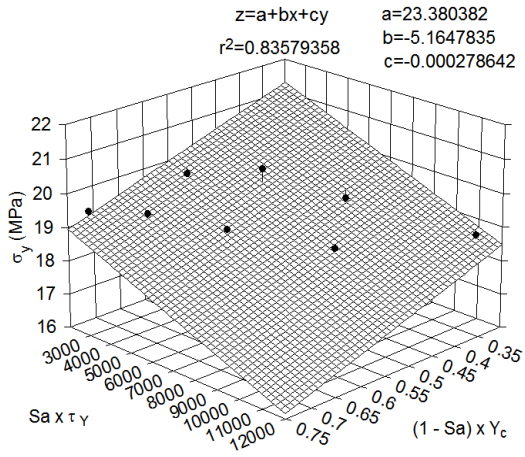

Figure Ii: Effect of the weighted TMI on the quasi-static σ_y

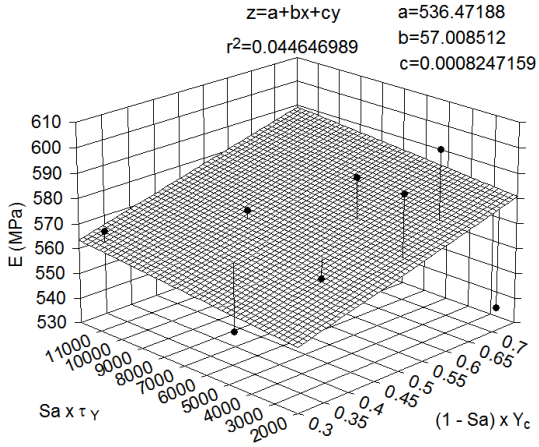

Figure Iii: Effect of the weighted TMI on the quasi-static E

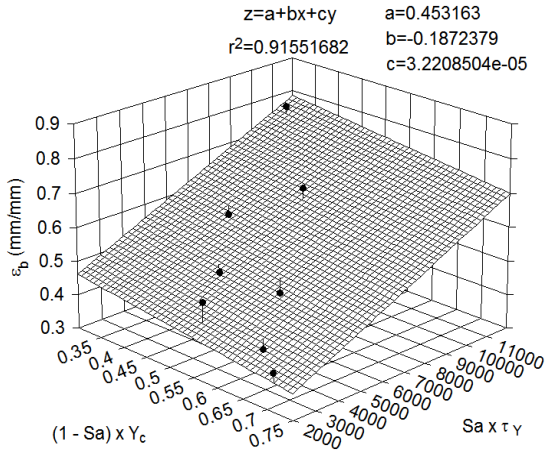

Figure Iiii: Effect of the weighted TMI on the quasi-static ε_b

Tensile tests at 1m/s

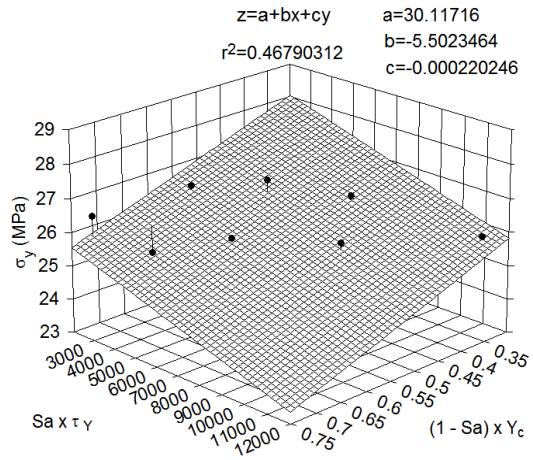

Figure Iiv: Effect of the weighted TMI on σ_y measured at 1m/s

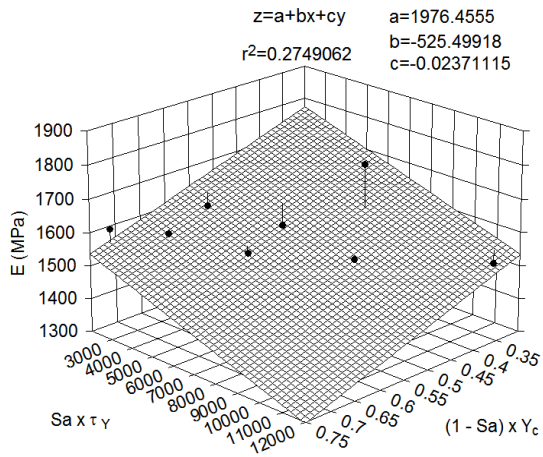

Figure Iv: Effect of the weighted TMI on E measured at 1m/s

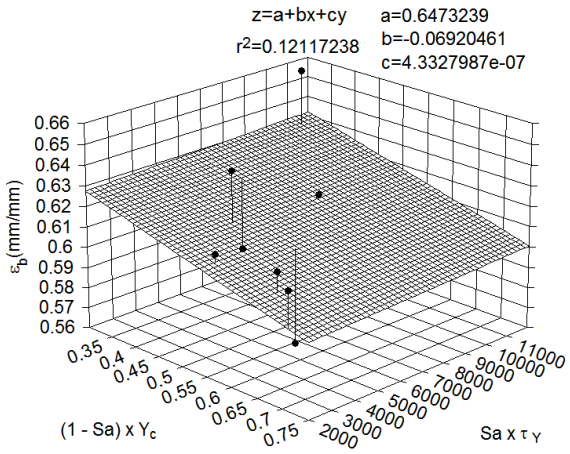

Figure lvi: Effect of the weighted TMI on ε_b measured at 1m/s

Tensile tests at 3m/s

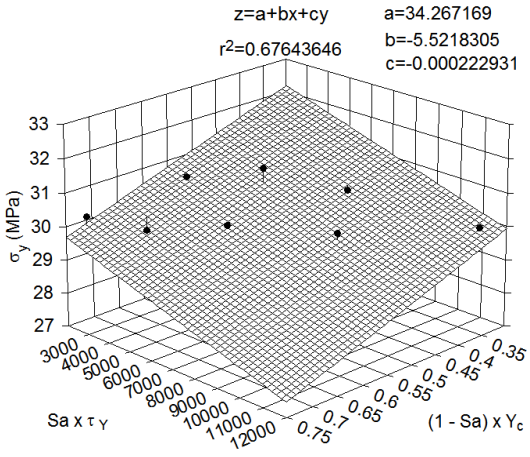

Figure lvii: Effect of the weighted TMI on σ_y measured at 3m/s

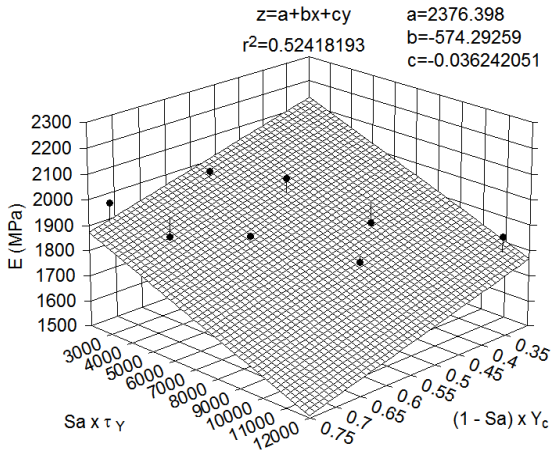

Figure lviii: Effect of the weighted TMI on E measured at 3m/s

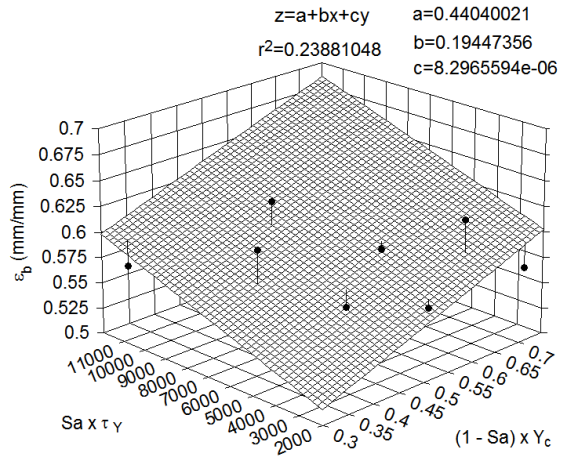

Figure lix: Effect of the weighted TMI on ε_b measured at 3m/s

ANNEX IX – CASE STUDY

PLM Images

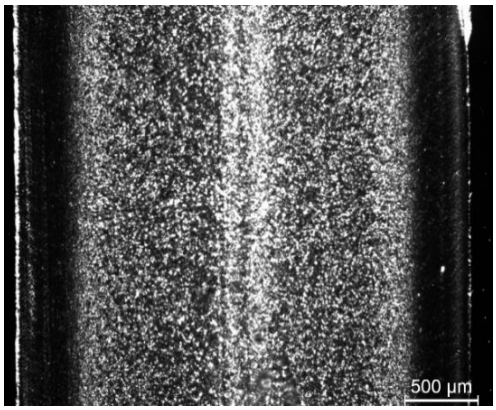

Figure lx: Microstructure of experiment C1

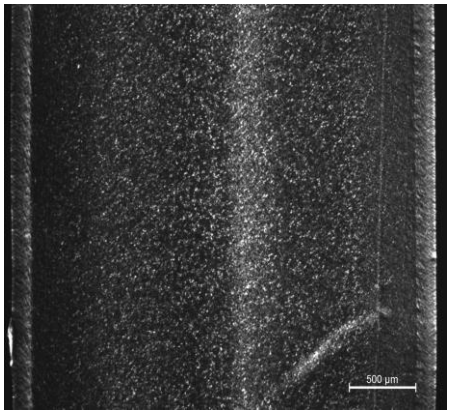

Figure lxi: Microstructure of experiment C2

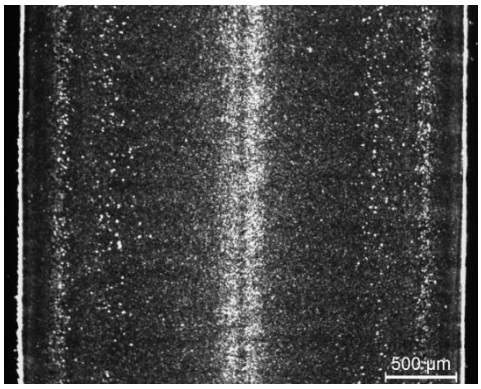

Figure lxii: Microstructure of experiment C3

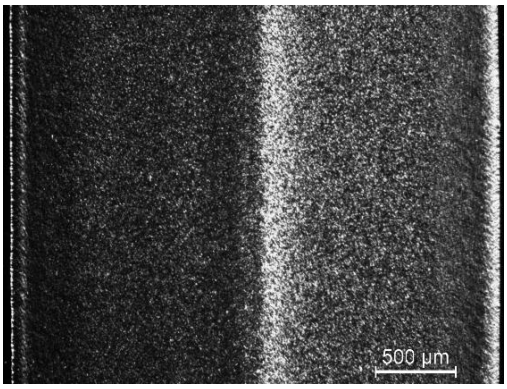

Figure lxiii: Microstructure of experiment C4

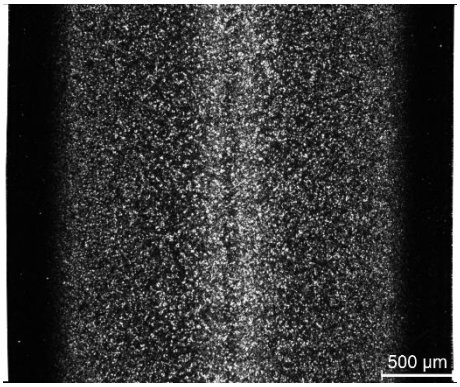

Figure lxiv: Microstructure of experiment C5

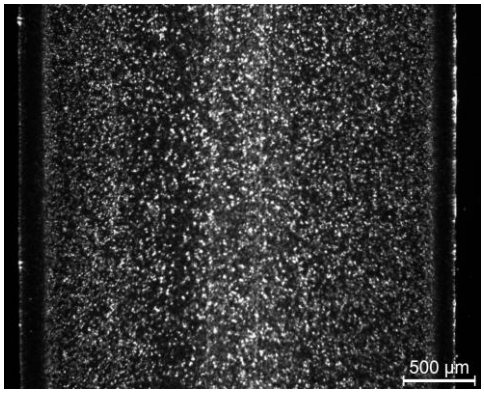

Figure lxv: Microstructure of experiment C6

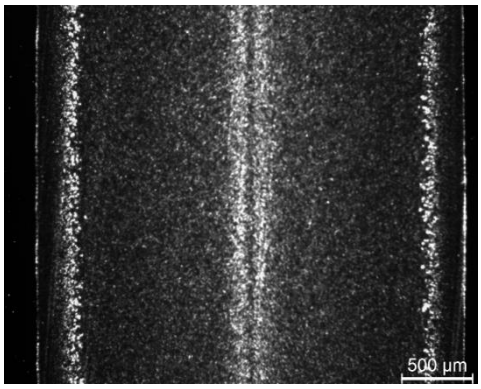

Figure lxvi: Microstructure of experiment C7

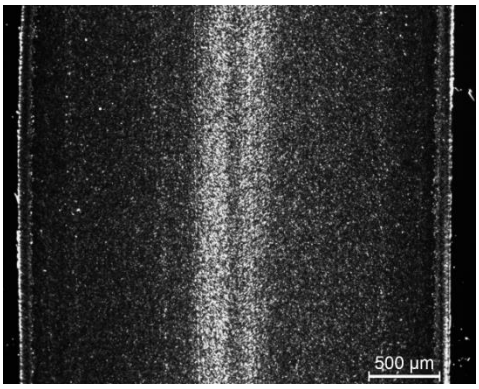

Figure lxvii: Microstructure of experiment C8

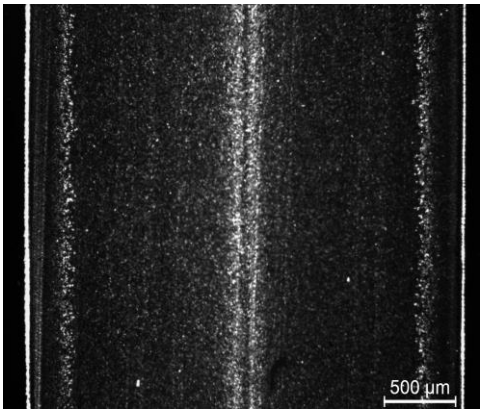

Figure lxviii: Microstructure of experiment C9

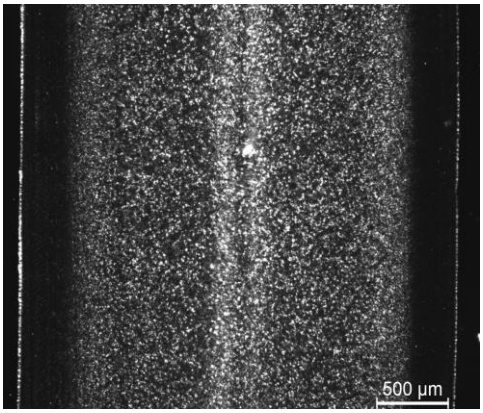

Figure lxix: Microstructure of experiment C10

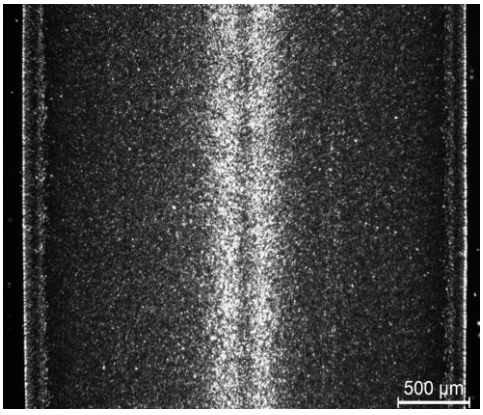

Figure lxx: Microstructure of experiment C11

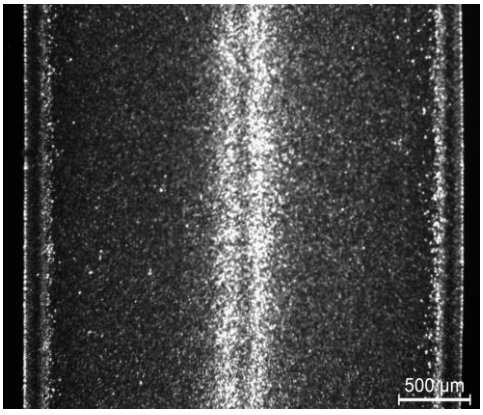

Figure lxxi: Microstructure of experiment C12

Falling weight impact test: Curves

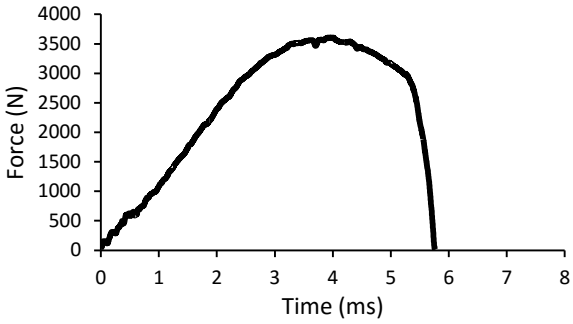

Figure lxxii: Falling weight curve of experiment C1

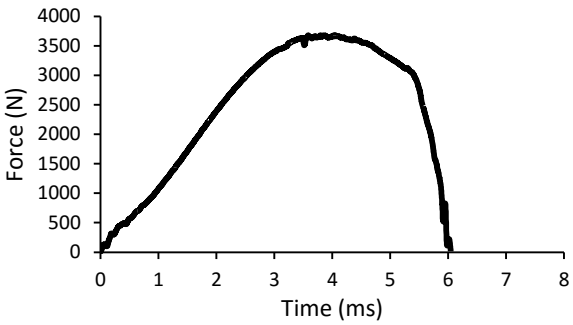

Figure lxxiii: Falling weight curve of experiment C2

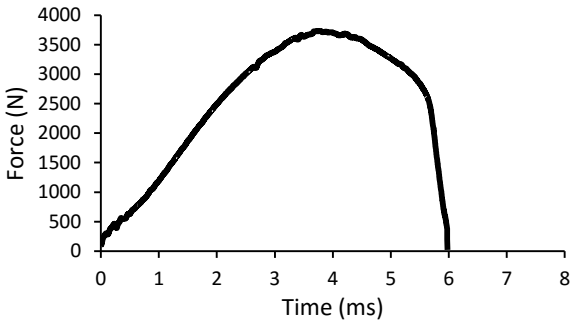

Figure lxxiv: Falling weight curve of experiment C3

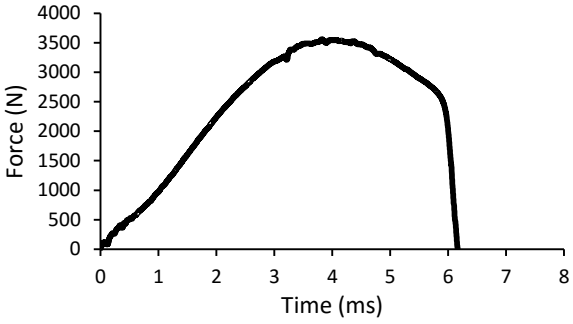

Figure lxxv: Falling weight curve of experiment C4

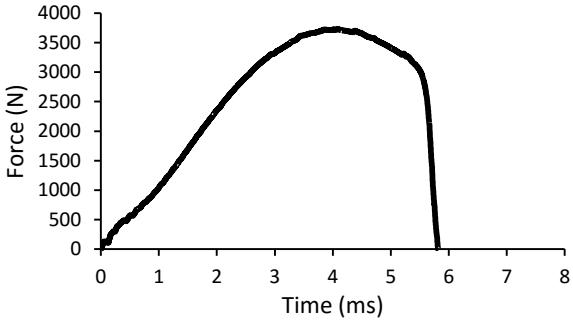

Figure lxxvi: Falling weight curve of experiment C5

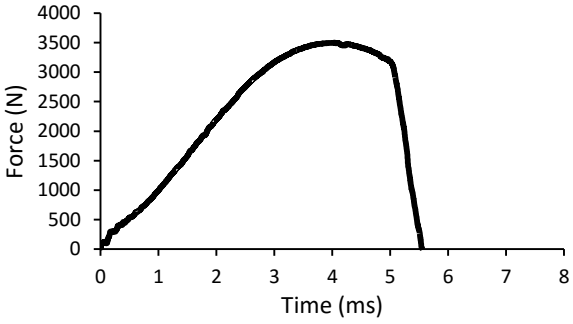

Figure lxxvii: Falling weight curve of experiment C6

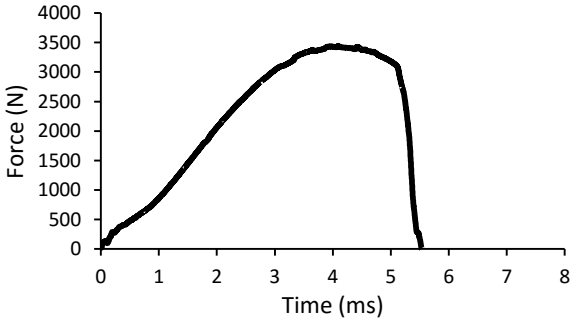

Figure lxxviii: Falling weight curve of experiment C7

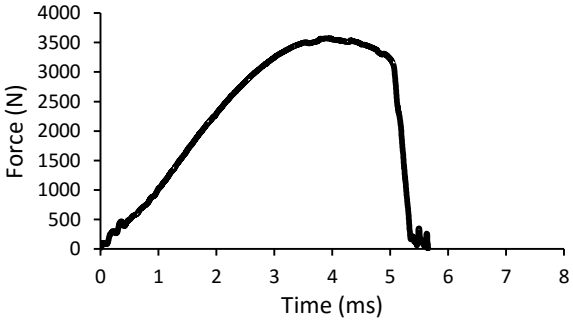

Figure lxxix: Falling weight curve of experiment C8

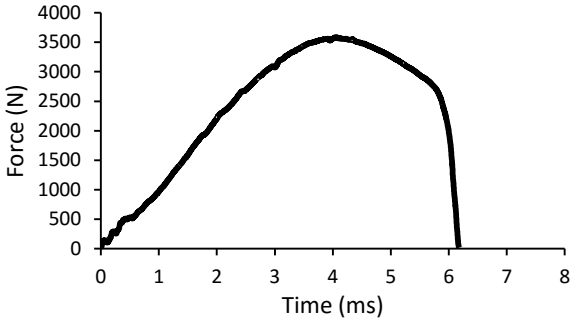

Figure lxxx: Falling weight curve of experiment C9

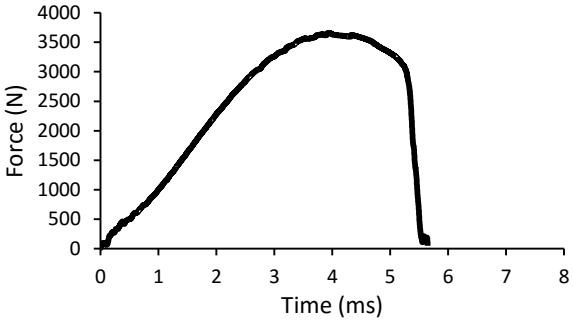

Figure lxxxi: Falling weight curve of experiment C10

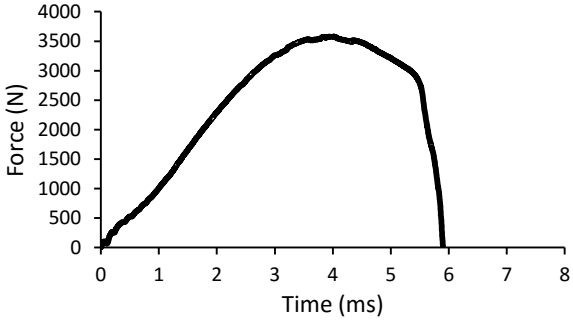

Figure lxxxii: Falling weight curve of experiment C11

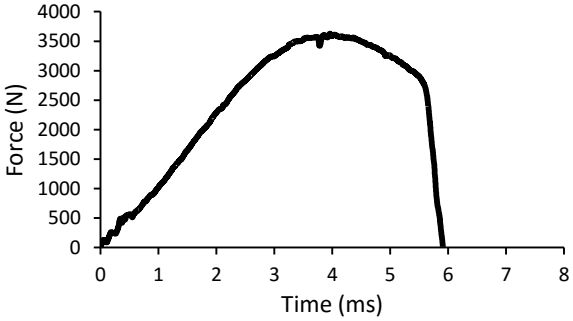

Figure lxxxiii: Falling weight curve of experiment C12